Title
Improving the accuracy and resolution of electrochemical aptamer-based sensors

Author
Downs, Alexandra

Publication Date
2021

UNIVERSITY OF CALIFORNIA

Santa Barbara

Improving the accuracy and resolution of electrochemical aptamer-based sensors

A dissertation submitted in partial satisfaction of the requirements the degree,

Doctor of Philosophy in Mechanical Engineering

by

Alex M. Downs

Committee:

Professor Kevin Plaxco, Chair

Professor Lior Sepunaru

Professor Carl Meinhart

Professor Bassam Bamieh

September 2021

The dissertation of Alex M. Downs is approved.

Lior Sepunaru

Carl Meinhart

Bassam Bamieh

Kevin Plaxco, Committee Chair

August 2021

Improving the accuracy and resolution of electrochemical aptamer-based sensors

by

Alex M. Downs

Acknowledgements

I would first like to thank my family for supporting my interests, both scientific and beyond. Thank you for encouraging my love for reading and learning, and for tolerating my enduring skill at mess-making. I thank my Mom for visiting me in Santa Barbara, and my Aunt Mary for making that crazy turn-around drive out to see me.

I thank my family at University of Arizona, who treated me with nothing but kindness, and provided my first opportunities to explore research. Anyone in lab can confirm - much of my five years at UC Santa Barbara were spent talking about my love for Tucson and the U of A. In particular, I would like to thank Dr. Pamela Vandiver for her vivid, memorable teaching in experimental research, and for showing me that art and exploring can very much be part of being a scientist.

I thank everyone from the Pennathur lab, which was my first home at UC Santa Barbara. I am grateful to everyone for their friendship, support, and good memories together. I would like to thank Karen Scida for giving me my very first introduction to electrochemistry, which has served me well throughout my PhD. I thank Seth Boden for his friendship throughout my time in Santa Barbara, and for always making me laugh.

I thank all of the friends I’ve made at UC Santa Barbara, in the Mechanical Engineering department and beyond. I remember so happily our lunches together at Nano Cafe, exploring Santa Barbara together, and navigating the different milestones of grad school. I’m especially grateful to Simone Stewart, Melanie Adams, and Kerry Lane for being bright spots in life outside of research.

I thank the Plaxco group wholeheartedly for making me a part of the tribe, and for endless good conversations over the years. I thank Phil Dauphin-Ducharme for his spectacular mentorship – I owe much of what I know about electrochemistry and experimental techniques to him. I thank Julian Gerson and Kyle Ploense for all their support on the in vivo side of experiments. Those experiments are so, so difficult, and

I am always stunned by what a spectacular job you do. I thank Martin, Alejandro, Lisa, Andrea, Nate, Kaylyn, Julia, and Gabi for your friendship and support throughout my PhD. I’ve loved our chats together about life plans, travel, and family. I looked forward every day to seeing you folks in lab. Thank you for being people I can count on for anything.

I thank, who else, but Kevin Plaxco, for being the best advisor I could have hoped to work for. Thank you for the many, many lessons on research and writing. Thank you for both your critical eye, and for being supportive when research invariably gets difficult. Thank you for building a supportive research environment with good, good people, and being supportive of my individual goals in life. Every time I have asked advice about whether I should take on an extra side gig or try a new idea, you’ve always been the first to give a resounding, “YES, go for it!” And beyond work, thank you for supporting my love for travel. You have the coolest travel recommendations and stories of any person I have met.

Finally, I thank Aranya Goswami for being with me through the high points, the low points, and everything between. Come what may in research, you have always been my voice of reason and a source of encouragement. You encircle my life with love and support, and bring meaning to my days. Thank you for all our time together, spent cooking, making art messes, and traveling. Graduate school would not have been nearly as fun without our trips, whether abroad, or down the road to Anna’s Bakery.

VITA OF ALEX M. DOWNS

August 2021

EDUCATION

Doctor of Philosophy in Mechanical Engineering

University of California at Santa Barbara, August 2016 – August 2021

Graduate Certificates in: Management Practice, Bioengineering

Bachelor of Science in Biosystems Engineering

Minor in Materials Science & Engineering

The University of Arizona Honors College, August 2012 – May 2016

JOURNAL PUBLICATIONS

Downs, A.M., Gerson, J., Leung, K., Honeywell, K., Kippin, T., Plaxco, K.W. "Improved Calibration of Electrochemical Aptamer-Based Sensors." (In preparation).

Downs, A.M., Plaxco, K.W. "Review: Electrochemical Aptamer Based Sensors for In-body Monitoring." (In preparation).

Leung, K., **Downs, A.M**., Ortega, G., Kurnik, M., Plaxco, K.W. "Elucidating the mechanisms underlying the signal drift of electrochemical aptamer-based sensors in whole blood." *ACS Sensors*. 2021.

Downs, A.M., Gerson, J., Hossain, M.N., Ploense, K., Pham, M., Kraatz, H.B., Kippin, T., Plaxco, K.W. "Nanoporous Gold for the Miniaturization of In Vivo Electrochemical Aptamer-Based Sensors." *ACS Sensors*. 2021.

Downs, A.M., Gerson, J., Ploense, K., Plaxco, K.W., Dauphin-Ducharme, P. "Sub-second-resolved Molecular Measurements Using Electrochemical Phase Interrogation of Aptamer-Based Sensors." *Analytical Chemistry*. 2020.

Downs, A.M., McCallum, C., Pennathur, S. "Confinement Effects on DNA Hybridization in Electrokinetic Micro- and Nanofluidic Systems." *Electrophoresis*. 2019.

Gerson, J., Erdal, M., Dauphin-Ducharme, P., Idili, A., **Downs, A.M.**, Hespanha, J., Kippin, T., Plaxco, K.W. "An ultra-high precision view of intercompartmental drug transport via simultaneous, seconds-resolved measurements of vancomycin concentrations in the veins and brains of live rats." (In preparation).

Carroll, M.J., Goodall, C., Brown, N., **Downs, A. M**., Sheenan, T., and Anderson, K. "Honey bees preferentially consume freshly-stored pollen." *PLOS ONE*. 2017.

Abstract

Improving the accuracy and resolution of electrochemical aptamer-based sensors

Alex M. Downs

The ability to track the concentrations of specific molecules in the body in real time would vastly improve our ability to diagnose, understand, and treat disease. Most real-time molecular sensing technologies, however, rely on the adsorption of target to a receptor-modified surface. Because of this, they fail when challenged directly in complex biological media, such as whole blood. In such media, proteins, cells, and other interferents bind to the sensing interface, which leads to false positives or poor quantification. Electrochemical aptamer-based (EAB) sensors, in contrast, report on the concentration of their target via a binding-induced change in electron transfer from a redox reporter attached to a target-recognizing aptamer. They thus enable real-time molecular sensing directly in undiluted blood and even in situ in the living body. And because aptamers can be artificially selected for many target species, EAB sensors are a platform technology generalizable to a range of small molecules, metabolites, and proteins. Consistent with this, to date, EAB sensors have enabled real-time, in vivo measurements of numerous pharmaceuticals, drugs of abuse, and metabolites.

In this thesis, I described my work focused on the improvement of EAB sensor time resolution, spatial resolution, and accuracy. Specifically, I first detailed the application of the phase component of electrochemical impedance spectroscopy to push EAB time resolution to sub-second measurements. Then, with the aim of rendering them less invasive and improving their spatial resolution, I miniaturized the sensors by six-fold using nanoporous gold substrates. Finally, I improved the calibration used for in vivo quantification by examining how media selection, temperature, and age impact the accuracy of EAB sensor measurements.

TABLE OF CONTENTS

CHAPTER 1: INTRODUCTION

1.1 Motivation

The ability to track the concentrations of specific molecules in the body in real time would vastly improve our ability to monitor, treat, and study disease. For example, the continuous glucose monitor, which enables measurements of glucose in close to real time, is revolutionizing our ability to treat diabetes[1,2]. Likewise, after first appearing in surgical theaters in the 1980s, pulse oximeters have become a ubiquitous tool for monitoring health status[3] throughout hospitals and, under the pressure of the COVID pandemic, even at home[4]. Unfortunately, however, these two sensors are the sole commercially available devices supporting real-time, in vivo molecular monitoring. Given the promise of such time-resolved measurements, why do we not have widespread access to point of care or wearable sensors for a greater variety of molecules?

Biosensors, a class of technologies that exploit the molecular recognition properties of proteins and nucleic acids, have long been thought a potentially promising means of achieving continuous molecular monitoring. The majority of previously reported biosensors couple the presence of target to a change in system properties, such as mass, charge, optical signal, or acoustic signal. Because of this, they are highly sensitive to the non-specific binding of the cells and proteins present in bodily fluids. Consequently, few of the many architectures described in the biosensor literature have been demonstrated to function in whole blood in vitro, much less in the living body. In contrast, the limited techniques that do function in vivo, such as direct electrochemistry and certain enzymatic sensors, rely on the reactivity of the target itself. This limits them to a small set of biomarkers. Collectively, this has led to an impasse, where the few sensors that support molecular monitoring in vivo are not generalizable, and all of the generalizable sensing platforms fail when deployed in vivo.

The invention of electrochemical aptamer based (EAB) sensors has overcome this impasse. EAB sensors consist of redox-reporter modified aptamers attached to an electrode[5,6]. When the aptamer binds to its target, the rate of electron transfer from the redox reporter to the electrode surface changes because of the proximity of the redox reporter. This, in turn, can generate a change in electrochemical signal detectable by a range of analytical techniques, which can be converted into target concentration in real time. EAB sensors can perform molecular measurements in the living body because their surface-attached electrochemical recognition element enables sufficient fouling resistance to discern signal changes in flowing whole blood[7].

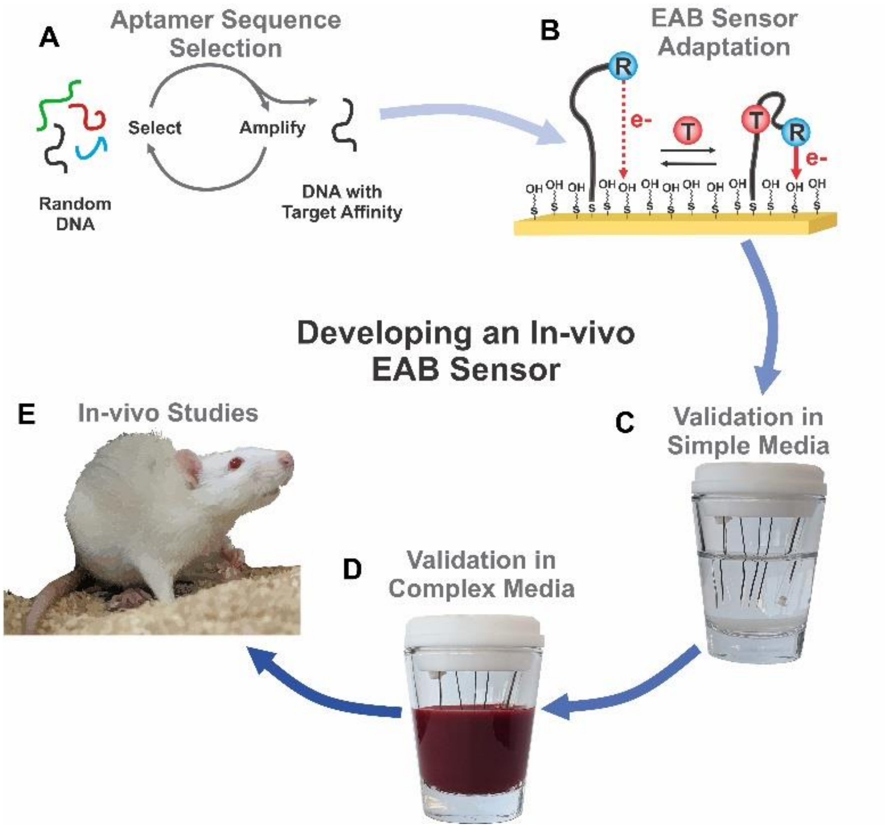

Figure 1: (A) To develop an in vivo EAB sensor, first an aptamer is selected for a given target using SELEX[8,9]. **(B)** Modifications to the selected aptamer, such as surface linkers, redox reporter tags, and changes to the aptamer sequence itself allow adaptation of an aptamer sequence into an EAB sensor. **(C)** Titrations in simple media, such as phosphate buffered saline, quantify response to target without the effect of biofouling. **(D)** Pending success in simple media, aptamer response is measured in the media that more closely reflects the in vivo environment (commonly, bovine blood for venous measurements, or cerebral spinal fluid for in-brain measurements). **(E)** If the sensor response aligns with the expected physiological target range, it may be applied for measurements in the living body.

Developing an EAB sensor and applying it in vivo requires a multi-step process that includes aptamer discovery, adaptation of the aptamer to the EAB platform, and validation of the sensor's performance in vitro and then in vivo. Aptamer selection is performed using an in-vitro discovery process called Systemic Evolution of Ligand

Exponential Enrichment, or “SELEX” (**Figure 1A**)[8,9]. To adapt a given aptamer sequence into an EAB sensor, an alkane thiol is attached for conjugation to the electrode, and a redox reporter is attached to generate an electrochemical signal (**Figure 1B**). If the selected aptamer doesn’t produce a large enough binding-induced conformational to generate a response to target addition, we “re-engineer” the aptamer by making small changes to its sequence. These changes include iterative removal of bases from the aptamer’s termini or movement of the redox reporter to other positions on the chain[10,11], which can increase the electrochemical signal response to target. After achieving a significant response to target, we characterize the EAB sensor’s response at different electrochemical interrogation conditions and target concentrations in simple media, such as phosphate buffered saline (**Figure 1C**). If the sensor produces sufficient signal change within a clinically-relevant range in simple media, the EAB sensor is again characterized in the appropriate biological fluid, such as undiluted blood or cerebral spinal fluid. (**Figure 1D**). Finally, if the sensor demonstrates a signal change in response to target within the clinically relevant range, then it can be applied the living body for real-time in vivo measurements (**Figure 1E**).

Below, I explore the strengths and weaknesses of the EAB sensing platform, placing particular focus on applications in vivo. I then discuss what I view as the opportunities and threats faced in their translation from an academic technique to a commercial platform to support clinically-relevant molecular monitoring.

1.2 Strengths

1.2a Generalizability

Because the aptamers themselves function independent of the electrochemical or enzymatic reactivity of their targets, EAB sensors are generalizable to a range of molecules and biomarkers. Consistent with this, dozens of EAB sensors have been described to date, with many more aptamer sequences having been reported but not yet adapted to the platform. Thus far, EAB sensors have demonstrated detection of targets ranging from pharmaceuticals and drugs of abuse, to proteins and metabolites[12,13]. EAB sensors have proven particularly useful for measurement of small molecule targets[7,14], and are among the only technologies capable of real-time measurement of specific proteins.

1.2b High-frequency, real-time molecular measurements

EAB sensors can monitor target concentrations in real time with excellent time resolution. Unlike immunoassays and sensors relying on free-solution redox reporters, for example, the assembly of a redox-reporter-modified aptamer into a surface assembled monolayer avoids the need for reagent addition or washing steps[5,6,15]. Because target binding to the aptamer portion of the EAB sensor typically is rapidly reversible, EAB sensors can measure rising and falling target concentrations in real time[16,17]. Indeed, under most circumstances, the rate-limiting step in EAB sensor operation is the electrochemical interrogation of the device (rather than the sensors rate of equilibration with the target). Thus, the platform’s time resolution depends only on the time required to perform its electrochemical interrogation. Using square wave voltammetry, for example, we achieve time resolutions of a few seconds to tens of seconds, depending on the square-wave frequencies required. In contrast, using techniques such as chronoamperometry[18], or intermittent pulse amperometry[19], and electrochemical impedance spectroscopy[20] can achieve sub-second time resolution. Thus, EAB sensor measurements are faster than most physiological processes, and are, thus, well-suited to monitoring rapid phenomena in the living body.

1.2c Performance in Undiluted Biological Media, and the Living Body

While many sensing platforms fail when challenged in biological fluids, EAB sensors are sufficiently insensitive to fouling that they support measurements in complex matrixes, such as undiluted whole blood. This is not to say that EAB sensors are unaffected by fouling altogether. Instead, fouling and other sensor-degradation phenomena contribute to a decline in signal when sensors are placed in vivo[21]. Fortunately, using interrogation techniques, such as square wave voltammetry, we can correct this drift. Specifically, by interrogating at distinct frequencies that drift at similar rates, subtraction of normalized peak signals can both correct for drift, and increase the magnitude of signal response[22].

The EAB platform is one of the few sensing technologies implemented directly in the living body, achieving hours-long measurements of a range of clinically important targets (**Table 1**). For example, they have demonstrated the real-time, seconds-resolved measurement of pharmaceuticals, such as antibiotics[7,10] and chemotherapeutics[7,23,24]. Likewise, they have measured drugs of abuse, such as cocaine[25], and metabolites, such as ATP and phenylalinine[12,13,26]. Using EAB sensors, researchers have achieved unprecedented, highly-time resolved measurement of drug delivery and clearance within the body. The ability to measure biomarker levels in the body creates exciting possibilities, such as personalized dosing of pharmaceuticals. Already, the ability to collect real-time measurements in the body has enabled feedback-controlled delivery of toxic, difficult-to-administer antibiotics[10,14].

Table 1: In vivo EAB sensors reported to date

Target	Target class	In vivo application	Duration
Vancomycin[10]	Antibiotic	Measurements in rat jugular vein, feedback controlled drug delivery in rat jugular vein	5 h
Tobramycin[14,18,27,28]	Antibiotic	Measurements in rat jugular vein. feedback controlled drug delivery in rat jugular vein	4 -11 h
Cocaine[25]	Drug of abuse	Measurements in rat brain	4.5 h
Kanamycin[26,28]	Antibiotic	Measurements in rat jugular vein	3 h
Phenylalinine[12]	Amino acid	Measurements in rat jugular vein	1 h
Doxorubicin[23,28]	Chemotherapeutic	Measurements in rat jugular vein	3 - 5 h
Adenine Triphosphate (ATP)[26]	Metabolite	Measurements in rat jugular vein	3 h
Irinotecan[24]	Chemotherapeutic	Measurements in rat jugular vein	2 h
Gentamicin[28]	Antibiotic	Measurements in rat jugular vein	4 h

1.2d Miniaturizable and Adaptable to Different Device Formats

EAB sensors are sufficiently small to implant in the body, and adaptable to a range of device architectures. Because EAB sensors require only a gold surface for adhesion, they can be implemented in both 3-dimensional formats, such as gold wires[7], and two dimensional platforms, such as electrodeposited planar substrates[29]. This makes them compatible for the surgical devices, well as microneedles and other wearable devices. For example, the in-vein measurements reported to date have mostly utilized a 230 µm diameter bundle of wires consisting of a sensor, a silver chloride reference electrode, and a platinum counter electrode[10]. In the future, performing measurements in other bodily locations, or targeting specific regions of a rat or mouse brain will require even smaller sensors. While sensor sizing represents a tradeoff between magnitude of electrochemical signal (which influences noise level in measurements) and macro-scale sensor dimensions, the sensors may be miniaturized further by increasing the microscopic surface area of the gold working electrode.

1.3 Weaknesses

1.3a Adaptation of Aptamer Sequences to EAB Sensors

The selection and subsequent adaptation of an aptamer into an EAB sensor can serve as chokeholds or barriers altogether to producing an in vivo sensor. SELEX identifies aptamers with binding typically demonstrated in free solution via optical or calorimetric methods[30,31]. When adapting these into EAB sensors, however, their signal gain (signal response relative to signal in absence of target) is sometimes small or even non-existent. Most often, this can be rectified by re-engineering the aptamer to undergo a large-scale, binding-induced conformational change using a number of rational or semi-rational approaches[10,32]. Typically, this requires addition or removal of bases from the aptamer. When adapting aptamer sequences into EAB sensors, the mid-point of the electrochemically observed binding curve often differs significantly from that reported for the unmodified, free-solution aptamer. Thus, there is risk associated with EAB sensor development, as an aptamer is not guaranteed to yield an EAB sensor that produces a strong signal response over the desired range of target concentrations.

1.3b Specificity

Many EAB sensors have been shown sufficiently selective to monitor their targets in vivo. That is, nothing naturally present in blood or other bodily fluids produces a significant signal response. Still, EAB sensors cannot be any more specific than the aptamer they employ and, thus, specificity is an inherent concern. Because aptamers are artificially selected to bind to a certain chemical group on a target, which can overlap with other targets, cross-reactivity can occur in both aptamers and their resulting EAB sensors. For example, cross-reactivity has been observed in the aminoglycoside sensor, which binds broadly to other antibiotics in this structural class, such as tobramycin, gentamycin, and kanamycin[7]. Likewise, an aptamer selected for the drug of abuse, cocaine, also responds to the anesthetic, procaine, the antimalarial, quinine, and the immunosuppressant, hydroxychloroquine[33]. This cross-reactivity mainly poses a challenge during in vivo monitoring if both compounds are present in the body at concentrations above each target's limit of detection. Application of EAB sensors to in vivo monitoring, then, requires an understanding of reactivity with structurally similar compounds likely to be present.

1.3c Measurement Duration

Of note, the majority of in vivo measurements to date have had durations below six hours. Primarily, this results from both animal use guidelines dictating that experiments under anesthesia do not exceed 6 h durations and sensor drift, which produces signal loss over time[21,23,33-35]. While correctable, ultimately signal drift poses a barrier to achieving long-duration measurements because no matter the efficacy of our drift correction, a sensor's signal-to-noise will eventual fall too low to support accurate quantification. Typically, this signal drift manifests as two distinct phases: an exponential signal decrease followed by a linear, sloping decrease[21]. Until recently, the sources of these two phases was poorly understood. Recent work, however, has shown that the more rapid exponential phase of signal drift results from fouling agents present in biological media, which decrease the electron transfer rate from the redox reporter to the electrode surface[21,33]. This exponential phase does not appear when interrogating in non-biological media, such as buffers. The linear drift phase, in contrast, results from the electrochemical interrogation[21]. When using square wave voltammetry, for example, a wider potential range (e.g., scanning below -0.4 V vs Ag|AgCl or above 0 V vs Ag|AgCl) leads to substantially more rapid linear drift[21], presumably due to reductive and oxidative desorption of the self-assembled monolayer[36].

While kinetic differential measurements reduce the impact of drift for in-vitro measurements as long as 24 h[21], they typically rely on finding square wave voltammetry frequencies that drift in concert. If the signal does not drift very closely in concert, it's possible to introduce sloping baselines and inaccurate quantifications. Not all interrogation frequencies yield currents that drift at the same rate, however. This poses a challenge for application of certain EAB sensors in vivo. Further, upon placement in whole blood, the electron transfer rate of EAB sensors shift, causing different drift behavior at disparate frequencies.

1.4 Opportunities

1.4a Improvement of SELEX

Recognizing the challenges in adapting aptamers to EAB sensors, there are opportunities to improve yield by making aptamer selection conditions match the desired environment of use more closely to the conditions of sensor operation conditions. It is logical that implementing variables during SELEX, such as body temperature conditions, physiologically-relevant buffers, or surface adherence, could improve the yield of sufficiently high-performance EAB sensors. Likewise, the use of non-natural oligomers could help improve affinity because it increases the chemical and structural diversity of possible aptamer sequences[37-39]. Finally, negative selections, whereby oligomers responding to structurally similar targets are bound and removed from the selection pool[40], could reduce undesirable cross-reactivity in aptamer sequences themselves.

1.4b Longer Duration Measurement Through Reduction or Elimination of Sensor Degradation

While we do not yet know how long EAB sensors last in vivo, it is clear that eventually, signal drift will pose a challenge to increased duration. Fortunately, however, there are many practical opportunities for improving, and possibly eliminating, the sensor degradation that produces this drift. These approaches include the use of more stable self-assembled monolayers, electrochemical interrogation approaches that cause less damage to the monolayer, and fouling-protecting coatings[41], antifouling monolayer head groups[23].

Maintaining good surface assembled monolayer integrity prevents both signal loss and overwhelming capacitative currents. Thus, monolayer selection is important for sensor drift behavior. Due to ease of use and ready availability, the majority of EAB sensor work to date has employed mercaptohexanol monolayers[35]. These offer a compromise between monolayer stability, which improves with the length of the alkane chain[42], and electron transfer, which slows as the monolayer becomes thicker[43]. Nevertheless, sensors fabricated using this monolayer drift considerably when challenged in whole blood due to fouling and loss of monolayer. Other monolayers appear to reduce these effects. For example, recent investigations have shown that a 1-hexanethiol monolayer better resists desorption and capacitance-linked loss of faradaic signal, even when challenged for 60 h in undiluted blood serum[35]. While stable, however, this monolayer substantially changes certain aptamers’ response to target[35]. Fortunately, the use of mixed mercaptohexanol and 1-hexanethiol monolayers appears to maintain both sensor response to target and long-term stability[35]. Another monolayer system containing a phosphatidylcholine head group has demonstrated good resistance to fouling-induced drift, while maintaining response to target[44]. With further investigation of the impact of scanning duration on measurement accuracy, these less-explored monolayer systems could enable longer duration measurements.

For the linear phase of drift associated with voltametric scanning, application of voltammetry that causes less oxidative/reductive desorption of monolayer can greatly reduce drift. As demonstrated recently for square wave voltammetry, confining the potential window between -0.2 to -0.4 V versus Ag|AgCl greatly reduces drift[21]. Applying techniques that scan very narrow potential windows about the methylene blue redox potential, such as in electrochemical impedance spectroscopy[20], may also reduce interrogation-driven drift.

For the exponential phase of drift associated with fouling agents, methods to control surface accessibility, such as surface membranes and coatings, could reduce drift. Application of hydrogel coatings, for example, can reduce fouling by excludes access of proteins of a given size. These approaches are most appropriate when sensing targets smaller than the pore size of the coating or membrane. And because these barriers can slow sensor response times, they work best in applications where seconds time resolution is not critical. In another approach, which does not impact response time, increasing the packing density of the DNA monolayer reduced enzyme-linked degradation[45]. Alternatively, recognizing that the signal loss with fouling plateaus after approximately 1 h[21], controlled pretreatment of sensors with known fouling agents could achieve more stable interfaces from the beginning of a measurement. Indeed, in a study of long-term EAB sensor storage, incubating EAB sensors in bovine serum albumin and glucose improved reproducibility of measurements[46] – suggesting such treatments that “pre-foul” the surface may improve overall interfacial stability for long duration measurements.

1.4c Applications

EAB sensors enable unprecedented opportunities to monitor molecules in real-time in the challenging in-vivo environment, and could produce innovations across both biomedical research and clinical practice.

As research tools, EAB sensors could greatly improve our understanding of metabolism, endocrinology, pharmacokinetics and neurochemistry. Specifically, EAB sensors could enable better time resolved, more quantitative measurements of phenomena such as neurotransmission, drug delivery and clearance, and responses to infection. Likewise, performing simultaneous EAB sensor measurements in multiple locations could enable a greater understanding of drug transport through and between bodily compartments, such as the muscles, brain, and subcutaneous space. In addition to in-body measurements, EAB sensors could prove particularly useful for real-time monitoring of cell cultures. To date, they have been used in microfluidic channels for monitoring of ATP release in astrocytes[41,47], and as glass nanopipettes for serotonin detection[47].

EAB sensors could also revolutionize our ability to detect, monitor, and treat disease. We envision, for example, the adaptation of the EAB sensing platform into a wearable device which, analogous to the continuous glucometer, can measure drugs and biomarkers indicative of health and disease in real-time. Where, then, could real-time, continuous monitoring improve disease treatment? For patients recovering from a surgery, monitoring infection biomarkers, such a C-reactive protein, could provide an early warning of onset of sepsis. Similarly, for patients with active infections of the kidney or urinary tract, monitoring infection biomarkers could help confirm efficacy of antibiotic treatment. And given that specific biomarkers, such as troponin, accompany heart attack onset, a wearable device could aid in early detection of heart attacks for individuals with high cardiac risk factors. Further, real-time sensing could provide impactful clinical applications for monitoring of allergic reactions, immune reactions, and metabolic diseases.

Finally, the ability to reliably measure molecules in the living body creates opportunities to improve the safety and efficacy of drug dosing through feedback-controlled delivery of medications. Today, the bulk of pharmaceutical dosing is performed based on assumptions of how an average person absorbs and responds to a drug. Each person, however, responds and metabolizes drugs in different ways, which can impact the efficacy of treatment. This can lead to consequences in terms of missed therapeutic window and even toxicity. Already, EAB sensors have been demonstrated in a rat model to support feedback-controlled delivery of the antibiotic, vancomycin[14]. In the future, EAB sensors could be used to guide dosage of high-risk pharmaceuticals, such as antibiotics, chemotherapeutics, and immunosuppressants. Currently, as a gold standard, we control the dosage of such medicines either with inconvenient hourly blood draws, or by waiting for harmful side effects to appear. By applying feedback-control to drug dosing, we may be able to improve the clinical benefit of medical treatments, while minimizing damage to the body.

1.5 Threats: Competing Technologies

Here, we define “threats” as technologies occupying a similar potential commercial space. Namely, we ask, “what competing technologies could fulfill the goals of continuous, long duration molecular monitoring in or at the interface of the body?”

1.5a Approaches Relying on Target Reactivity

Some sensing targets are electroactive at potentials that can be safely applied within the body. The oxidation and/or reduction of these species on an electrode allows for their direct detection via a change in electrochemical signal, typically via chronoamperometry, differential pulse voltammetry, or fast scan cyclic voltammetry[48-50]. A number of neurotransmitters are appropriately electroactive, such as dopamine, norepinephrine, epinephrine, histamine, serotonin, and adenosine[48,49]. Thus motivated, the neuroscience field has extensively applied direct electrochemistry for in vivo neurophysiological measurements, with the in vivo detection of dopamine[51,52] and serotonin[53]. Other electroactive compounds in the body include oxygen, nitric oxide, hydrogen peroxide and ascorbate[54,55]. While direct electrochemical detection in vivo is increasingly widespread, these measurements often suffer from poor sensitivity and specificity. For example, due to overlapping redox potentials, electroactive substances, such as ascorbic acid, can interfere with neurotransmitter detection[48]. Likewise, overlapping oxidation potentials can make it difficult to differentiate between compounds, including the neurotransmitters dopamine and serotonin[56]. Finally, when deployed in vivo, many electrochemical techniques are not sensitive enough to detect biological levels of neurotransmitters[56]. Collectively, these challenges make quantification of specific electroactive species difficult[57].

Enzymatic sensors, which instead rely on the enzymatic reactivity of a target, are among the only commercially-available molecular monitoring technologies capable of performing directly in blood or the body itself. As mentioned in the opening, the continuous glucose meter, which has revolutionized diabetes care, is one such example. Using an electrode implanted in the subcutaneous, this sensing strategy detects glucose via a the enzymatic conversion of the target to an eletroactive species, using enzymes such as glucose oxidase (GOx)[58]. Specifically, after GOx oxidizes glucose, becoming reduced itself, an electron mediator transports the resulting electrons to the working electrode, re-oxidizing the GOx. This creates a current that is measured using amperometry, in which a constant potential is applied between a working and counter electrode, and changes in current indicate presence of glucose oxidation. In addition to glucose, similar in vivo electrochemical enzymatic sensors have been described for the measurements of lactate[59], acetylcholine[60,61], and glutamate[54,55,62]. The further development of enzymatic is limited, primarily, by the lack of suitable enzymes, and secondarily, by instability or toxicity of mediator species[57], enzyme degradation in biological fluids[63], and interference from redox active species[64].

1.5b Optical Methods

Optical technologies relying on fluorescence, photoacoustics, and optogenetics can track biomarkers in the living body. Injectable optical sensors, for example, have been reported that use target binding to an optical reporter (ionophore, enzyme, or functionalized carbon nanotubes) to change either fluorescent or photoacoustic signal. These sensors require injection of photo-reactive, target-binding chemicals into the dermis, and have demonstrated in vivo detection of sodium[65], lithium[66], and histamine[67,68]. In contrast to electrochemical approaches, which often provide measurements at a single targeted location, optical methods often provide more spatially resolved measurements over a greater area. Nevertheless, this technique is not generalizable and faces substantial challenges for clinical application. Namely, results to date have failed to show robust in vivo quantification using the optical sensor output.

1.6 Conclusions

Table 2: Summary of EAB sensor platform strengths, weaknesses, opportunities, and threats

Strengths	Weaknesses	Opportunities	Threats
High-frequency, real-time measurements Generalizable to many targets Miniaturizable Works in blood and in living body	Iterative process of adaptating of aptamers into EAB sensors Specificity Measurement duration	Ongoing advances in aptamer selection New approaches to improving in vivo duration Adaptation to wearable devices	Other in vivo molecular sensing strategies: • Enzymatic • Direct Electrochemistry • Optical

EAB sensors are already a “class in their own” platform for quantitative in vivo measurements. This generalizable platform hosts a wealth of benefits, such as excellent time resolution, miniaturizability, and applicability to a range of device formats. While the platform faces challenges in terms of translation from aptamer discovery to EAB sensor development, this has not notably impeded to introduction of new, useful EAB sensors each year. Worth noting, the EAB sensing field is still in its emerging stages, and has yet to either develop market-ready products (like the glucometer) or widely applied research use (like direct electrochemistry of neurotransmitters). For this field to mature and yield reliable analytical tools, we need a greater understanding of interfacial stability and actively seek applications to reduce sensor drift. This is no surprise, however. The existing implantable glucometers rely on the use of selective membranes to mediate the effects of fouling. Thus, we believe that with the application of both electrochemical and interfacial methods to alleviate sensor drift, this technology could enable long-duration, time resolved measurements of a multitude of biomarkers.

1.6a Scope of Thesis Work

In the span of my work at UC Santa Barbara, I have aimed to improve and expand the applications of EAB sensors. With the goal of improving time resolution, I developed a technique that uses the phase component of impedance spectroscopy to report on target binding with sub-second resolution. This technique offers promise both for rapid in vivo measurements, as well as application in better understanding the dynamic EAB sensor interface. From there, I examined the question of sensor miniaturizability. Recognizing that increasing the microscopic surface area provides a path toward miniaturization, I produced nanoporous gold substrates on our existing wire sensors. After characterizing the sensor response with this new surface morphology, I applied the resulting increase in surface area to miniaturize our in vivo probes by 6-fold. In the future, this substrate could enable ultra-localized measurements with EAB sensors. Finally, through my own in vivo experiments and through assisting others with theirs, I realized the extent to which temperature impacts the EAB sensors' response. Thus motivated, I performed a comprehensive study of the factors impacting EAB sensor calibration, including temperature, blood age, the use of blood proxies.

1.7 References

(1) Rodbard, D. Continuous Glucose Monitoring: A Review of Successes, Challenges, and Opportunities. *Diabetes Technology & Therapeutics* **2016**, *18*, S2-3-S2-13, 10.1089/dia.2015.0417.
(2) Klonoff, D. C.; Ahn, D.; Drincic, A. Continuous glucose monitoring: A review of the technology and clinical use. *Diabetes Research and Clinical Practice* **2017**, *133*, 178-192, 10.1016/j.diabres.2017.08.005.
(3) Sinex, J. E. Pulse oximetry: Principles and limitations. *The American Journal of Emergency Medicine* **1999**, *17*, 59-66, 10.1016/S0735-6757(99)90019-0.
(4) Shah, S.; Majmudar, K.; Stein, A.; Gupta, N.; Suppes, S.; Karamanis, M.; Capannari, J.; Sethi, S.; Patte, C. Novel Use of Home Pulse Oximetry Monitoring in COVID-19 Patients Discharged From the Emergency Department Identifies Need for Hospitalization. **2020**, *27*, 681-692, 10.1111/acem.14053.
(5) Xiao, Y.; Lai, R. Y.; Plaxco, K. W. Preparation of electrode-immobilized, redox-modified oligonucleotides for electrochemical DNA and aptamer-based sensing. *Nature Protocols* **2007**, *2*, 2875-2880, 10.1038/nprot.2007.413.
(6) Xiao, Y.; Lubin, A. A.; Heeger, A. J.; Plaxco, K. W. Label-Free Electronic Detection of Thrombin in Blood Serum by Using an Aptamer-Based Sensor. **2005**, *44*, 5456-5459, 10.1002/anie.200500989.
(7) Arroyo-Currás, N.; Somerson, J.; Vieira, P. A.; Ploense, K. L.; Kippin, T. E.; Plaxco, K. W. Real-time measurement of small molecules directly in awake, ambulatory animals. *Proceedings of the National Academy of Sciences* **2017**, *114*, 645-650, 10.1073/pnas.1613458114.
(8) Ellington, A. D.; Szostak, J. W. In vitro selection of RNA molecules that bind specific ligands. *Nature* **1990**, *346*, 818-822, 10.1038/346818a0.
(9) Tuerk, C.; Gold, L. Systematic evolution of ligands by exponential enrichment: RNA ligands to bacteriophage T4 DNA polymerase. *Science* **1990**, *249*, 505, 10.1126/science.2200121.
(10) Dauphin-Ducharme, P.; Yang, K.; Arroyo-Currás, N.; Ploense, K. L.; Zhang, Y.; Gerson, J.; Kurnik, M.; Kippin, T. E.; Stojanovic, M. N.; Plaxco, K. W. Electrochemical Aptamer-Based Sensors for Improved Therapeutic Drug Monitoring and High-Precision, Feedback-Controlled Drug Delivery. *ACS sensors* **2019**, *4*, 2832-2837, 10.1021/acssensors.9b01616.
(11) Mayer, M. D.; Lai, R. Y. Effects of redox label location on the performance of an electrochemical aptamer-based tumor necrosis factor-alpha sensor. *Talanta* **2018**, *189*, 585-591, 10.1016/j.talanta.2018.07.055.
(12) Idili, A.; Gerson, J.; Kippin, T.; Plaxco, K. W. Seconds-Resolved, In Situ Measurements of Plasma Phenylalanine Disposition Kinetics in Living Rats. *Analytical Chemistry* **2021**, *93*, 4023-4032, 10.1021/acs.analchem.0c05024.
(13) Idili, A.; Parolo, C.; Ortega, G.; Plaxco, K. W. Calibration-Free Measurement of Phenylalanine Levels in the Blood Using an Electrochemical Aptamer-Based Sensor Suitable for Point-of-Care Applications. *ACS Sensors* **2019**, *4*, 3227-3233, 10.1021/acssensors.9b01703.
(14) Arroyo-Currás, N.; Ortega, G.; Copp, D. A.; Ploense, K. L.; Plaxco, Z. A.; Kippin, T. E.; Hespanha, J. P.; Plaxco, K. W. High-Precision Control of Plasma Drug Levels

Using Feedback-Controlled Dosing. *ACS Pharmacology & Translational Science* **2018**, *1*, 110-118, 10.1021/acsptsci.8b00033.
(15) White, R. J.; Plaxco, K. W. Exploiting Binding-Induced Changes in Probe Flexibility for the Optimization of Electrochemical Biosensors. *Analytical Chemistry* **2010**, *82*, 73-76, 10.1021/ac902595f.
(16) Xiao, Y.; Lubin, A. A.; Heeger, A. J.; Plaxco, K. W. Label-free electronic detection of thrombin in blood serum by using an aptamer-based sensor. *Angewandte Chemie (International ed. in English)* **2005**, *44*, 5456-5459, 10.1002/anie.200500989.
(17) Baker, B. R.; Lai, R. Y.; Wood, M. S.; Doctor, E. H.; Heeger, A. J.; Plaxco, K. W. An Electronic, Aptamer-Based Small-Molecule Sensor for the Rapid, Label-Free Detection of Cocaine in Adulterated Samples and Biological Fluids. *Journal of the American Chemical Society* **2006**, *128*, 3138-3139, 10.1021/ja056957p.
(18) Arroyo-Currás, N.; Dauphin-Ducharme, P.; Ortega, G.; Ploense, K. L.; Kippin, T. E.; Plaxco, K. W. Subsecond-Resolved Molecular Measurements in the Living Body Using Chronoamperometrically Interrogated Aptamer-Based Sensors. *ACS Sensors* **2018**, *3*, 360-366, 10.1021/acssensors.7b00787.
(19) Santos-Cancel, M.; Lazenby, R. A.; White, R. J. Rapid Two-Millisecond Interrogation of Electrochemical, Aptamer-Based Sensor Response Using Intermittent Pulse Amperometry. *ACS Sensors* **2018**, *3*, 1203-1209, 10.1021/acssensors.8b00278.
(20) Downs, A. M.; Gerson, J.; Ploense, K. L.; Plaxco, K. W.; Dauphin-Ducharme, P. Subsecond-Resolved Molecular Measurements Using Electrochemical Phase Interrogation of Aptamer-Based Sensors. *Analytical Chemistry* **2020**, *92*, 14063-14068, 10.1021/acs.analchem.0c03109.
(21) Leung, K.; Downs, A.; Ortega, G.; Kurnik, M.; Plaxco, K. Elucidating the mechanisms underlying the signal drift of electrochemical aptamer-based sensors in whole blood. *Submitted to ACS Sensors* **2021**,
(22) Ferguson, B. S.; Hoggarth, D. A.; Maliniak, D.; Ploense, K.; White, R. J.; Woodward, N.; Hsieh, K.; Bonham, A. J.; Eisenstein, M.; Kippin, T. E.; Plaxco, K. W.; Soh, H. T. Real-Time, Aptamer-Based Tracking of Circulating Therapeutic Agents in Living Animals. *Science translational medicine* **2013**, *5*, 213ra165, 10.1126/scitranslmed.3007095.
(23) Li, H.; Dauphin-Ducharme, P.; Arroyo-Currás, N.; Tran, C. H.; Vieira, P. A.; Li, S.; Shin, C.; Somerson, J.; Kippin, T. E.; Plaxco, K. W. A Biomimetic Phosphatidylcholine-Terminated Monolayer Greatly Improves the In Vivo Performance of Electrochemical Aptamer-Based Sensors. **2017**, *56*, 7492-7495, 10.1002/anie.201700748.
(24) Idili, A.; Arroyo-Currás, N.; Ploense, K. L.; Csordas, A. T.; Kuwahara, M.; Kippin, T. E.; Plaxco, K. W. Seconds-resolved pharmacokinetic measurements of the chemotherapeutic irinotecan in situ in the living body. *Chemical Science* **2019**, *10*, 8164-8170, 10.1039/C9SC01495K.
(25) Taylor, I. M.; Du, Z.; Bigelow, E. T.; Eles, J. R.; Horner, A. R.; Catt, K. A.; Weber, S. G.; Jamieson, B. G.; Cui, X. T. Aptamer-functionalized neural recording electrodes for the direct measurement of cocaine in vivo. *Journal of Materials Chemistry B* **2017**, *5*, 2445-2458, 10.1039/C7TB00095B.

(26) Li, H.; Li, S.; Dai, J.; Li, C.; Zhu, M.; Li, H.; Lou, X.; Xia, F.; Plaxco, Kevin W. High frequency, calibration-free molecular measurements in situ in the living body. *Chemical Science* **2019**, *10*, 10843-10848, 10.1039/C9SC04434E.
(27) Vieira, P. A.; Shin, C. B.; Arroyo-Currás, N.; Ortega, G.; Li, W.; Keller, A. A.; Plaxco, K. W.; Kippin, T. E. Ultra-High-Precision, in-vivo Pharmacokinetic Measurements Highlight the Need for and a Route Toward More Highly Personalized Medicine. **2019**, *6*, 10.3389/fmolb.2019.00069.
(28) Arroyo-Currás, N.; Somerson, J.; Vieira, P. A.; Ploense, K. L.; Kippin, T. E.; Plaxco, K. W. Real-time measurement of small molecules directly in awake, ambulatory animals. **2017**, *114*, 645-650, 10.1073/pnas.1613458114 %J Proceedings of the National Academy of Sciences.
(29) Shin, S. R.; Zhang, Y. S.; Kim, D.-J.; Manbohi, A.; Avci, H.; Silvestri, A.; Aleman, J.; Hu, N.; Kilic, T.; Keung, W.; Righi, M.; Assawes, P.; Alhadrami, H. A.; Li, R. A.; Dokmeci, M. R.; Khademhosseini, A. Aptamer-Based Microfluidic Electrochemical Biosensor for Monitoring Cell-Secreted Trace Cardiac Biomarkers. *Analytical Chemistry* **2016**, *88*, 10019-10027, 10.1021/acs.analchem.6b02028.
(30) Lin, P.-H.; Chen, R.-H.; Lee, C.-H.; Chang, Y.; Chen, C.-S.; Chen, W.-Y. Studies of the binding mechanism between aptamers and thrombin by circular dichroism, surface plasmon resonance and isothermal titration calorimetry. *Colloids and Surfaces B: Biointerfaces* **2011**, *88*, 552-558, 10.1016/j.colsurfb.2011.07.032.
(31) Nakatsuka, N.; Yang, K.-A.; Abendroth, J. M.; Cheung, K. M.; Xu, X.; Yang, H.; Zhao, C.; Zhu, B.; Rim, Y. S.; Yang, Y.; Weiss, P. S.; Stojanović, M. N.; Andrews, A. M. Aptamer–field-effect transistors overcome Debye length limitations for small-molecule sensing. **2018**, *362*, 319-324, 10.1126/science.aao6750 %J Science.
(32) Parolo, C.; Idili, A.; Ortega, G.; Csordas, A.; Hsu, A.; Arroyo-Currás, N.; Yang, Q.; Ferguson, B. S.; Wang, J.; Plaxco, K. W. Real-Time Monitoring of a Protein Biomarker. *ACS sensors* **2020**, *5*, 1877-1881, 10.1021/acssensors.0c01085.
(33) Shaver, A.; Kundu, N.; Young, B. E.; Vieira, P. A.; Sczepanski, J. T.; Arroyo-Currás, N. Nuclease Hydrolysis Does Not Drive the Rapid Signaling Decay of DNA Aptamer-Based Electrochemical Sensors in Biological Fluids. *Langmuir* **2021**, *37*, 5213-5221, 10.1021/acs.langmuir.1c00166.
(34) Li, H.; Arroyo-Currás, N.; Kang, D.; Ricci, F.; Plaxco, K. W. Dual-Reporter Drift Correction To Enhance the Performance of Electrochemical Aptamer-Based Sensors in Whole Blood. *Journal of the American Chemical Society* **2016**, *138*, 15809-15812, 10.1021/jacs.6b08671.
(35) Shaver, A.; Curtis, S. D.; Arroyo-Currás, N. Alkanethiol Monolayer End Groups Affect the Long-Term Operational Stability and Signaling of Electrochemical, Aptamer-Based Sensors in Biological Fluids. *ACS Applied Materials & Interfaces* **2020**, *12*, 11214-11223, 10.1021/acsami.9b22385.
(36) Wackerbarth, H.; Grubb, M.; Zhang, J.; Hansen, A. G.; Ulstrup, J. Long-Range Order of Organized Oligonucleotide Monolayers on Au(111) Electrodes. *Langmuir* **2004**, *20*, 1647-1655, 10.1021/la035547g.
(37) Kimoto, M.; Yamashige, R.; Matsunaga, K.-i.; Yokoyama, S.; Hirao, I. Generation of high-affinity DNA aptamers using an expanded genetic alphabet. *Nature Biotechnology* **2013**, *31*, 453-457, 10.1038/nbt.2556.

(38) Gawande, B. N.; Rohloff, J. C.; Carter, J. D.; von Carlowitz, I.; Zhang, C.; Schneider, D. J.; Janjic, N. Selection of DNA aptamers with two modified bases. **2017**, *114*, 2898-2903, 10.1073/pnas.1615475114 %J Proceedings of the National Academy of Sciences.
(39) Kalra, P.; Dhiman, A.; Cho, W. C.; Bruno, J. G.; Sharma, T. K. Simple Methods and Rational Design for Enhancing Aptamer Sensitivity and Specificity. **2018**, *5*, 10.3389/fmolb.2018.00041.
(40) Yang, K.-A.; Pei, R.; Stojanovic, M. N. In vitro selection and amplification protocols for isolation of aptameric sensors for small molecules. *Methods* **2016**, *106*, 58-65, 10.1016/j.ymeth.2016.04.032.
(41) Santos-Cancel, M.; Simpson, L. W.; Leach, J. B.; White, R. J. Direct, Real-Time Detection of Adenosine Triphosphate Release from Astrocytes in Three-Dimensional Culture Using an Integrated Electrochemical Aptamer-Based Sensor. *ACS chemical neuroscience* **2019**, *10*, 2070-2079, 10.1021/acschemneuro.9b00033.
(42) White, R. J.; Phares, N.; Lubin, A. A.; Xiao, Y.; Plaxco, K. W. Optimization of Electrochemical Aptamer-Based Sensors via Optimization of Probe Packing Density and Surface Chemistry. *Langmuir* **2008**, *24*, 10513-10518, 10.1021/la800801v.
(43) Lai, R. Y.; Seferos, D. S.; Heeger, A. J.; Bazan, G. C.; Plaxco, K. W. Comparison of the Signaling and Stability of Electrochemical DNA Sensors Fabricated from 6- or 11-Carbon Self-Assembled Monolayers. *Langmuir* **2006**, *22*, 10796-10800, 10.1021/la0611817.
(44) Li, H.; Dauphin-Ducharme, P.; Arroyo-Currás, N.; Tran, C. H.; Vieira, P. A.; Li, S.; Shin, C.; Somerson, J.; Kippin, T. E.; Plaxco, K. W. A Biomimetic Phosphatidylcholine-Terminated Monolayer Greatly Improves the In Vivo Performance of Electrochemical Aptamer-Based Sensors. *Angewandte Chemie (International ed. in English)* **2017**, *56*, 7492-7495, 10.1002/anie.201700748.
(45) Deng, M.; Li, M.; Li, F.; Mao, X.; Li, Q.; Shen, J.; Fan, C.; Zuo, X. Programming Accessibility of DNA Monolayers for Degradation-Free Whole-Blood Biosensors. *ACS Materials Letters* **2019**, *1*, 671-676, 10.1021/acsmaterialslett.9b00404.
(46) Lai, R. Y.; Seferos, D. S.; Heeger, A. J.; Bazan, G. C.; Plaxco, K. W. Comparison of the signaling and stability of electrochemical DNA sensors fabricated from 6- or 11-carbon self-assembled monolayers. *Langmuir* **2006**, *22*, 10796-10800, 10.1021/la0611817.
(47) Nakatsuka, N.; Heard, K. J.; Faillétaz, A.; Momotenko, D.; Vörös, J.; Gage, F. H.; Vadodaria, K. C. Sensing serotonin secreted from human serotonergic neurons using aptamer-modified nanopipettes. *Molecular psychiatry* **2021**, 10.1038/s41380-021-01066-5.
(48) Robinson, D. L.; Hermans, A.; Seipel, A. T.; Wightman, R. M. Monitoring Rapid Chemical Communication in the Brain. *Chemical Reviews* **2008**, *108*, 2554-2584, 10.1021/cr068081q.
(49) Bucher, E. S.; Wightman, R. M. Electrochemical Analysis of Neurotransmitters. *Annu Rev Anal Chem (Palo Alto Calif)* **2015**, *8*, 239-261, 10.1146/annurev-anchem-071114-040426.
(50) Roberts, J. G.; Sombers, L. A. Fast-Scan Cyclic Voltammetry: Chemical Sensing in the Brain and Beyond. *Analytical Chemistry* **2018**, *90*, 490-504, 10.1021/acs.analchem.7b04732.

(51) Rodeberg, N. T.; Sandberg, S. G.; Johnson, J. A.; Phillips, P. E. M.; Wightman, R. M. Hitchhiker's Guide to Voltammetry: Acute and Chronic Electrodes for in Vivo Fast-Scan Cyclic Voltammetry. *ACS Chemical Neuroscience* **2017**, *8*, 221-234, 10.1021/acschemneuro.6b00393.
(52) Clark, J. J.; Sandberg, S. G.; Wanat, M. J.; Gan, J. O.; Horne, E. A.; Hart, A. S.; Akers, C. A.; Parker, J. G.; Willuhn, I.; Martinez, V.; Evans, S. B.; Stella, N.; Phillips, P. E. M. Chronic microsensors for longitudinal, subsecond dopamine detection in behaving animals. *Nat Methods* **2010**, *7*, 126-129, 10.1038/nmeth.1412.
(53) Swamy, B. E. K.; Venton, B. J. Carbon nanotube-modified microelectrodes for simultaneous detection of dopamine and serotoninin vivo. *Analyst* **2007**, *132*, 876-884, 10.1039/B705552H.
(54) Ferreira, N. R.; Ledo, A.; Laranjinha, J.; Gerhardt, G. A.; Barbosa, R. M. Simultaneous measurements of ascorbate and glutamate in vivo in the rat brain using carbon fiber nanocomposite sensors and microbiosensor arrays. *Bioelectrochemistry* **2018**, *121*, 142-150, 10.1016/j.bioelechem.2018.01.009.
(55) Weltin, A.; Kieninger, J.; Enderle, B.; Gellner, A.-K.; Fritsch, B.; Urban, G. A. Polymer-based, flexible glutamate and lactate microsensors for in vivo applications. *Biosensors and Bioelectronics* **2014**, *61*, 192-199, 10.1016/j.bios.2014.05.014.
(56) O'Neill, R. D. Microvoltammetric techniques and sensors for monitoring neurochemical dynamics in vivo. A review. *The Analyst* **1994**, *119*, 767-779, 10.1039/AN9941900767.
(57) Tan, C.; Robbins, E. M.; Wu, B.; Cui, X. T. Recent Advances in In Vivo Neurochemical Monitoring. *Micromachines* **2021**, *12*, 10.3390/mi12020208.
(58) Teymourian, H.; Barfidokht, A.; Wang, J. Electrochemical glucose sensors in diabetes management: an updated review (2010–2020). *Chemical Society Reviews* **2020**, *49*, 7671-7709, 10.1039/D0CS00304B.
(59) Wolf, A.; Renehan, K.; Ho, K. K. Y.; Carr, B. D.; Chen, C. V.; Cornell, M. S.; Ye, M.; Rojas-Peña, A.; Chen, H. Evaluation of Continuous Lactate Monitoring Systems within a Heparinized In Vivo Porcine Model Intravenously and Subcutaneously. *Biosensors (Basel)* **2018**, *8*, 122, 10.3390/bios8040122.
(60) Burmeister, J. J.; Pomerleau, F.; Huettl, P.; Gash, C. R.; Werner, C. E.; Bruno, J. P.; Gerhardt, G. A. Ceramic-based multisite microelectrode arrays for simultaneous measures of choline and acetylcholine in CNS. *Biosensors and Bioelectronics* **2008**, *23*, 1382-1389, 10.1016/j.bios.2007.12.013.
(61) Bruno, J. P.; Gash, C.; Martin, B.; Zmarowski, A.; Pomerleau, F.; Burmeister, J.; Huettl, P.; Gerhardt, G. A. Second-by-second measurement of acetylcholine release in prefrontal cortex. **2006**, *24*, 2749-2757, 10.1111/j.1460-9568.2006.05176.x.
(62) Naylor, E.; Aillon, D. V.; Gabbert, S.; Harmon, H.; Johnson, D. A.; Wilson, G. S.; Petillo, P. A. Simultaneous real-time measurement of EEG/EMG and L-glutamate in mice: A biosensor study of neuronal activity during sleep. *J Electroanal Chem (Lausanne)* **2011**, *656*, 106-113, 10.1016/j.jelechem.2010.12.031.
(63) Rocchitta, G.; Spanu, A.; Babudieri, S.; Latte, G.; Madeddu, G.; Galleri, G.; Nuvoli, S.; Bagella, P.; Demartis, M.; Fiore, V.; Manetti, R.; Serra, P. Analytical Problems in Exposing Amperometric Enzyme Biosensors to Biological Fluids. *Sensors* **2016**, *16*, 780, 10.3390/s16060780.

(64) Soto, R. J.; Hall, J. R.; Brown, M. D.; Taylor, J. B.; Schoenfisch, M. H. In Vivo Chemical Sensors: Role of Biocompatibility on Performance and Utility. *Analytical Chemistry* **2017**, *89*, 276-299, 10.1021/acs.analchem.6b04251.
(65) Dubach, J. M.; Lim, E.; Zhang, N.; Francis, K. P.; Clark, H. In vivo sodium concentration continuously monitored with fluorescent sensors. *Integrative Biology* **2011**, *3*, 142-148, 10.1039/c0ib00020e.
(66) Cash, K. J.; Li, C.; Xia, J.; Wang, L. V.; Clark, H. A. Optical Drug Monitoring: Photoacoustic Imaging of Nanosensors to Monitor Therapeutic Lithium in Vivo. *ACS Nano* **2015**, *9*, 1692-1698, 10.1021/nn5064858.
(67) Cash, K. J.; Clark, H. A. In vivo histamine optical nanosensors. *Sensors (Basel)* **2012**, *12*, 11922-11932, 10.3390/s120911922.
(68) Cash, K. J.; Clark, H. A. Phosphorescent Nanosensors for in Vivo Tracking of Histamine Levels. *Analytical Chemistry* **2013**, *85*, 6312-6318, 10.1021/ac400575u.

CHAPTER 2: SUB-SECOND-RESOLVED MOLECULAR MEASUREMENTS USING ELECTROCHEMICAL PHASE INTERROGATION OF APTAMER-BASED SENSORS

2.1 ABSTRACT

Recent years have seen the development of a number of biosensor architectures that rely on target binding-induced changes in the rate of electron transfer from an electrode-bound receptor. Most often, the interrogation of these sensors has relied on voltammetric methods, such as square-wave voltammetry, which limit their time resolution to a few seconds. Here, we describe the use of an impedance-based approach, which we have termed electrochemical phase interrogation, as a means of interrogating sensors in this class with high time resolution. Specifically, using changes in the electrochemical phase to monitor target binding in an electrochemical-aptamer based sensor, we achieve sub-second temporal resolution and multi-hour stability in measurements performed directly in undiluted whole blood. Electrochemical phase interrogation also offers improved insights into EAB sensors' signaling mechanism. By modeling the interfacial resistance and capacitance using equivalent circuits, we find that the only parameter that is altered by target binding is the charge transfer resistance. This confirms previous claims that binding-induced changes in electron transfer kinetics drive signaling in this class of sensors. Considering that a wide range of electrochemical biosensor architectures rely on this signaling mechanism, we believe that electrochemical phase interrogation may prove generalizable towards sub-second measurements of molecular targets.

2.2 INTRODUCTION

Prior studies of EAB sensors have almost exclusively applied square wave voltammetry to measure target binding-induced changes in electron transfer. In square wave voltammetry, a ramping staircase square wave potential scans across the redox reporter's potential window, where changes in electron transfer lead to corresponding changes in the peak height of the voltammogram[1]. Because its waveform reduces the contribution of the electric double layer to the current, this approach provides superior measurement sensitivity[2]. Due to the time required to perform a full square-wave scan, however, the time resolution of this approach is often limited from seconds to tens of seconds. This renders the approach too slow to resolve biological processes, such as neurotransmission, which occur on sub-second time scales.

In contrast to voltammetric approaches, electrochemical impedance measurements can achieve sub-second interrogation times. This is because the approach directly measures changes in interfacial surface properties (i.e., charge transfer and electric double layer formation) rapidly via an applied sinusoidally oscillating (alternating current; AC) potential pulse. Changes in interfacial surface properties have been either measured: 1) "faradaically" using a free in solution redox reporter (typically $Fe(CN)_6^{3-/4-}$) that changes its charge transfer ability due to steric or electrostatic blocking of a functionalized electrode[3], or 2) "non-faradaically" by detecting target binding via changes in the functionalized electrode electric double layer[3]. Despite the popularity of these approaches in the scientific literature, target quantification fails in realistically complex sample matrices (i.e., undiluted serum or blood samples), presumably because the signal change generated by fouling mimics the change produced by target binding[3,4].

Here, we demonstrate a method of impedimetrically interrogating EAB sensors (**Figure 1A**) that is remarkably insensitive to non-specific adsorption, allowing for continuous sub-second-resolved, real-time measurements over long durations in undiluted whole blood. To achieve this, our approach monitors the phase shift of the current response produced by a redox (faradaic) reporter that is covalently attached to the receptor rather than free in solution. A binding-induced change in the conformation of the receptor alters the rate of electron transfer from the reporter, producing an easily measurable change in phase shift.

2.3 RESULTS

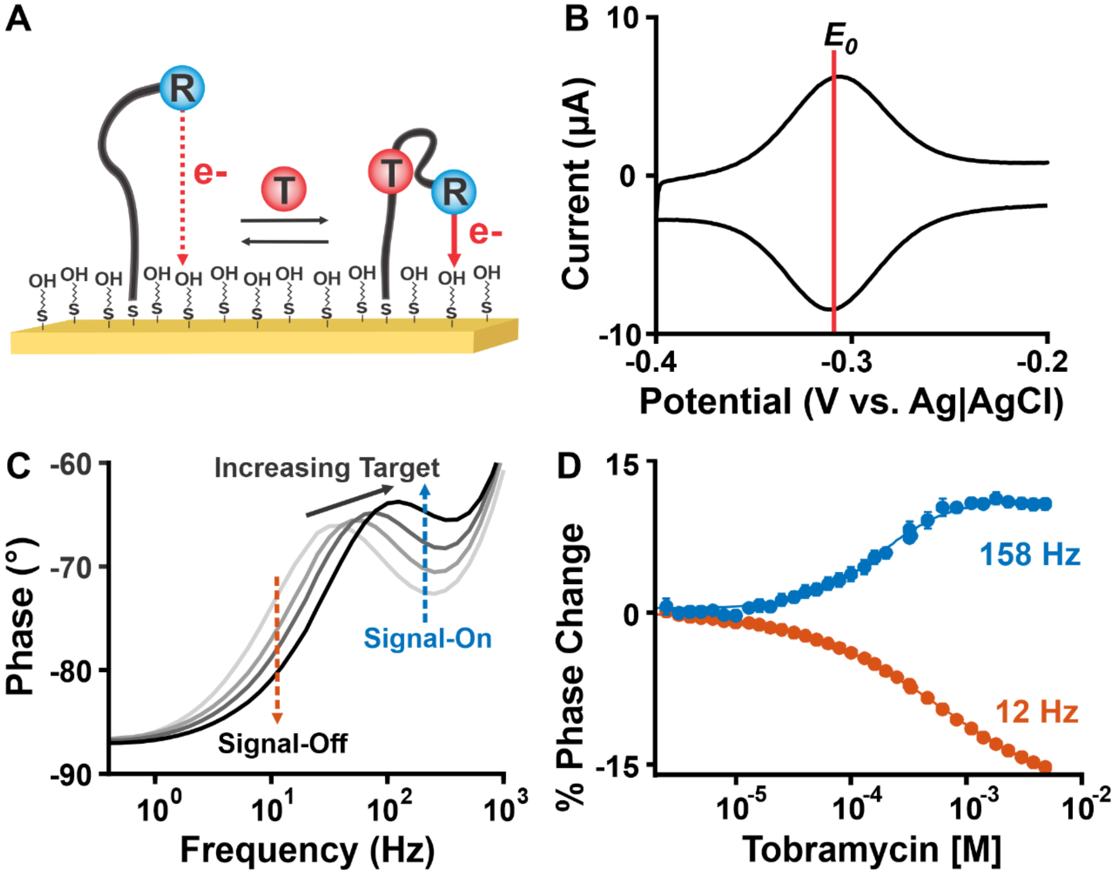

Figure 1. (**A**) EAB sensors consist of a gold electrode coated with a passivating self-assembled monolayer (here 6-mercapto-1-hexanol) and redox reporter-modified (R) aptamers. Signaling in this class of sensors occurs via a binding-induced change in electron transfer kinetics of the redox reporter. In this work, we have employed an aptamer that binds to the aminoglycoside antibiotic, tobramycin. (**B**) Interrogating the EAB sensor using cyclic voltammetry produces the reversible, surface-bound electrochemical reaction expected from the redox reporter with peaks at the standard reduction potential of methylene blue (E_0). (**C**) We measure changes in electron transfer kinetics by acquiring a phase spectroscopy scan when polarizing the EAB sensor at E_0 and exposing it to increasing amounts of tobramycin in undiluted whole blood. We observe a phase shift towards higher frequencies as the rate of electron transfer from the redox reporter increases upon target binding. This leads to a decrease in phase shift at low frequencies (“signal-off” behavior) and an increase in phase shift at higher frequencies (“signal-on” behavior). (**D**) Correspondingly, when performing alternating electrochemical phase measurements at 12 and 158 Hz (orange and blue traces) we observe binding curves that reach phase changes of -15% and +15% at target saturation. The error bars in panel D (which are smaller than the marker size) indicate standard deviation derived from 4 independently fabricated and interrogated sensors.

Electrochemical phase interrogation of EAB sensors reports on target concentration. To demonstrate this, we employed an EAB sensor that detects aminoglycoside antibiotics, including tobramycin[5]. To measure the full frequency dependence of the sensor’s phase response, we applied sinusoidally-oscillating potential wave forms of varying frequencies centered around the formal reduction potential, E_0, (**Figure 1B**) of the methylene blue redox reporter and measured the resulting shift in phase of the current response. In the absence of target, we observe a phase peak at ~25 Hz (**Figure 1C**, light grey curve). The addition of tobramycin causes this peak to shift to higher frequencies (**Figure 1C**, progressively darker curves) where the measured phase increases toward 0° at higher frequencies ("signal-on") and decreases toward -90° at lower frequencies ("signal-off"). Performing full titrations at both signal-on and off AC frequencies (12 and 158 Hz, respectively), we observe binding curves with dissociation constants of ~380 mM and ±15% changes in phase at saturating target (**Figure 1D**).

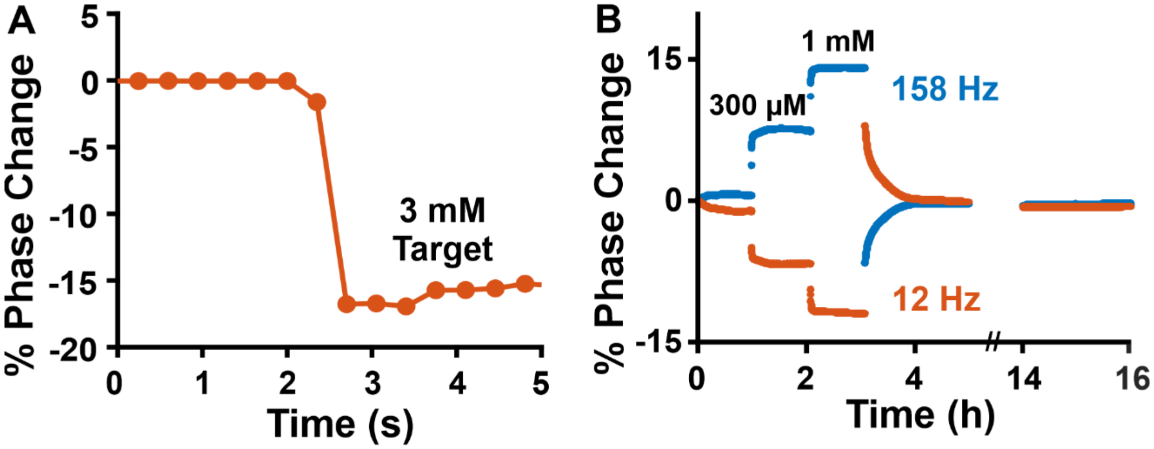

Figure 2. Electrochemical phase interrogation of EAB sensors achieve few hundred milliseconds time resolution and remain stable in whole blood for many hours. (**A**) To illustrate sub-second time resolution, we continuously interrogate the EAB sensor at a signal-off frequency of 12 Hz and spike the phosphate buffer saline solution with saturating amounts of tobramycin (3 mM). (**B**) Electrochemical phase spectroscopy enables measurements in undiluted whole blood for multi-hour time periods. To demonstrate this, here we immersed EAB sensors in undiluted whole blood over 16 h, and sequentially interrogated them at the AC frequencies indicated. As shown, we added 300 mM, then 1 mM tobramycin to the blood before then returning the sensor to target-free blood.

Electrochemical phase interrogation supports sub-second-resolved real-time EAB measurements. To demonstrate this, we interrogated the EAB sensor using a 12 Hz

AC pulse during the addition of 3 mM tobramycin. The time resolution of the resulting measurements, which is defined here by the data acquisition software rather than the physics of the system, is 416 ms (**Figure 2A**). This already represents a 1 to 2 orders of magnitude improvement in measurement frequency over EAB sensors interrogated using square-wave voltammetry, but could be improved further with faster processing electronics than those we have employed. For example, if a pulse of a single period is collected, the time resolution achievable using a pulse of frequency 158 Hz should approach 6 ms. In addition to read-out timescale, several factors can limit time resolution. These include mixing time to achieve sample homogeneity and diffusion of the target to the sensor surface. Thus, while in PBS, the sensor's signal rapidly stabilizes upon a change in target concentration (**Figure 2A**), it requires more time in whole blood (**Figure 2B**), which is far more viscous. When the whole blood is rapidly homogenized, in contrast, our sensor's signal stabilizes faster than shown in Figure 2B (see **Figure S3**).

In contrast to traditional impedimetric approaches to biosensor interrogation, electrochemical phase interrogation of EAB sensors produces stable baseline signals even in highly complex sample matrices. For example, we see only 0.5 to 1% baseline drift over the course of 16 h of continuous measurements directly in undiluted whole blood (**Figure 2B**). We presume that this derives from the EAB signaling mechanism, which relies on binding-induced change in the rate of electron transfer from the surface-bound redox reporter rather than adsorption of the target to a surface, thus rendering it relatively unaffected by non-specific adsorption.

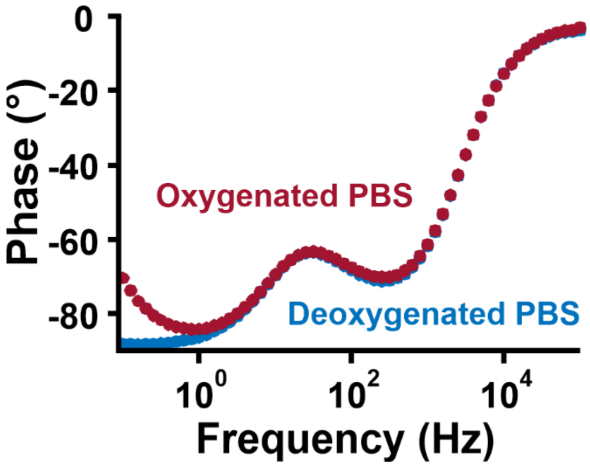

Figure 3. Electrochemical phase interrogation allows deconvolution of the contribution of other interfering electrochemical processes taking place at the EAB sensor interface, such as oxygen reduction. We show this by recording an electrochemical phase spectroscopy scan when our phosphate buffered solution is oxygenated (purple trace) and when deoxygenated by bubbling with argon gas (blue trace). In doing so, we find that low frequencies (< 1 Hz) are sensitive to the presence of oxygen and lead to an increase in phase.

Compared to voltammetric approaches, electrochemical phase interrogation minimizes the contribution of interfering surface electrochemical processes because it directly monitors the redox reporter's faradaic transfer. This includes oxygen reduction, which, upon degradation of the sensor's protecting monolayer[6], can overlap with the reduction potential of methylene blue[7], reducing measurement precision. Because transfer from the reporter is much more rapid than transfer to oxygen, electrochemical phase interrogation cleanly separates the two processes (**Figure 3**). Thus, interrogation of our EAB sensor at frequencies insensitive to the oxygen reduction (>1 Hz) can minimize any drift arising from monolayer degradation and subsequent oxygen reduction.

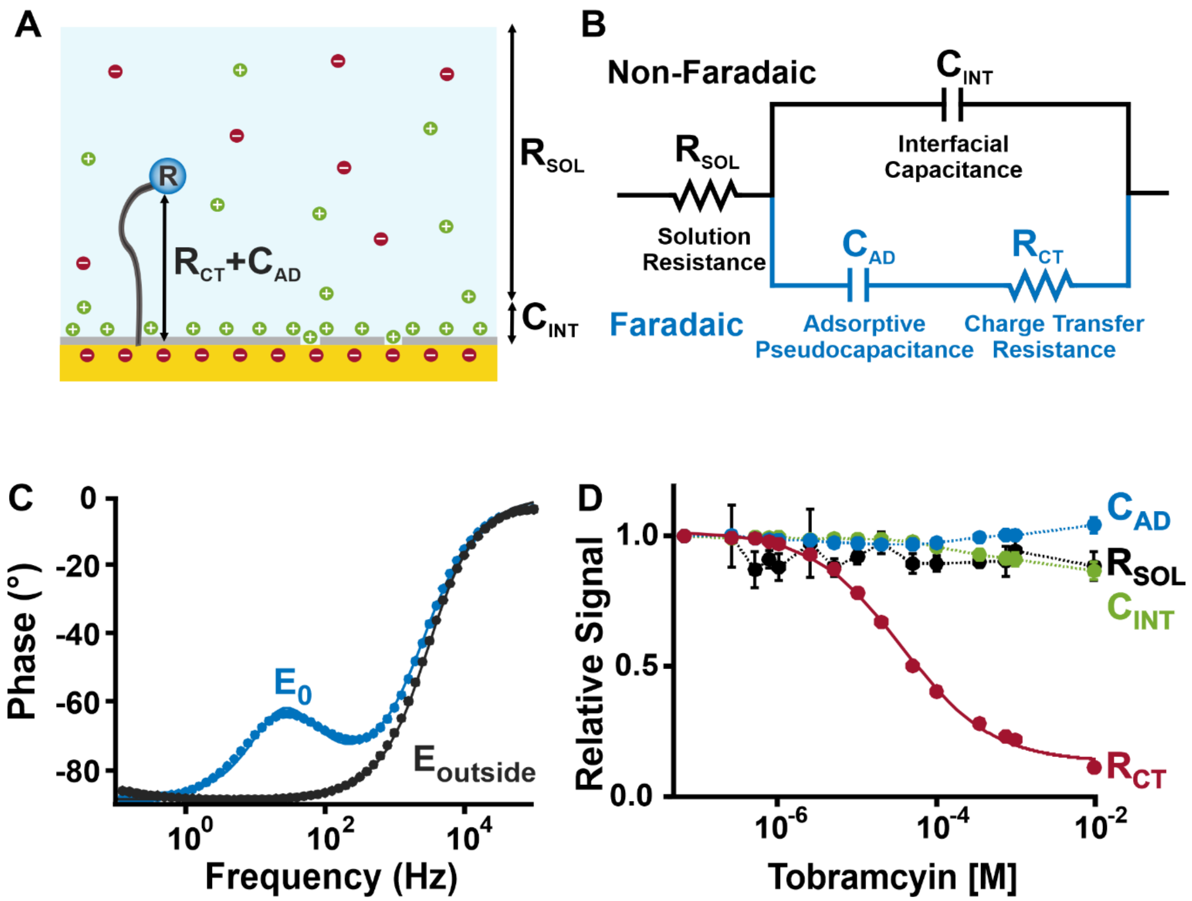

Figure 4. To better understand the signaling mechanism of EAB sensors, we model the electrochemical phase spectroscopy response as a combination of resistor and capacitor circuit elements. (**A**) We represent EAB sensors as a solution-electrode interface separated by a self-assembled alkanethiol dielectric (grey) with defects present. The electrolyte solution separating the working from the counter electrodes contributes to a resistance, R_{SOL}. The solution-electrode interface equilibrates via the formation of an electrical double layer that we represent as a non-ideal capacitor (i.e., constant phase element), C_{INT}, to capture the defects within the self-assembled monolayer. Finally, we represent the redox reporter charge transfer event by a combination of a charge transfer resistance, R_{CT}, and an adsorptive pseudocapacitance, C_{AD}, which accounts for the presence of a limited number of redox reporters on the electrode surface able to transfer electrons at a given rate[8]. (**B**) When no faradaic charge transfer occurs, our equivalent circuit simply contains the solution resistance, R_{SOL}, in series with the interfacial capacitance, C_{INT} (both in black). When faradaic charge transfer does occur, we add to our equivalent circuit the charge

transfer resistance, R_{CT}, and pseudocapacitance, C_{AD} (both in blue), in parallel with the interfacial capacitance. (**C**) We model the EAB sensor interface's impedimetric response when polarized at $E_{outside}$ (no redox reaction taking place) with the RC circuit of R_{SOL} and the interfacial capacitance, C_{INT}. We then model the EAB sensor interface when polarized at E_0 (where charge transfer occurs) with the complete equivalent circuit. We find that both our equivalent circuits fittings (solid lines) match well with our experimental results (dotted lines) ($\chi^2 = 0.033$ for $E_{outside}$, $\chi^2 = 0.021$ for E_0, fitting results in **Table S2**, **S3**). Of note, we have eliminated for these results the contribution of dissolved oxygen to the current, which appears as a shoulder at the lowest frequencies by bubbling argon gas in the electrochemical cell. (**D**) In fitting our entire equivalent circuit to the electrochemical phase spectroscopy scans of a tobramycin-binding EAB sensor exposed to an increasing amount of target in phosphate buffered saline, we find that target addition mainly affects the charge transfer resistance (R_{CT}). This is because as R_{CT} decreases, the effective resistance of the interface in accepting electrons from the reporter decreases due its increased rate of charge transfer. Fitting the resulting binding curve to a Langmuir isotherm returns a $K_D = 36$ μM (error bars represent standard deviations seen across three independently fabricated and interrogated sensors).

To understand the origins of the target-induced phase response, we modeled the EAB sensor's behavior both at the redox potential of the reporter, E_0, and at potentials far removed, $E_{outside}$, using resistors and capacitors to represent each of its components (**Figure 4A**). The phase shift in the phase spectrum approaches 0˚ at frequencies above 10 kHz (**Figure 4C**), indicating that under these conditions, the system behaves as a simple resistor of resistance R_{SOL}. This presumably occurs because these frequencies are faster than both the rate of double layer formation[9,10] and any faradaic processes[11]. At lower frequencies, formation of the electric double layer contributes capacitance to the observed behavior. For example, when the applied potential is far from the redox potential of the reporter (and thus no faradaic processes occur), the phase monotonically decreases towards -90˚ with decreasing frequency ($E_{outside}$, **Figure 4C**). To capture this effect, we include in our model a non-ideal capacitor (of capacitance C_{INT}) placed in series with the solution resistance, R_{SOL} (see black circuit elements in **Figure 4B**). The nonideality of this capacitor, reported as a constant phase element, accounts for surface monolayer defects and electrode roughness (see supporting information for additional details)[12]. Finally, when we interrogate the sensor at the reporter's redox potential, E_0, we observe a peak in the phase spectrum at frequencies corresponding to the electron transfer rate of the aptamer-attached redox reporter (**Figure 4C**)[11]. We modeled this as a resistor and a constant phase element (of resistance R_{CT} and capacitance C_{AD}, respectively) placed in series with each other and in parallel to the interfacial capacitance, C_{INT}. These elements reflect the resistance associated with faradaic charge transfer and the adsorptive pseudo-capacitance associated with oxidation and reduction of a fixed number of surface-attached, redox-reporter-modified aptamer[8,10,13,14].

By fitting our experimental data sets to the two equivalent circuit models described above, we find that the target-induced phase peak shift arises due to binding-induced changes in charge transfer resistance. To see this, we first fit data collected at $E_{outside}$ to determine R_{SOL} and C_{INT} (**Figure 4C**). Using these values, we then modeled the system's behavior at E_0 (**Figure 4C**). Both models accurately capture our experimental observations, producing estimates of R_{CT} that vary as a function of target concentration with the Langmuir isotherm shape expected for single-site binding (**Figure 4D**). In contrast, R_{SOL}, C_{INT} and C_{AD} are effectively independent of target concentration (**Figure 4D**), indicating that the phase response we observe upon target addition arises solely due to the binding-induced change in R_{CT}. This is consistent with previous arguments that signaling in this class of sensors is solely associated with binding-induced changes in the electron transfer kinetics of the redox reporter[8,15] To see this, we note that R_{CT} is inversely proportional to the electron transfer rate (**Eq. 1**) per:

$$R_{CT} = \frac{2RT}{F^2 A k_{et}} \qquad \textbf{Eq. 1}$$

where R is the ideal gas constant, T the temperature, F Faraday's constant, A the quantity of redox reporters (in moles), and k_{et} the electron transfer rate.

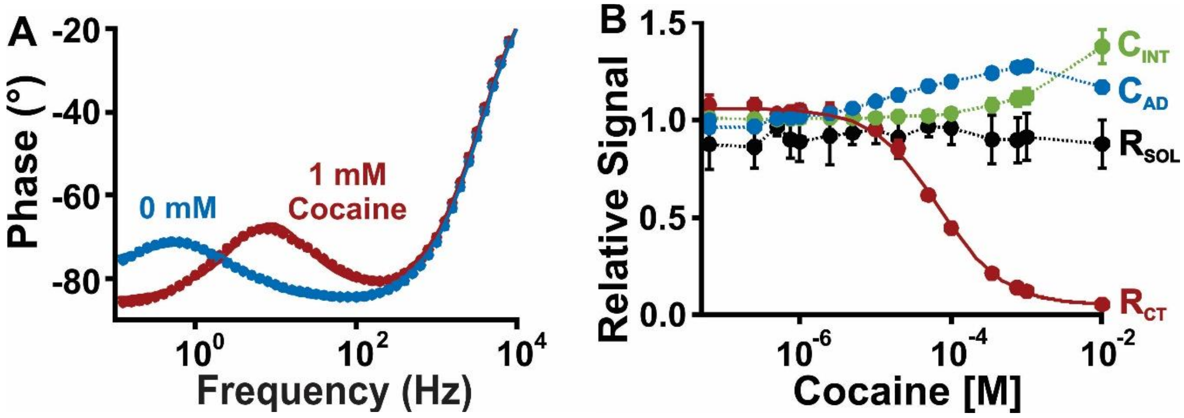

Figure 5. Electrochemical phase interrogation is applicable to other EAB sensors. **(A)** Shown, for example, is the phase response of a cocaine-detecting EAB sensor when challenged with its target (here in PBS). With target addition, we measure a phase peak shift towards higher frequencies. **(B)** Fitting the resulting phase change to our proposed equivalent circuit model in **Figure 4B** for four sensors, we find transfer resistance (R_{CT}) to be the dominant contributor to the measured phase change. This supports that, as was true for the aminoglycoside sensor, signal generation is due to a binding-induced change in electron transfer rate.

Electrochemical phase interrogation appears to be generalizable to other EAB sensors. To see this, we applied it to a sensor against the drug of abuse, cocaine, which employs a previously-described aptamer Neves et al.[16] When we interrogate this sensor at the reduction potential of the redox reporter, we observe a phase peak that shifts to higher frequencies upon the addition of increasing cocaine concentrations both in PBS (**Figure 5A**) and in undiluted whole blood (**Figure S4**). Fitting this to the equivalent circuit we used to characterize the aminoglycoside sensor, we find that the observed change in phase is, once again, largely due to changes in R_{CT} (**Figure 5C**). Signal generation in this sensor is thus also driven by binding-induced changes in electron transfer kinetics.

2.4 DISCUSSION

Electrochemical phase interrogation of EAB sensors provides a sub-second-resolved, real-time approach to measuring specific small molecules with time resolution 1 to 2 orders of magnitude better than those achieved using voltammetric interrogation of sensors in this class. Likewise, this technique rejects the confounding effects of oxygen reduction, rendering measurements less sensitive to monolayer degradation and ensuring excellent, long-duration, drift-free performance in whole blood without the need to resort to drift correction mechanisms or antifouling coatings. In short, the approach combines the speed of impedimetric measurements and selectivity of EAB sensors, thus supporting sub-second resolved measurements in complex, unprocessed clinical sample matrices.

Electrochemical phase interrogation is not the first means of collecting sub-second EAB sensor measurements,[17,18] but it does provide potential advantages over prior approaches. For example, chronoamperometry employs a series of oxidizing and reducing potentials to induce exponentially decaying current responses, which can be fitted to determine receptor occupancy with sub-second resolution[17]. In this approach, the temporal resolution is determined by the time required to fully resolve the portion of the current decay that is associated with charge transfer. A limitation of chronoamperometry, however, is the difficulty of accurately fitting exponential decays due to other decays of similar lifetimes that are unrelated to the charge transfer event (e.g., the formation of the electric double layer formation)[17]. To improve temporal resolution further, Santos-Cancel et al.[18] proposed the sampling of currents at tens of microsecond time intervals. The binding-induced signal change they observed, however, is linked to alteration in the formation of the electrical double layer, which may render the approach sensitive to non-target-driven changes at the interface (ionic strength and biofouling) that invariably occur in realistically-complex clinical samples.

Electrochemical phase interrogation combines the time resolution benefits of impedance-based measurements with the fouling resistance of surface-tethered redox reporters. This superior time resolution stems from the rapid AC potential pulses that cleanly monitor charge transfer, instead of deriving it by scanning across a large potential window (like in voltammetric approaches) or across a large frequency range (like in other impedance-based approaches). We envision that applying the phase interrogation approach to EAB sensors could resolve rapid biological events in other complex matrices or in the living body thanks to their fouling-insensitive signaling mechanism of binding-induced change in electron transfer. Beyond EAB sensors, we expect that electrochemical phase interrogation can be applied to other sensing platforms that rely on binding-induced changes in electron transfer rate. These include sensors for which signal generation is associated with binding-induced changes in (1) a surface-attached redox reporter's reorganizational energy[19-21]; (2) the coupling constant that defines how rapidly electrons transfer between an electrode and the reporter[22-24]; and (3) the diffusion of a surface-tethered redox reporter[25,26]. Thus, we believe electrochemical phase interrogation provides a widely-adaptable platform for sensing directly in complex clinical media because it combines the high time resolution of impedance-based measurements with the fouling resistance of surface-bound redox reporter sensing platforms.

2.5 EXPERIMENTAL METHODS

Aptamer preparation

We first thaw a 2 µL, aliquot of 100 µM aptamer (sequences below) pre-modified with a 6-carbon thiol linker on the 5' end and methylene blue on the 3' end (Biosearch Technologies, Novato, CA, dual HPLC purification, stored at -20^{o}C).

Aminoglycoside-binding aptamer:

5'-HO-$(CH_2)_6$-S-S-$(CH_2)_6$-GGGACTTGGTTTAGGTAATGAGTCCC-O-CH_2-CHCH$_2$OH-$(CH_2)_4$-NH-CO-$(CH_2)_2$-Methylene Blue-3'

Cocaine-binding aptamer:

5’-HO-$(CH_2)_6$-S-S-$(CH_2)_6$-AAGGAAAATCCTTCAACGAAGTGGGTC-O-CH_2-CHCH$_2$OH-$(CH_2)_4$-NH-CO-$(CH_2)_2$ -Methylene Blue-3’

Prior to conjugation, we reduce the disulfide bond by combining 2 µL of 10 mM Tris (2-carboxyethyl) phosphine (TCEP, Sigma-Aldrich, St. Louis, MO) with the aptamer sample for a one-hour thiol reduction in dark conditions at room temperature. We then dilute the sample with 96 µL 1X phosphate buffered saline and quantify the concentration of the aptamer using the molar absorption coefficient at 260 nm provided by the supplier with UV-vis spectroscopy (DU800, Beckman Coulter, Brea, CA). Using 1X phosphate buffered saline, we further dilute the aptamer sample to 500 nM.

Sensor Fabrication

We fabricate each sensor by cutting a 5 cm long, 200 mm diameter bare gold wire (Alfa Aesar, Haverhill, MA) and soldering it to a gold-plated pin connector (CH Instruments, Inc., Austin, TX) with 60/40 lead-selenium solder (Digikey, Thief River Falls, MN) without any polishing done. To isolate the working electrode surface, we insulate the bare gold wire with two layers of polytetrafluorethylene (PTFE) heat-shrink tubing (HS Sub-Lite-Wall PTFE, ZEUS, Orangeburg, SC) using an industrial hot air blower (Master Appliance Corp., Racine, WI), leaving approximately 3.5 mm of bare gold surface exposed. We then trim the exposed working electrode surface to 3 mm.

Next, we cleaned the electrode surface to prepare it for modification with the aptamer. For all cleaning procedures and experiments, our electrochemical cell consists of an PTFE-wrapped gold sensor working electrode, a platinum counter electrode (CH Instruments, Inc, Austin, TX), and an Ag|AgCl reference electrode (CH Instruments, Inc., Austin TX). We secure our working, counter, and reference electrodes in a “shot glass” cell vessel with a custom-fabricated Teflon lid fixture. First, we electrochemically clean the electrodes in 0.5 M NaOH (Sigma-Aldrich, St. Louis, MO) by performing repeated cyclic voltammetry scans between -1 to -1.6 V vs. Ag|AgCl at 1 V s^{-1} scan rate for 300 cycles using a CH Multipotentiostat (CHI1040C, CH Instruments, Inc.) to remove any contaminating organics (**Table S1** for complete parameters), followed by a thorough rinsing in deionized water. Then, we increase the surface area of the gold wire electrode by electrochemically roughening in 0.5 M H_2SO_4 (Sigma-Aldrich, St. Louis, MO) using a previously-described procedure[27] that involves repeatedly stepping the potential between 0 and 2.2 V (see **Table S1** for parameter details). This results in a 2 to 5-fold increase in microscopic surface area, attributed to islands of nano-scale dendrites forming on the planar gold surface[27]. Immediately after roughening, we rinse the electrodes thoroughly in deionized water and place them in the prepared aptamer solution for 1 h at room temperature in dark conditions. To passivate the surface, we rinse the electrode with deionized water and immerse them for 10 to 12 h at 4˚C in a 10 mM 6-mercapto-1-hexanol (Sigma-Aldrich, St. Louis, MO) solution suspended in 1X phosphate buffered saline (PBS). Following a final rinse with deionized water, the sensor is ready for use.

Data Collection

We perform electrochemical impedance spectroscopy characterization experiments on a Gamry Reference 600+ potentiostat/galvanostat (Gamry Instruments, Warminster, PA). First, we characterize the modified electrodes at room temperature in 1X PBS. To determine the formal potential, E_0, of the redox reporter, we collect a cyclic voltammogram, sweeping from -0.1 V to -0.45 V at 100 mV s^{-1}, and identify the midpoint between the oxidation and reduction waves of the voltammogram. We then collect a potentiostatic impedimetric measurement by applying an AC potential waveform of 10 mV amplitude centered around the formal potential, measuring the impedance response from 10 kHz to 0.1 Hz. To measure the response to target addition, we collect phase between 10 kHz to 0.1 Hz after adding graduated amounts of stock concentrations of tobramycin sulfate (USP Grade, Gold BioTechnology Inc., St Louis, MO) in 1X PBS. To evaluate the sensor's performance in complex matrices, we also repeated this binding curve experiment in undiluted, heparinized whole bovine blood (Hemostat Laboratories, Dixon, CA).

2.6 ACKNOWLEDGEMENTS

We acknowledge Kaylyn Leung and Nathan Ogden for useful discussions relating to impedance spectroscopy and modeling of electrochemical interfaces. Further, we acknowledge Kaylyn Leung for useful critical feedback of our manuscript. The project described was supported by the Office of Naval Research through grant number N00014-20-1-2164. This material is based upon work supported by the National Science Foundation Graduate Research Fellowship under Grant No. 1650114 (A.D.). The content of the information does not necessarily reflect the

position or the policy of the Government, and no official endorsement should be inferred.

2.7 SUPPLEMENTAL INFORMATION

Table S1. Electrochemical cleaning and roughening parameters for microscopic surface area enhancement. We perform cleaning procedures with a CHI1040C potentiostat (CH Instruments, Inc.)

	Electrode Cleaning in 0.5 M NaOH	**Electrode Roughening In 0.5 M H_2SO_4**
Electrochemical Technique	Cyclic Voltammetry	Chronoamperometry
$E_{initial}$ (V) vs. Ag|AgCl	-1.0	0.0
E_{high} (V) vs. Ag|AgCl	-1.0	2.2
E_{low} (V) vs. Ag|AgCl	-1.6	0.0
Scan Rate (V s^{-1})	1.0	N/A
Number of Repeats	300	32,000
Interval (V)	0.001	N/A
Quiet Time (s)	0	0
Sensitivity	1e-4	1e-3
Pulse Width (s)	N/A	0.02

2.7a. Circuit Fitting: Constant Phase Element

The constant phase element impedance follows:

$$Z_{CPE} = \frac{1}{C\,(j\omega)^n} \qquad \textbf{Eq. S1}$$

where *C* represents capacitance, ω represents radial frequency, *j* represents a unit imaginary number, and *n* represents the degree to which the system behaves as an ideal capacitor, with 1 indicating pure capacitance ($0 < n < 1$). To improve model convergence, we constrained R_{SOL} within 100-150 Ω, a range determined from data collected at frequencies > 10^4 Hz, where resistance dominates the impedimetric response (**Figure S1**).

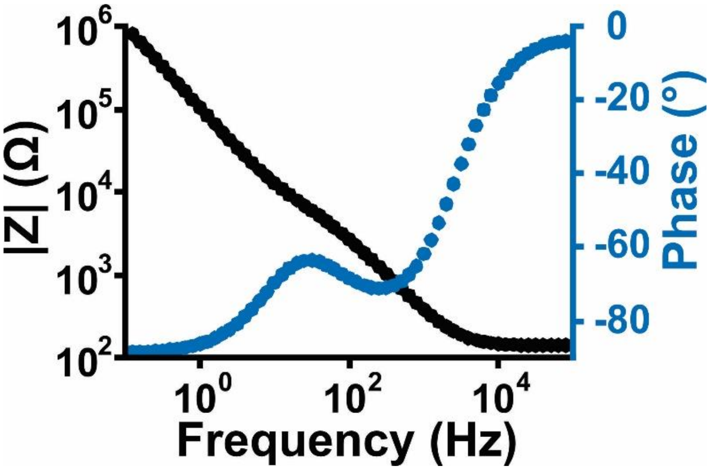

Figure S1. A Bode plot representation of data collected at E_0 in deoxygenated 1X PBS. At frequencies greater than 10^4 Hz, the impedance (which, at these frequencies, is dominated by solution resistance) equals approximately 145 Ω.

2.7b Circuit Fitting Results

Using the least squares analysis fitting tool in Nova 2.1 software yields the following parameter estimates for the above-described circuit:

Table S2. Output parameters for fitting a circuit consisting of a resistor in series with a constant phase element capacitor to data collected when we interrogate the E-AB sensor at a potential far away from the redox active region ($E_{outside}$, see **Figure 4C**).

Circuit Element	**Value**	**Error (%)**
R_{SOL} (Ω)	137.74	0.489
C_{INT} (s^n/ Ω)	4.45×10^{-7}	0.483
n	0.985	0.085
χ^2	0.020827	N/A

Note: we include units of the constant phase elements as (s^n/ Ω), where s represents seconds, and n represents the degree to which the system behaves as an ideal capacitor, with 1 indicating pure capacitance (**Eq. S1**).

Table S3. Output parameters for fitting a circuit consisting of solution resistor in series with two parallel paths: a constant phase element capacitor representing interfacial capacitance, C_{INT}, and a branch with a charge transfer resistance, R_{CT}, and constant phase element capacitor representing pseudocapacitance, C_{AD}. We use this circuit to model the E-AB sensor interface when we polarize the electrode at the formal potential, E_0 (see **Figure 4C**).

Circuit Element	**Value**	**Error (%)**
R_{SOL} (Ω)	138	0.691
C_{INT} (s^n/ Ω)	8.67×10^{-7}	3.763
n (for C_{INT})	0.93015	0.487
C_{AD} (s^n/ Ω)	7.18×10^{-7}	4.701
n (for C_{AD})	1.0178	0.862

R_{CT} (Ω)	12,963	4.638
χ^2	0.032646	N/A

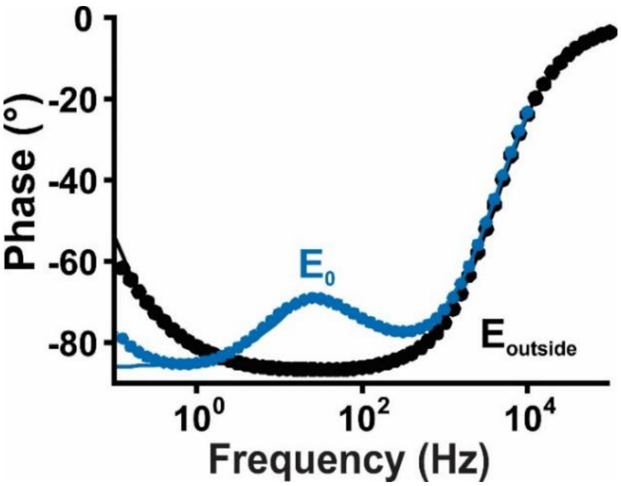

Figure S2: We modeled the EAB sensor impedimetric response in 1X PBS when polarized at $E_{outside}$ (i.e., where no redox reaction takes place) with the RC circuit of R_{SOL} and the interfacial capacitance, C_{INT}. We then model the sensor when polarized at E_0 (where charge transfer occurs) with the complete equivalent circuit. We find that both equivalent circuits fittings (solid lines) match well with our experimental results (dots) (χ^2 = 0.075984 for $E_{outside}$, χ^2 = 0.025993 for E_0).

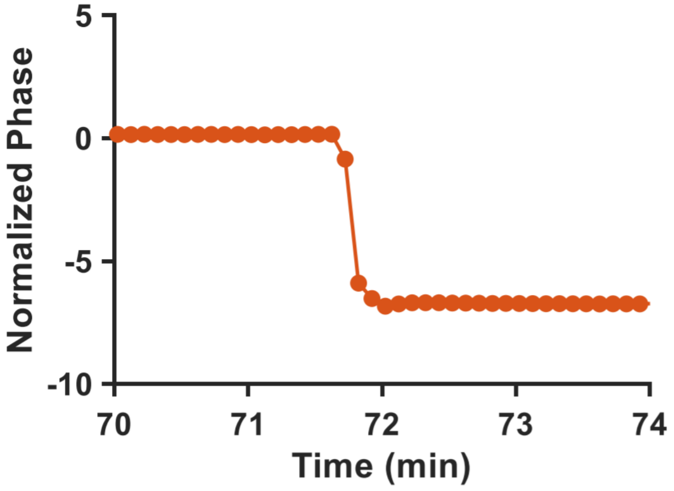

Figure S3: When E-AB sensors are immersed in an electrochemical cell with undiluted whole blood spiked with 300 µM of tobramycin which is homogenized rapidly for ~20 s, the sensor rapidly responds to target. Shown here is the normalized % phase versus time.

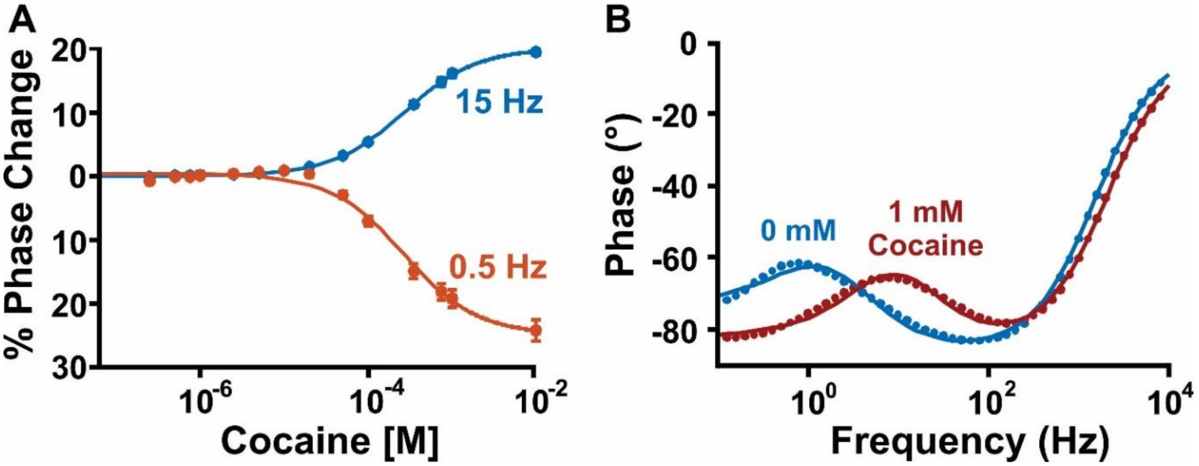

Figure S4: Electrochemical phase interrogation is applicable to other EAB sensors, such as (shown here) a cocaine-detecting aptamer. **(A)** When performing alternating electrochemical phase measurements at 0.5 and 15 Hz (orange and blue traces) in PBS, we observe binding curves that reach phase changes of ~20% at saturating target. The error bars indicate standard error derived from 4 independently fabricated and interrogated sensors. **(B)** The phase response also occurs in undiluted whole blood. With target addition, we measure a phase peak shift towards higher frequencies.

2.8 REFERENCES

(1) White, R. J.; Plaxco, K. W. Exploiting Binding-Induced Changes in Probe Flexibility for the Optimization of Electrochemical Biosensors. *Analytical Chemistry* **2010**, *82*, 73-76, 10.1021/ac902595f.
(2) Dauphin-Ducharme, P.; Arroyo-Currás, N.; Kurnik, M.; Ortega, G.; Li, H.; Plaxco, K. W. Simulation-Based Approach to Determining Electron Transfer Rates Using Square-Wave Voltammetry. *Langmuir* **2017**, *33*, 4407-4413, 10.1021/acs.langmuir.7b00359.
(3) Daniels, J. S.; Pourmand, N. Label-Free Impedance Biosensors: Opportunities and Challenges. *Electroanalysis* **2007**, *19*, 1239-1257, 10.1002/elan.200603855.

(4) Bogomolova, A.; Komarova, E.; Reber, K.; Gerasimov, T.; Yavuz, O.; Bhatt, S.; Aldissi, M. Challenges of Electrochemical Impedance Spectroscopy in Protein Biosensing. *Analytical Chemistry* **2009**, *81*, 3944-3949, 10.1021/ac9002358.
(5) Rowe, A. A.; Miller, E. A.; Plaxco, K. W. Reagentless measurement of aminoglycoside antibiotics in blood serum via an electrochemical, ribonucleic acid aptamer-based biosensor. *Analytical chemistry* **2010**, *82*, 7090-7095, 10.1021/ac101491d.
(6) Shaver, A.; Curtis, S. D.; Arroyo-Currás, N. Alkanethiol Monolayer End Groups Affect the Long-Term Operational Stability and Signaling of Electrochemical, Aptamer-Based Sensors in Biological Fluids. *ACS Applied Materials & Interfaces* **2020**, *12*, 11214-11223, 10.1021/acsami.9b22385.
(7) Kang, D.; Ricci, F.; White, R. J.; Plaxco, K. W. Survey of Redox-Active Moieties for Application in Multiplexed Electrochemical Biosensors. *Analytical Chemistry* **2016**, *88*, 10452-10458, 10.1021/acs.analchem.6b02376.
(8) Creager, S. E.; Wooster, T. T. A New Way of Using ac Voltammetry To Study Redox Kinetics in Electroactive Monolayers. *Analytical Chemistry* **1998**, *70*, 4257-4263, 10.1021/ac980482l.
(9) Bertok, T.; Lorencova, L.; Chocholova, E.; Jane, E.; Vikartovska, A.; Kasak, P.; Tkac, J. Electrochemical Impedance Spectroscopy Based Biosensors: Mechanistic Principles, Analytical Examples and Challenges towards Commercialization for Assays of Protein Cancer Biomarkers. *ChemElectroChem* **2019**, *6*, 989-1003, 10.1002/celc.201800848.
(10) Eckermann, A. L.; Feld, D. J.; Shaw, J. A.; Meade, T. J. Electrochemistry of redox-active self-assembled monolayers. *Coordination Chemistry Reviews* **2010**, *254*, 1769-1802, 10.1016/j.ccr.2009.12.023.
(11) Dauphin-Ducharme, P.; Arroyo-Currás, N.; Adhikari, R.; Somerson, J.; Ortega, G.; Makarov, D. E.; Plaxco, K. W. Chain Dynamics Limit Electron Transfer from Electrode-Bound, Single-Stranded Oligonucleotides. *The Journal of Physical Chemistry C* **2018**, *122*, 21441-21448, 10.1021/acs.jpcc.8b06111.
(12) Douglass Jr, E. F.; Driscoll, P. F.; Liu, D.; Burnham, N. A.; Lambert, C. R.; McGimpsey, W. G. Effect of Electrode Roughness On the Capacitive Behavior of Self-Assembled Monolayers. *Analytical Chemistry* **2008**, *80*, 7670-7677, 10.1021/ac800521z.
(13) Zoltowski, P. On the electrical capacitance of interfaces exhibiting constant phase element behaviour. *Journal of Electroanalytical Chemistry* **1998**, *443*, 149-154, 10.1016/S0022-0728(97)00490-7.
(14) Ahmad, S. A. A.; Ciampi, S.; Parker, S. G.; Gonçales, V. R.; Gooding, J. J. Forming Ferrocenyl Self-Assembled Monolayers on Si(100) Electrodes with Different Alkyl Chain Lengths for Electron Transfer Studies. *ChemElectroChem* **2019**, *6*, 211-220, 10.1002/celc.201800717.
(15) Dauphin-Ducharme, P.; Plaxco, K. W. Maximizing the Signal Gain of Electrochemical-DNA Sensors. *Analytical Chemistry* **2016**, *88*, 11654-11662, 10.1021/acs.analchem.6b03227.
(16) Neves, M. A. D.; Reinstein, O.; Saad, M.; Johnson, P. E. Defining the secondary structural requirements of a cocaine-binding aptamer by a

thermodynamic and mutation study. *Biophysical Chemistry* **2010**, *153*, 9-16, 10.1016/j.bpc.2010.09.009.
(17) Arroyo-Currás, N.; Dauphin-Ducharme, P.; Ortega, G.; Ploense, K. L.; Kippin, T. E.; Plaxco, K. W. Subsecond-Resolved Molecular Measurements in the Living Body Using Chronoamperometrically Interrogated Aptamer-Based Sensors. *ACS Sensors* **2018**, *3*, 360-366, 10.1021/acssensors.7b00787.
(18) Santos-Cancel, M.; Lazenby, R. A.; White, R. J. Rapid Two-Millisecond Interrogation of Electrochemical, Aptamer-Based Sensor Response Using Intermittent Pulse Amperometry. *ACS Sensors* **2018**, *3*, 1203-1209, 10.1021/acssensors.8b00278.
(19) Plumb, K.; Kraatz, H.-B. Interaction of a Ferrocenoyl-Modified Peptide with Papain: Toward Protein-Sensitive Electrochemical Probes. *Bioconjugate Chemistry* **2003**, *14*, 601-606, 10.1021/bc0256446.
(20) Orlowski, G. A.; Chowdhury, S.; Kraatz, H.-B. Reorganization Energies of Ferrocene-Peptide Monolayers. *Langmuir* **2007**, *23*, 12765-12770, 10.1021/la701740q.
(21) Feld, D. J.; Hsu, H.-T.; Eckermann, A. L.; Meade, T. J. Trinuclear Ruthenium Clusters as Bivalent Electrochemical Probes for Ligand–Receptor Binding Interactions. *Langmuir* **2012**, *28*, 939-949, 10.1021/la202882k.
(22) Uzawa, T.; Cheng, R. R.; White, R. J.; Makarov, D. E.; Plaxco, K. W. A Mechanistic Study of Electron Transfer from the Distal Termini of Electrode-Bound, Single-Stranded DNAs. *Journal of the American Chemical Society* **2010**, *132*, 16120-16126, 10.1021/ja106345d.
(23) Genereux, J. C.; Barton, J. K. Mechanisms for DNA Charge Transport. *Chemical Reviews* **2010**, *110*, 1642-1662, 10.1021/cr900228f.
(24) Boon, E. M.; Ceres, D. M.; Drummond, T. G.; Hill, M. G.; Barton, J. K. Mutation detection by electrocatalysis at DNA-modified electrodes. *Nature Biotechnology* **2000**, *18*, 1096-1100, 10.1038/80301.
(25) Katayama, Y.; Ohuchi, Y.; Higashi, H.; Kudo, Y.; Maeda, M. The Design of Cyclic AMP−Recognizing Oligopeptides and Evaluation of Its Capability for Cyclic AMP Recognition Using an Electrochemical System. *Analytical Chemistry* **2000**, *72*, 4671-4674, 10.1021/ac990847h.
(26) Le Floch, F.; Ho, H. A.; Leclerc, M. Label-Free Electrochemical Detection of Protein Based on a Ferrocene-Bearing Cationic Polythiophene and Aptamer. *Analytical Chemistry* **2006**, *78*, 4727-4731, 10.1021/ac0521955.
(27) Arroyo-Currás, N.; Somerson, J.; Vieira, P. A.; Ploense, K. L.; Kippin, T. E.; Plaxco, K. W. Real-time measurement of small molecules directly in awake, ambulatory animals. **2017**, *114*, 645-650, 10.1073/pnas.1613458114 %J Proceedings of the National Academy of Sciences.

CHAPTER 3: NANOPOROUS GOLD FOR THE MINIATURIZATION OF IN VIVO ELECTROCHEMICAL APTAMER-BASED SENSORS

3.1 ABSTRACT

Electrochemical aptamer-based sensors enable real-time molecular measurements in the living body. The spatial resolution of these measurements and ability to perform measurements in targeted locations, however, is limited by the length and width of the device's working electrode. Historically, achieving good signal-to-noise in the complex, noisy in vivo environment has required working electrode lengths of 3 to 6 mm. To enable sensor miniaturization, here we have enhanced the signaling current obtained for a sensor of given macroscopic dimensions by increasing its surface area. Specifically, we produced nanoporous gold via an electrochemical alloying/dealloying technique to increase the microscopic surface area of our working electrodes by up to 100-fold. Using this approach, we have miniaturized the in vivo EAB sensors (here using sensors against the antibiotic, vancomycin) by a factor of 6 while retaining sensor signal and response times. Conveniently, the fabrication of nanoporous gold is simple, parallelizable, and compatible with both two- and three-dimensional electrode architecture, suggesting it may be of value to a range of electrochemical biosensor applications.

3.2 INTRODUCTION

Achieving good signal-to-noise with EAB sensors in the complex in vivo environment has historically required 75 µm to 200 µm diameter gold wires with lengths of 3 to 6 mm (refs[1-6]). While such sensors are small relative to the length scale of human tissue dimensions, they are inconveniently large for some applications. The several millimeter lengths of the sensors in prior use limits our ability to make targeted measurements in specific rat brain regions. Further, intravenous deployment of EAB sensors in mice, an animal model of great interest for pharmaceutical screening, would require narrower sensors. Thus motivated, we explore here a new approach to further miniaturizing in vivo EAB sensors.

Increasing the microscopic surface area of the gold provides a route towards smaller EAB sensors because it allows the attachment of more aptamers to an electrode of a given size. To this end, many techniques exist that enhance the microscopic surface area of gold, including a number of electrochemical etching/deposition approaches[7-14], co-sputtering[15-17], or the leaching of commercially-available gold alloy foils[15,18,19]. Co-sputtering and the leaching of gold foil, however, are incompatible with the wire format of our implantable sensors. In contrast, electrochemical surface area enhancement techniques are readily compatible with our sensor architecture. Indeed, our prior in vivo EAB studies relied on electrochemical roughening in acid to produce dendritic structures. However, this technique achieves only 2- to 4-fold enhancements[6]. Here, we have implemented an electrochemical alloying and dealloying process that achieves up to a 100-fold increase in surface area, enabling significant reductions in EAB sensor size.

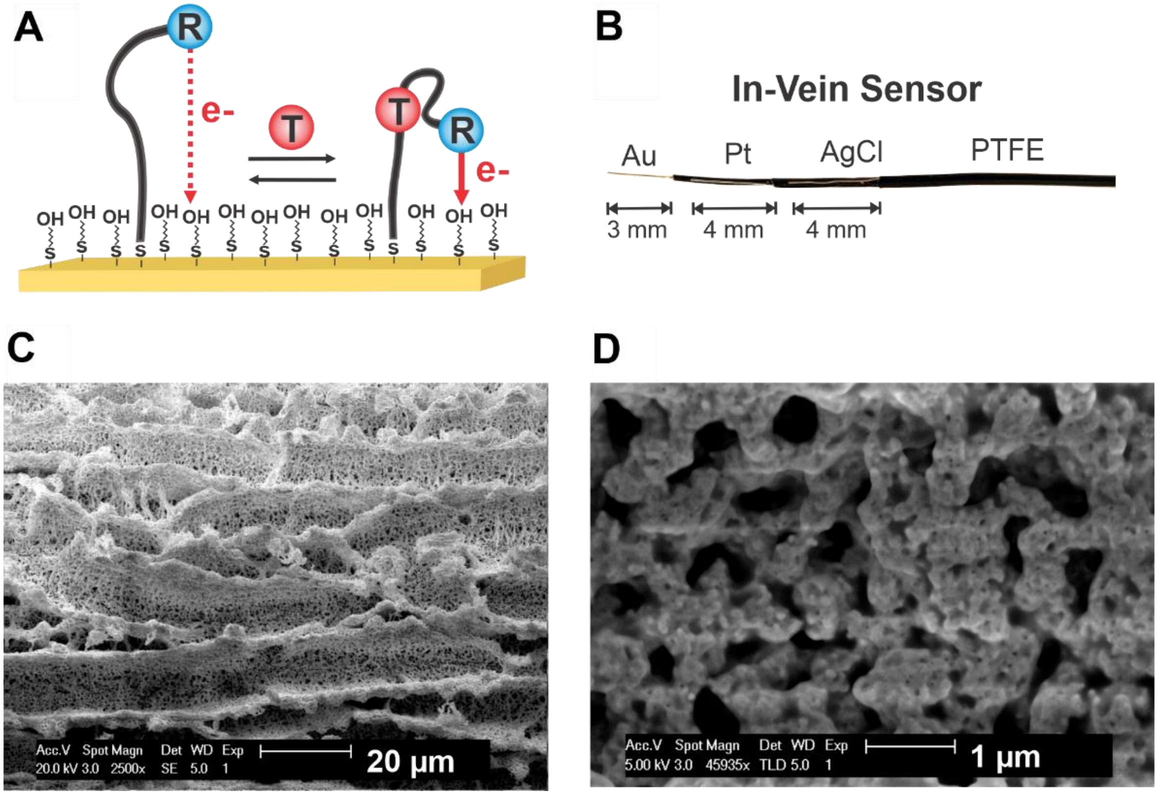

Figure 1: **(A)** To fabricate an EAB sensor, we form a self-assembled monolayer consisting of redox reporter-modified (R) aptamer and 6-mercapto-1-hexanol on the surface of a gold electrode. EAB signaling occurs via a target (T) binding-induced change in the electron transfer kinetics of the redox reporter. Graphic reprinted with permission[20]. **(B)** Our intravenous EAB sensors consist of bundled gold, platinum, and silver wires. In past work, in vivo measurements have required gold working electrodes measuring 3 to 6 mm in length and 75 µm to 200 µm in diameter. **(C)** To further miniaturize EAB sensors, here we have fabricated them using nanoporous gold electrodes. As shown by scanning electron microscopy at 2500x magnification, layers of sponge-like pores cover the surface of these electrodes, greatly increasing their microscopic surface area. **(D)** As shown by scanning electron microscopy at 45,935x magnification, the matrix pore sizes range from 30 to 500 nm.

3.3 RESULTS AND DISCUSSION

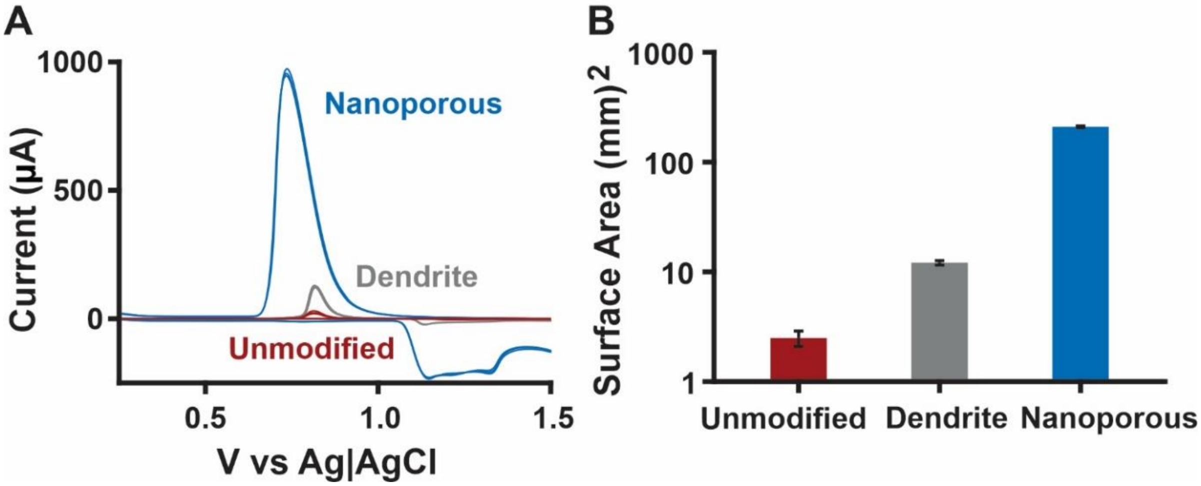

Figure 2: The generation of nanoporous gold greatly increases the microscopic surface area of gold wire electrodes. To see this, we used cyclic voltammetry to compare the microscopic surface areas of three wire substrates: an unmodified gold wire, a dendrite-covered wire prepared using our prior electrochemical roughening procedure[6], and a nanoporous gold wire of the type explored here. Each wire has an exposed working electrode surface 3 mm long by 200 μm in diameter. **(A)** Comparing the areas under CV curves collected in 50 mM sulfuric acid (which reflects the reduction of the gold oxide surface layer[21], which, in turn, is proportional to microscopic surface area[6,22]) of the three surface morphologies, we see that the microscopic surface area of the nanoporous substrate is greatly enhanced. Of note, this figure shows data collected from 3 electrodes for each morphology; the lines overlap well, illustrating the reproducibility of our fabrication procedures. **(B)** The integrated area under the reduction peak in the CV curves shown in the prior panel indicate that the surface area of this batch of nanoporous gold electrodes is approximately 85-fold greater than that of unmodified gold and 20-fold greater than that of the dendritic gold. The error bars here and elsewhere in this manuscript reflect standard deviations of the mean.

Because it can increase the microscopic surface area of gold wires up to 100-fold, we have applied an electrochemical alloying procedure which creates a nanoporous gold layer on the surface[23]. In this technique, we apply cyclic voltammetry to alternatively deposit and strip away zinc metal (**Figure S1**). The cathodic potential sweep deposits zinc onto the gold surface – forming a layer of zing and gold-zinc alloy[24]. The anodic sweep then removes zinc from the surface, leaving behind a pitted gold surface[24,25]. Repeating this process produces a gold layer riven with nano- to micro-scale pores (**Figure 1C**), the smallest of which range from 30 to 500 nm in diameter (**Figure 1D**). The nanoporous gold fabrication technique produces significantly greater microscopic surface area than either unmodified wire substrates or wires modified using the electrochemical roughening procedure[6] we have employed previously to produce dendrite morphologies (**Figure 2A**). Specifically, the alloying/dealloying technique that produces nanoporous gold achieves surface area enhancements of 75- to 100-fold relative to those seen for unmodified electrodes, and 15 to 20-fold relative to dendrite electrodes (**Figure 2B**). The degree of surface area enhancement within a given alloying/dealloying batch is quite reproducible, as indicated by the near perfect overlap of cyclic voltammograms collected in sulfuric acid (**Figure 2A**).

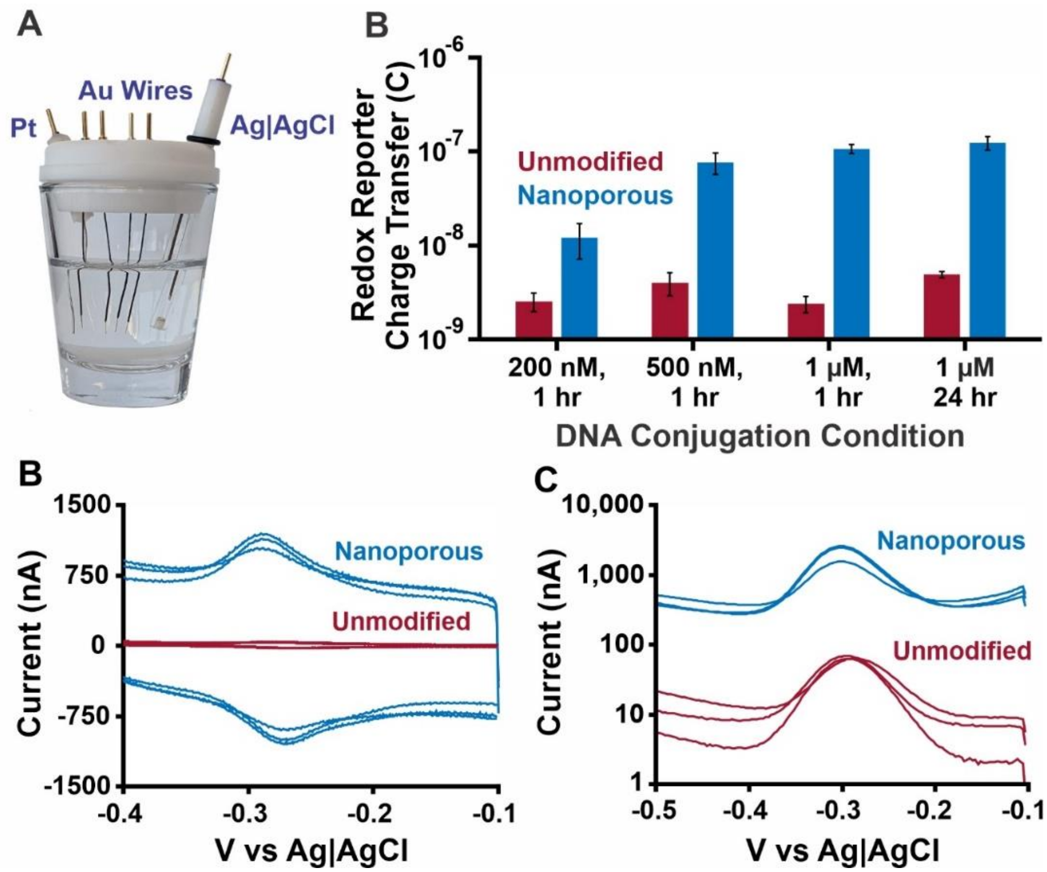

Figure 3: Irrespective of the aptamer deposition conditions, nanoporous substrates produce higher EAB sensor signals than unmodified substrates of the same macroscopic dimensions. **(A)** We interrogate EAB sensors in PBS within a glass vessel and PTFE cap securing the gold wire working electrodes, platinum counter electrode, and Ag|AgCl reference electrode. (**B**) Charge transfer from the redox reporter (a measure of the number of methylene-blue-modified aptamers on the surface) is higher for the nanoporous electrode at all aptamer deposition concentrations or deposition durations. Here, we incubated independently-prepared electrodes with the thiol-modified aptamer at 200 nM, 500 nM, or 1 µM of for 1 h, and at 1 µM for 24 h (n = 3 electrodes each). Because the increase in charge transfer plateaus at a 1 h long, 1 µM DNA deposition, we select these as our deposition conditions. **(C)** The increase in redox signal produced by nanoporous electrodes is evident here in cyclic voltammograms. For the same macroscopic dimensions (3 mm long x 200 mm diameter, n = 3 each), the methylene blue redox peak area is 25-fold greater for nanoporous electrodes. **(D)** Reflecting this, the square wave voltammetry

peaks of sensors fabricated on nanoporous electrodes also increase significantly. At a square wave frequency of 10 Hz, for example, the nanoporous wires exhibit approximately 30-fold greater peak currents (note that the y-axis on this plot is logarithmic).

The nanoporous gold electrodes' higher surface area increases EAB sensor signal. As our test-bed demonstration of this, we prepared sensors that detect the antibiotic, vancomycin, which we fabricated using a range of aptamer deposition concentrations and times (**Figure 3B**). The sensors we fabricated using nanoporous electrodes produced consistently greater signaling current under all of the deposition conditions we investigated. Because the observed signal improvement for nanoporous wires plateaus at a 1 h incubation in 1 µM aptamer (**Figure 3B**), we selected these parameters as our fabrication conditions moving forward. Compared to unmodified substrates, EAB sensors constructed on nanoporous electrodes exhibit higher signaling current from the aptamers' methylene blue redox reporter. For example, comparing cyclic voltammograms collected in phosphate buffered saline, we see an approximately 25-fold increase in the methylene blue reduction peak for sensors fabricated using nanoporous electrodes (**Figure 3C**). We see similar signal enhancements when we compare square wave voltammetry peak currents (30-fold at 10 Hz), which, due to its sensitivity and reduction of charging current contributions, is the most ubiquitous approach for interrogating EAB sensors (**Figure 3D**).

The increase in EAB signal we observe is smaller than the 75-100-fold increase in microscopic surface area seen for nanoporous electrodes (**Figure 2**). This discrepancy, which is consistent with recent observations by Vesilinovic et al., who examined the impact of nanoporous gold surfaces on the signaling of a different class of electrochemical biosensors[16], may result from two sources. First, hindered diffusion of aptamer into the smallest pores in the matrix might reduce the number of aptamers per unit of microscopic surface area. Consistent with this, the aptamer packing density on nanoporous gold is lower than that seen on unmodified gold. Fortunately, however, while lower aptamer packing density often is associated with increased EAB sensor degradation[26], sensors fabricated on both nanoporous and unmodified substrates drift at similar rates (**Figure S3**). Second, charging currents can reduce square wave voltammogram peak height due to the greater capacitance associated with higher surface areas. Because charging currents increase with interrogation frequency[27], baselines can impact peak signals at higher frequencies (**Figure S4**). Thus, effectively using high surface area substrates with EAB sensors (and other electrochemical sensors) requires careful selection of interrogation frequency. Fortunately, however, the impact of capacitance on peak baselines is reduced when using smaller electrodes.

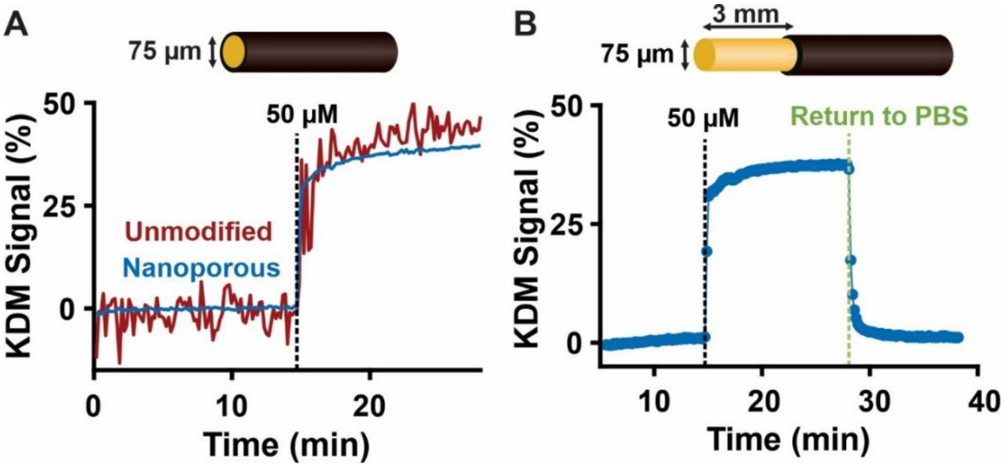

Figure 4: (A) Cutting insulated wires to expose a single circular surface, we produced 75 µm diameter “micro-disk” electrodes fabricated from unmodified gold and nanoporous gold. Both micro-disk electrodes respond immediately to the addition of

50 µM target in PBS. The sensor fabricated using nanoporous gold, however, yields a significantly improved signal-to-noise ratio. (**B**) The complex surface of the nanoporous gold does not significantly slow the equilibration of EAB sensors fabricated using this material. Shown here, for example, is the rapid response of a 3 mm long, 75 µm diameter nanoporous gold sensor when challenged in PBS with 50 µM vancomycin, followed by a return to baseline upon returning to target-free PBS.

The enhanced signaling current provided by nanoporous electrodes enables significant EAB sensor miniaturization. To illustrate this, we first reduced the macroscopic surface area of a sensor by approximately 160-fold by fabricating it on an electrode produced by cutting an insulated gold wire to expose a 75 µm diameter disk. The resulting "microdisk" sensor produces easily measurable signal and target response in both its unmodified and nanoporous configurations (**Figure 4A**). The microdisk sensor fabricated using nanoporous gold, however, exhibited significantly reduced noise. For example, the 0.4% baseline noise (defined here as the relative standard deviation of the fluctuating signal seen in the absence of target) seen for the nanoporous gold is more than 9 times lower than that seen for the equivalent unmodified gold electrode. This improvement is so great that noise seen in vitro for a 75 µm nanoporous disk electrode is comparable to that seen for a 75 µm diameter, 3 mm long sensor fabricated on unmodified gold interrogated under the same conditions (**Figure 4B)**.

Previous studies of nanoporous substrates have found that their complex morphology can slow the diffusion of materials to the electrode surface, in turn slowing sensor response or reducing its magnitude[28-30]. Fortunately, however, we have not found this causes a significant limitation for detecting small molecule targets, such as vancomycin. For example, when we exposed a sensor fabricated on nanoporous gold to 50 µM vancomycin in PBS, the sensor reached 90% of its final signaling current within 1 min (**Figure 4B).** Returning the sensor to target-free PBS, the signal returned to within 10% of baseline in ~ 2.5 min. In contrast, EAB sensor equilibration time does increase for higher molecular weight targets. Specifically, when challenging an EAB sensor[3] that responds to the 25 kDa protein, NGal, we observe 90% of signal saturation within ~1 min and ~5 min for sensors fabricated on unmodified and nanoporous gold, respectively (**Figure S5**).

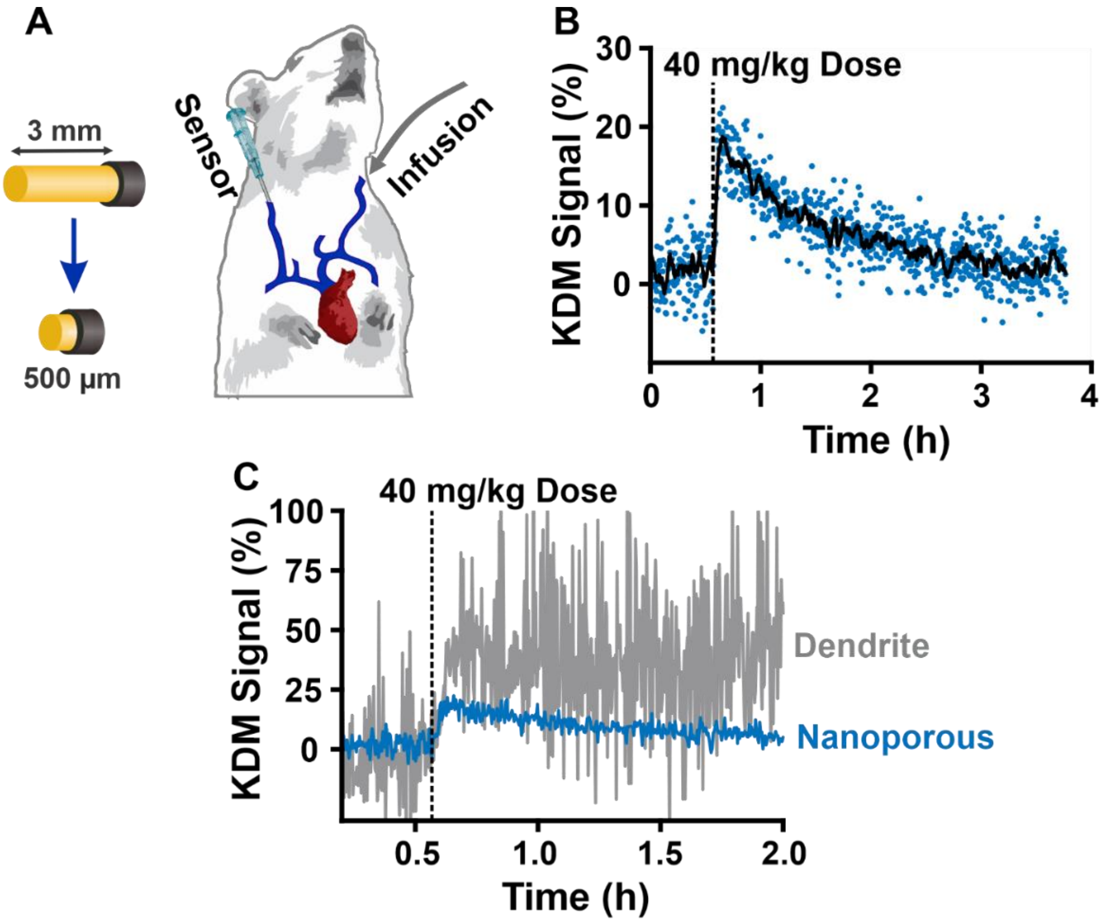

Figure 5: The use of nanoporous electrodes supports the miniaturization of in vivo EAB sensors. **(A)** Here, using a catheter, we place a miniaturized EAB sensor in the right jugular vein of an anesthetized rat, and infuse vancomycin via the left jugular vein. **(B)** Shown here are in-vein measurements collected using a 75 µm diameter,

500 µm long vancomycin sensor fabricated on a nanoporous electrode. After collecting a 15 min baseline, we perform a 40 mg/kg IV injection of the drug. The resulting raw KDM signal (blue) and a 10-point rolling average (black) are shown. As expected, the sensor responds immediately to the vancomycin addition and then returns to baseline (zero) levels as the drug is cleared from the bloodstream over the course of a few hours. Using a calibration curve collected in undiluted bovine blood (**Figure S6**), we estimate the peak concentration in the jugular vein to equal 8 µM (**Figure S7**) **(C)** We compare the raw KDM signal shown in the first panel with signal collected using a dendrite-modified vancomycin sensor of the same macroscopic dimensions. In contrast to the nanoporous substrate (blue), the signal-to-noise of the dendrite-modified sensor (grey) is too poor to support measurements of drug delivery and clearance.

The improved signaling seen for sensors employing nanoporous gold electrodes supports experimentally significant reductions in the size of indwelling EAB sensors. For example, despite being six times smaller than our previously reported in vivo sensors, a 500 µm long, 75 µm diameter vancomycin-detecting EAB sensor fabricated on nanoporous gold still produces good baseline signal-to-noise (baseline standard deviation = 2%) when placed into the jugular of a live rat (**Figure 5A**)[1,2,5]. In contrast, the signal associated with a sensor of the same size fabricated on a dendritic electrode was too poor to clearly resolve drug delivery and clearance (**Figure 5B**).

3.4 CONCLUSION

The electrochemical alloying/dealloying procedure applied here significantly improves surface area, enabling reductions in sensor size while maintaining effective performance. For example, the surface area enhancement's resulting increase in signal allowed us to reduce the length of the working electrode of an indwelling EAB sensor to just 500 µm, representing a 6-fold miniaturization of the working electrode relative to previous in vivo sensors in this class[1-3,5,6,31]. The resulting miniaturization offers a route forward for sensing systems where smaller working electrodes are critical, such as performing targeted measurements in brain regions, and developing wearable, minimally-invasive devices. The procedure is also simple, as it does not require clean room facilities and is compatible with any submersible gold surface. And unlike techniques such as co-sputtering and leaching of alloyed foil, the approach is readily compatible with the wire electrode format we employ for in vivo sensors. It may thus likewise prove useful for other sensing architectures, such as electrodes embedded in fluidic channels, rod electrodes, and gold-functionalized micropipettes. Given this, we believe it could prove useful for enhancing the performance of a wide range of electrochemical sensors.

3.5 MATERIALS AND METHODS

Electrode Fabrication

For in-vitro experiments, we fabricated sensors by soldering a 5 cm long gold wire (For **Figures 2-3**: 200 µm diameter from Alfa Aesar, Haverhill, MA. For **Figures 4-5**: 75 µm diameter from A-M Systems, Sequim, WA) to a gold-plated pin connector (CH Instruments, Inc., Austin, TX) with 60/40 lead-selenium solder (Digikey, Thief River Falls, MN). We isolated the desired length at the end of the gold wire by insulating with a layer of polytetrafluoroethylene (PTFE) heat-shrink tubing (HS Sub-Lite-Wall

PTFE, ZEUS, Orangeburg, SC) with an industrial hot air blower (Master Appliance Corp., Racine, WI).

For in vivo experiments, we fabricated the sensor probe by bundling 7.5 cm long, 75 µm diameter gold, platinum, and silver wires (A-M Systems, Sequim, WA) together using the same PTFE heat-shrink tubing used for in-vitro sensors. Using a digital caliper and razor blade, we trimmed the lengths of exposed wire to measure 3 mm, 4 mm, and 4 mm for the gold, platinum and silver wires, respectively. To prevent contact between the wires, we left a ~0.75 mm gap between each wire. To form a reference electrode, we deposited an AgCl layer on the silver wire by immersing the wire bundle in a concentrated sodium hypochlorite solution (Chlorox bleach) for at least 1 h. We rinsed the bundled wires in deionized water, then cleaned and modified them with aptamer as described below. Care was taken to avoid immersing the reference electrode into the NaOH or H_2SO_4 solutions used in subsequent steps, as these can damage the AgCl layer.

Electrode Electrochemical Cleaning

For electrode cleaning and in-vitro characterization, our electrochemical cell contained a PTFE-wrapped gold sensor working electrode, a platinum counter electrode (CH Instruments, Inc, Austin, TX), and an Ag|AgCl reference electrode (CH Instruments, Inc., Austin TX). We secured our working, counter, and reference electrodes in a cell vessel “shot glass” with a custom-fabricated Teflon lid fixture (See **Figure 3A**). First, we electrochemically cleaned the electrodes in 0.5 M NaOH (Sigma-

Aldrich, St. Louis, MO) by performing repeated cyclic voltammetry scans between -1 and -1.6 V (all potentials versus Ag|AgCl) at 1 V s^{-1} scan rate for 300 cycles using a CH Multipotentiostat (CHI1040C, CH Instruments, Inc.). We rinsed the electrodes in deionized water, then immersed them in 50 mM H_2SO_4 (Sigma Aldrich, St. Louis, MO). We recorded a series of five cyclic voltammograms in 50 mM H_2SO_4 (sweeping between 0 and 1.8 V at 0.1 V s^{-1}). To determine the electrode surface area, we measured the area under the cyclic voltammogram curve associated with the gold oxide reduction peak and divided it by the charge density of a monolayer of chemisorbed oxygen on gold (~400 µC cm^{-2}, see ref[6]). We then rinsed the electrodes in deionized water.

Nanoporous Gold Deposition and Surface Area Measurements

We dissolved 1.5 M $ZnCl_2$ (≥98%, Sigma Aldrich, St. Louis, MO) in anhydrous ethylene glycol (99.8%, Sigma Aldrich, St. Louis, MO) by alternatively heating (at 115˚C in a mineral oil bath) and vortexing the mixture. The solution was then added to the electrochemical cell, covered with a 0.5 cm layer of mineral oil, and immersed in a mineral oil bath heated to 115˚C. As both counter and reference electrodes, we inserted ~0.75 cm wide pieces of zinc foil (0.25 mm thick, 99.9% trace metals basis, Sigma Aldrich, St. Louis, MO) which had been sanded with a file, rinsed thoroughly in deionized water, and dried prior to use. We then connected the reference electrode, the counter electrode, and up to six gold wire working electrodes in series to a CHI1040C multipotentiostat (CH Instruments, Inc., Austin TX). To perform alloying, we scanned the working electrodes with a cyclic voltammogram starting at 0 V, then scanning from 0.8 to 1.8 V at 0.01 V/s. We repeated this 10 times (**Figure S1**) before removing the working electrodes and rinsing them with deionized water. To remove the zinc from the alloy, we next immersed the working electrodes in 5 M HCl (Merck, Darmstadt, Germany) for 15 min with magnetic stir bar agitation. The electrodes were then removed and rinsed in deionized water.

To complete the dealloying process, we placed the electrodes in 50 mM H_2SO_4 and applied cyclic voltammetry (scanning between 0 and 1.8 V at 0.1 V s^{-1}) until residual Zn is removed and the reduction peaks appear consistent in height and area. Typically, this takes 5 to 15 cyclic voltammetry scans (see **Figure S2**). Using the area of the gold oxide reduction peak, we again calculate the electrode surface area. Dividing this by the original unmodified area provides the area enhancement factor.

To assess surface morphology and pore size, we captured images of the nanoporous gold using a FEI XL-30 Sirion scanning electron microscope. To do so we trimmed a portion of gold, affixed it to a mount with copper adhesive tape, and imaged at a 2500x magnification, then a 45,935x magnification. We used ImageJ's set scale and linear measure feature to estimate pore size using the SEM detail image in Figure 1D.

EAB Sensor Fabrication

We first thawed a 2 µL, aliquot of 100 µM aptamer (sequence below) modified with a 6-carbon thiol linker on the 5' end and methylene blue on the 3' end (Biosearch Technologies, Novato, CA, dual HPLC purification, stored at -20^{o}C).

Vancomycin aptamer:

5’-SH-$(CH_2)_6$- CGAGG GTACC GCAAT AGTAC TTATT GTTCG CCTAT TGTGG GTCGG-O-CH_2-$CHCH_2OH$-$(CH_2)_4$-NH-CO-$(CH_2)_2$-methylene blue-3’

Because the manufacturer provides the DNA constructs in oxidized form, which does not effectively immobilize onto the gold surface, we must reduce the disulfide bond before deposition. To do so, we combined 2 μL of 10 mM Tris (2-carboxyethyl) phosphine (TCEP, Sigma-Aldrich, St. Louis, MO) with the aptamer sample for a 1 h thiol reduction in the dark at room temperature. We then diluted the sample with 96 μL 1X phosphate buffered saline (PBS, ChemCruz 20X phosphate buffered saline, Santa Cruz Biotechnology, Dallas, TX) and quantified the concentration of the aptamer using the molar absorption coefficient at 260 nm provided by the supplier with UV-VIS spectroscopy (DU800, Beckman Coulter, Brea, CA). Using PBS, we then diluted the aptamer to 500 nM.

As the final step in sensor fabrication, we placed the freshly-cleaned gold surface in the prepared aptamer solution for 1 h at room temperature in the dark. We then rinsed the electrodes with deionized water and immersed them for 12 to 18 h at room temperature in a 10 mM 6-mercapto-1-hexanol (Sigma-Aldrich, St. Louis, MO) in 1× PBS to passivate the surface. Following a final rinse with deionized water, the sensor was ready for use.

In-vitro Experiments

We filled the electrochemical cell with PBS, rinsed the electrodes in deionized water, and secured them in the electrochemical cell's Teflon cap. We collected a baseline cyclic voltammogram in PBS (-0.1 to – 0.5 V, 0.1 V/s). We calculate the redox reporter charge transfer in coulombs using the area determination feature of the CH potentiostat software, which quantifies charge transfer using the area of the reduction peak and cyclic voltammogram scan rate. We moved the electrode cap to the selected media (PBS or heparinized bovine blood, acquired from Hemostat Laboratories, Dixon, CA), and performed repeated square wave voltammetry scans (-0.2 to -0.4 V, 25 mV amplitude) at a frequency where the square wave voltammetry peak signal decreases in response to target ("signal-off," here 10 Hz), and a frequency where the square wave voltammetry peak signal increases in response to target ("signal-on," here 60 Hz). It is common to observe a downward drift in square wave voltammogram peak current, especially in complex media, such as whole blood. To correct for any peak signal loss, we applied a previously-described drift correction technique termed "Kinetic Differential Measurements" (KDM)[1,2,32]. In KDM, the normalized signal off-peak currents are subtracted from the signal-on peak currents. When these two signals drift roughly in concert, this enables correction of drift in complex environments.

In vivo Experiments

For in vivo experiments, we prepared our sensors by inserting the wire bundle probes into a 22 gauge catheter (BD Insyte Autoguard shielded IV catheter, BD, Franklin Lakes, NJ) that has ~2 mm windows cut into the catheter wall to expose the platinum and AgCl wires. To prevent air bubbles in the catheter, a syringe with a 27 gauge needle was used to fill the syringe with PBS. Once filled, we inserted the syringe into a PBS cell and collect a cyclic voltammogram (-0.1 to -0.5 V versus AgCl wire, or Ag|AgCl frit reference) to confirm the presence of aptamer signal and a well-formed monolayer.

The Institutional Animal Care and Use Committee (IACUC) of the University of California at Santa Barbara approved our experimental protocol, which adhered to the guidelines provided by the NIH Guide for Care and Use of Laboratory Animals (8th edition, National Academy Press, 2011)[33]. The Sprague Dawley rats weighed 660 to 760 g, and were pair housed in a 12:12 standard light cycle room with ad libitum access to food and water.

We surgically inserted the sensor-catheter assembly into the right jugular vein of a Sprague-Dawley rat (Charles River Laboratories, Santa Cruz, CA) as described previously[1,2,31]. Briefly, we shaved the chest area above the right and left jugular veins, and cleaned the skin using betaine and 70% ethanol. We anesthetized the rat using 5% isoflurane in a plexiglass anesthesia chamber, then maintained 2 to 3% isoflurane/oxygen anesthesia throughout the experiment using a nose cone.

To enable delivery of vancomycin (100 mM in filtered PBS), we installed a silastic catheter and infusion line into the left jugular vein as previously described[2] using a steel cannula with a screw-type connector (Plastics One, Roanoke, VA) and silastic tubing (11 cm, i.d. 0.64 mm, o.d. 1.19 mm, Dow Corning, Midland, MI). We secured the sensor and infusion lines using a sterile 6-0 silk suture (Fine Science Tools, Foster City, CA), and manually infused 30 units of heparin into the venous system prior to electrochemical measurements. We then connected the infusion line to a syringe of 100 mM vancomycin positioned on a syringe pump (KDS 200, KD Scientific Inc., Holliston, MA, USA).

Using alligator clips, we connected to the sensor probe to the potentiostat (for single sensor experiments we used the single channel CHI1242B; for multiplexed experiments, such as **Figure S3**, we used the multichannel CHI1040C). To confirm sensor connection and proper function, we first collected a cyclic voltammogram and baseline square wave voltammogram at 10 Hz. We continuously recorded square wave voltammograms at signal-off (10 Hz for both nanoporous and dendrite) and signal-on (60 Hz for nanoporous, 300 Hz for dendrite) frequencies, using the previously-described python script[34] to plot data in real time. After collecting a 15 to 30 min baseline, we used the syringe pump to inject a 40 mg/kg dose of vancomycin at a rate of 0.1 mL/min.

Data Analysis

To analyze square wave voltammetry peak currents in real time, we used a previously-reported, open source python script[34]. When provided with voltammogram bounds (typically, -0.21 to -0.39 V) and desired Savitzky–Golay filtering (5 mV for in-vitro data, 30 mV for in vivo data), this script calculates peak height and KDM values. Raw data from this program is exported to Matlab for data analysis and presentation. To calculate cyclic voltammogram reduction peak areas, we use the on-board area calculation tool provided with the CH software interface.

3.6 ACKNOWLEDGEMENTS

This work was funded by NIH grant R01AI145206 (to KWP). This material is based upon work supported by the National Science Foundation Graduate Research Fellowship under Grant No. 1650114 (AD). The content of the information does not necessarily reflect the position or the policy of the Government, and no official endorsement should be inferred. We also acknowledge financial contributions from the Natural Sciences and Engineering Research Council of Canada (NSERC-RGPIN-2016-06122 to HBK) and the University of Toronto at Scarborough.

3.7 SUPPLEMENTAL INFORMATION

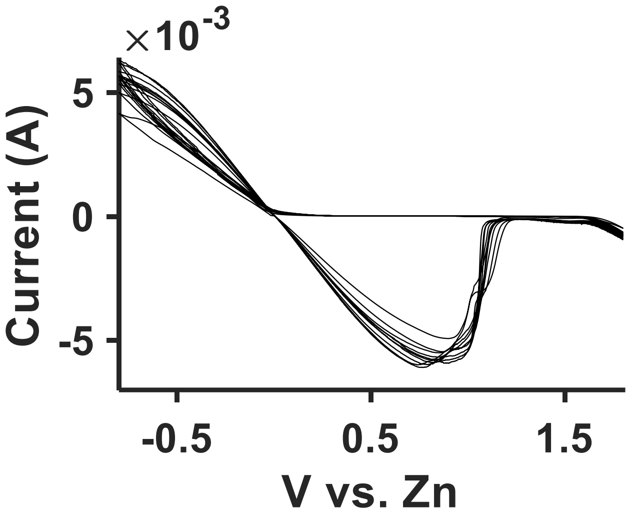

Figure S1: Shown is a cyclic voltammagram taken during the alloying/dealloying process. The conditions were 1.5 M $ZnCl_2$ in 115˚C ethylene glycol, with 6 wire electrodes connected in series. In this electrochemical cell, zinc foil is used both as the counter and reference electrode.

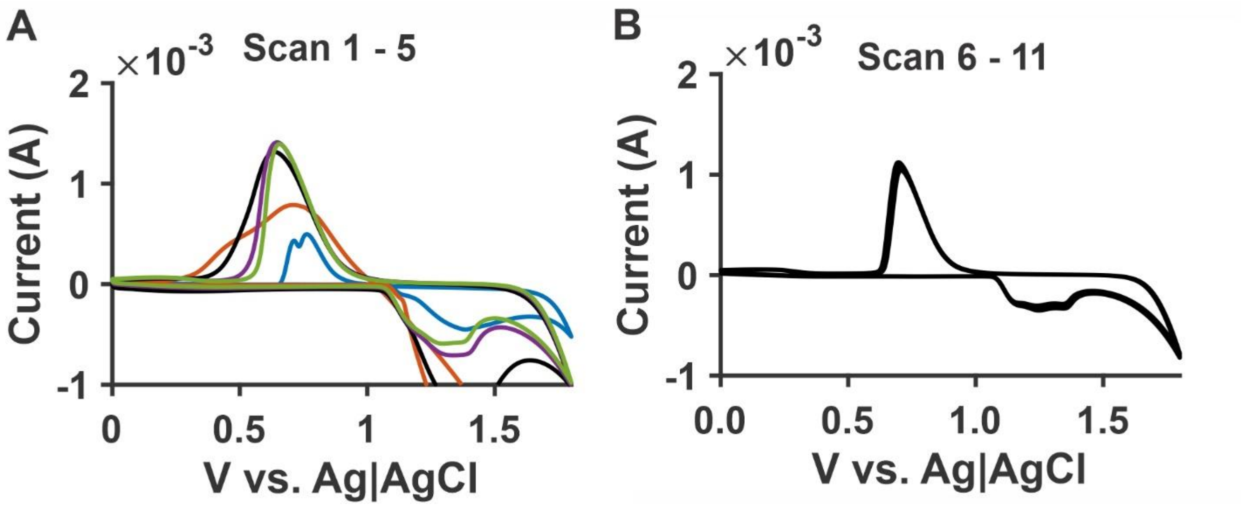

Figure S2: After dealloying the gold-zinc alloy in concentrated HCl, we rinse the electrodes and immerse them into 50 mM H_2SO_4 for a final surface cleaning via cyclic voltammetry. (A) The first few cyclic voltammograms (order: blue, orange, black, purple, green) demonstrate a change in the reduction peak, which we hypothesis to be removal of any remaining zinc or HCl in the matrix. (B) After 5-10 additional scans, we observe consistent peak appearance, and conjugate the wire electrodes as EAB sensors.

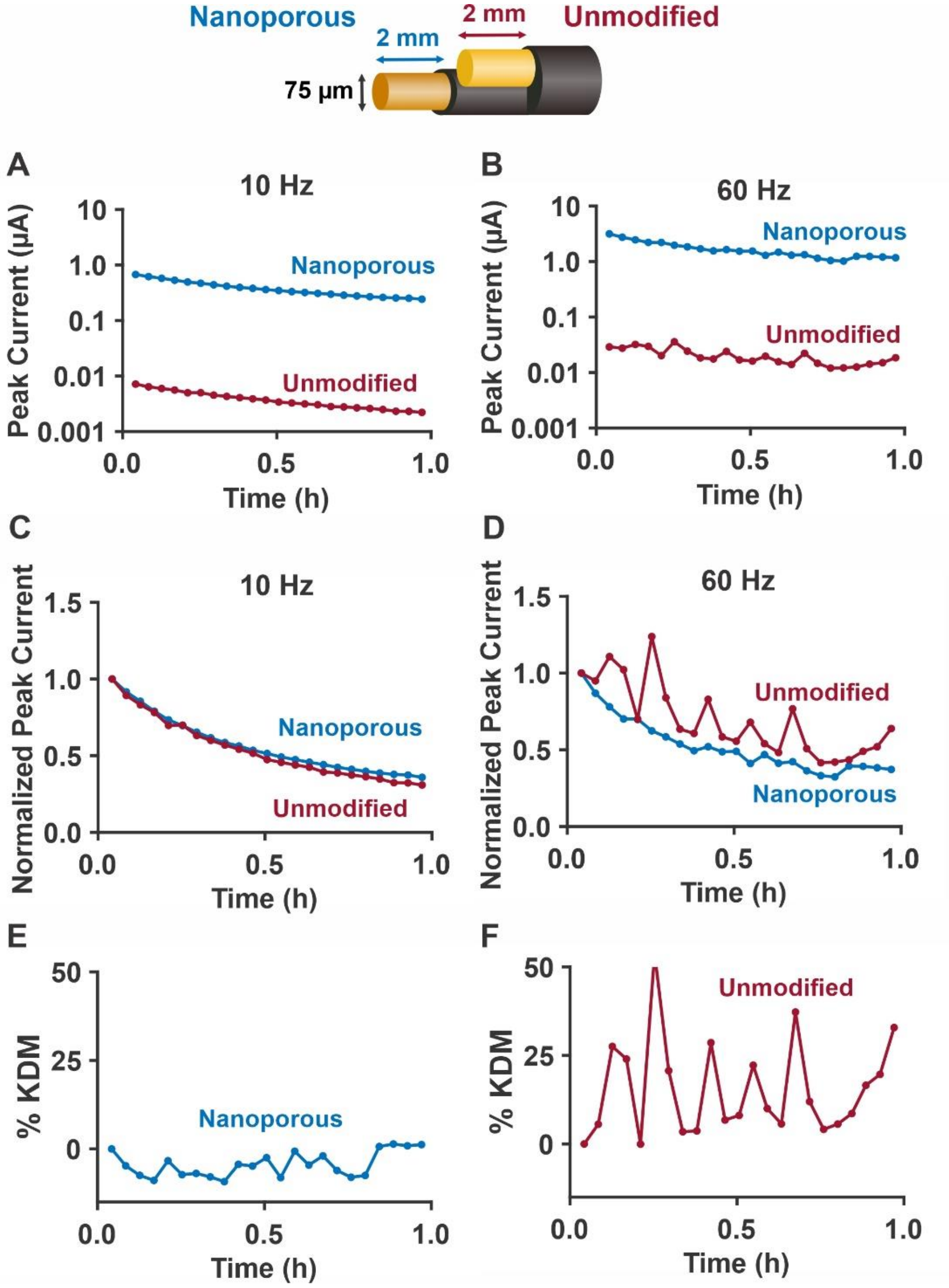

Figure S3: Sensors fabricated on unmodified and nanoporous gold drift at similar rates when deployed in the jugular vein, but the unmodified substrates exhibit higher noise. Here, we simultaneously interrogated a 75 µm diameter 2-mm-long sensor fabricated on unmodified (red) and nanoporous gold (blue) placed into the same jugular vein of a single rat. Here, we measure a baseline signal with no vancomycin addition. For both **(A)** 10 Hz and **(B)** 60 Hz, the nanoporous gold electrode has higher square wave voltammogram peak signal. **(C)** As seen from the normalized signals at 10 Hz, the peak currents drift at the same rate regardless of morphology. (D) However, at 60 Hz the noise level for the unmodified substrate is higher. As a result, the baseline KDM signal, which represent the subtracted normalized 60 Hz and 10 Hz peak signals, has substantially lower noise for the **(E)** nanoporous substrate than for the **(F)** unmodified substrate.

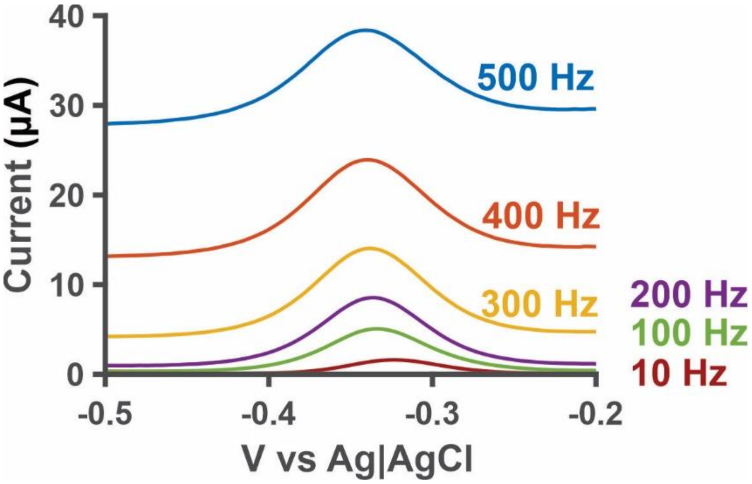

Figure S4: The contribution of charging currents to voltammogram baselines increases with square-wave frequency. Here, we show an EAB sensor constructed on a 3 mm long, 75 µm diameter nanoporous gold wire (area enhancement = 90-fold) interrogated in PBS at the indicated square-wave frequencies.

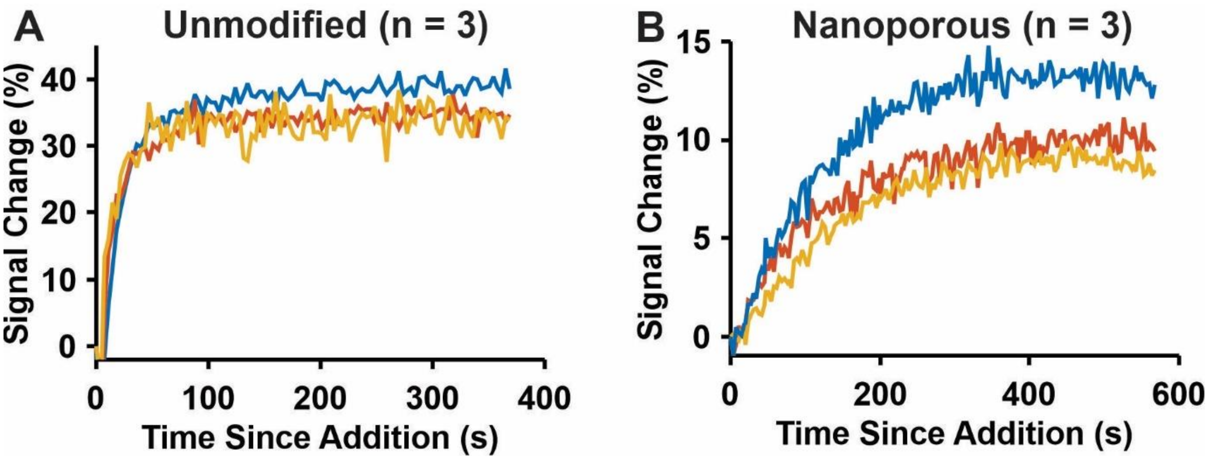

Figure S5: While the use of nanoporous gold does not measurably slow the equilibration of sensors directed against the small molecule target, vancomycin (1.4 kDa) (**Figure 4**), it does slow the response time of sensors against the higher molecular weight target, Ngal (a 25 kDa protein). Shown are the response times of an Ngal-detecting sensors fabricated using **(A)** unmodified (n =3) and **(B)** nanoporous gold (n = 3) upon challenge with 1 mM of the protein. Here, we present percent signal change of square wave voltammogram peak height for a signal-on frequency (60 Hz).

3.7 REFERENCES

(1) Arroyo-Currás, N.; Ortega, G.; Copp, D. A.; Ploense, K. L.; Plaxco, Z. A.; Kippin, T. E.; Hespanha, J. P.; Plaxco, K. W. High-Precision Control of Plasma Drug Levels Using Feedback-Controlled Dosing. *ACS Pharmacology & Translational Science* **2018**, *1*, 110-118, 10.1021/acsptsci.8b00033.
(2) Arroyo-Currás, N.; Somerson, J.; Vieira, P. A.; Ploense, K. L.; Kippin, T. E.; Plaxco, K. W. Real-time measurement of small molecules directly in awake, ambulatory animals. *Proceedings of the National Academy of Sciences* **2017**, *114*, 645-650, 10.1073/pnas.1613458114.
(3) Parolo, C.; Idili, A.; Ortega, G.; Csordas, A.; Hsu, A.; Arroyo-Currás, N.; Yang, Q.; Ferguson, B. S.; Wang, J.; Plaxco, K. W. Real-Time Monitoring of a Protein Biomarker. *ACS sensors* **2020**, *5*, 1877-1881, 10.1021/acssensors.0c01085.
(4) Cobb, S. J.; Macpherson, J. V. Enhancing Square Wave Voltammetry Measurements via Electrochemical Analysis of the Non-Faradaic Potential Window. *Analytical Chemistry* **2019**, *91*, 7935-7942, 10.1021/acs.analchem.9b01857.
(5) Dauphin-Ducharme, P.; Yang, K.; Arroyo-Currás, N.; Ploense, K. L.; Zhang, Y.; Gerson, J.; Kurnik, M.; Kippin, T. E.; Stojanovic, M. N.; Plaxco, K. W. Electrochemical Aptamer-Based Sensors for Improved Therapeutic Drug Monitoring and High-Precision, Feedback-Controlled Drug Delivery. *ACS sensors* **2019**, *4*, 2832-2837, 10.1021/acssensors.9b01616.

(6) Arroyo-Currás, N.; Somerson, J.; Vieira, P. A.; Ploense, K. L.; Kippin, T. E.; Plaxco, K. W. Real-time measurement of small molecules directly in awake, ambulatory animals. **2017**, *114*, 645-650, 10.1073/pnas.1613458114 %J Proceedings of the National Academy of Sciences.
(7) Kashefi-Kheyrabadi, L.; Mehrgardi, M. A. Aptamer-based electrochemical biosensor for detection of adenosine triphosphate using a nanoporous gold platform. *Bioelectrochemistry* **2013**, *94*, 47-52, 10.1016/j.bioelechem.2013.05.005.
(8) Qiu, H.; Sun, Y.; Huang, X.; Qu, Y. A sensitive nanoporous gold-based electrochemical aptasensor for thrombin detection. *Colloids and Surfaces B: Biointerfaces* **2010**, *79*, 304-308, 10.1016/j.colsurfb.2010.04.017.
(9) Liu, J.; Wagan, S.; Dávila Morris, M.; Taylor, J.; White, R. J. Achieving Reproducible Performance of Electrochemical, Folding Aptamer-Based Sensors on Microelectrodes: Challenges and Prospects. *Analytical Chemistry* **2014**, *86*, 11417-11424, 10.1021/ac503407e.
(10) Yang, W.; Gerasimov, J. Y.; Lai, R. Y. Folding-based electrochemical DNA sensor fabricated on a gold-plated screen-printed carbon electrode. *Chemical Communications* **2009**, 2902-2904, 10.1039/B904550C.
(11) Kiani, A.; Fard, E. N. Fabrication of palladium coated nanoporous gold film electrode via underpotential deposition and spontaneous metal replacement: A low palladium loading electrode with electrocatalytic activity. *Electrochimica Acta* **2009**, *54*, 7254-7259, 10.1016/j.electacta.2009.07.037.
(12) Ji, C.; Searson, P. C. Fabrication of nanoporous gold nanowires. **2002**, *81*, 4437-4439, 10.1063/1.1526920.
(13) Rouya, E.; Reed, M. L.; Kelly, R. G.; Bart-Smith, H.; Begley, M.; Zangari, G. Synthesis of Nanoporous Gold Structures via Dealloying of Electroplated Au-Ni Alloy Films. *ECS Transactions* **2007**, *6*, 41-50, 10.1149/1.2790413.
(14) Cherevko, S.; Chung, C.-H. Direct electrodeposition of nanoporous gold with controlled multimodal pore size distribution. *Electrochemistry Communications* **2011**, *13*, 16-19, 10.1016/j.elecom.2010.11.001.
(15) Seker, E.; Reed, M. L.; Begley, M. R. Nanoporous Gold: Fabrication, Characterization, and Applications. *Materials (Basel)* **2009**, *2*, 2188-2215, 10.3390/ma2042188.
(16) Veselinovic, J.; AlMashtoub, S.; Nagella, S.; Seker, E. Interplay of Effective Surface Area, Mass Transport, and Electrochemical Features in Nanoporous Nucleic Acid Sensors. *Analytical Chemistry* **2020**, *92*, 10751-10758, 10.1021/acs.analchem.0c02104.
(17) Matharu, Z.; Daggumati, P.; Wang, L.; Dorofeeva, T. S.; Li, Z.; Seker, E. Nanoporous-Gold-Based Electrode Morphology Libraries for Investigating Structure–Property Relationships in Nucleic Acid Based Electrochemical Biosensors. *ACS Applied Materials & Interfaces* **2017**, *9*, 12959-12966, 10.1021/acsami.6b15212.
(18) Zhu, Y.; Zhou, C.; Yan, X.; Yan, Y.; Wang, Q. Aptamer-functionalized nanoporous gold film for high-performance direct electrochemical detection of bisphenol A in human serum. *Analytica Chimica Acta* **2015**, *883*, 81-89, 10.1016/j.aca.2015.05.002.
(19) Xia, Y.; Huang, W.; Zheng, J.; Niu, Z.; Li, Z. Nonenzymatic amperometric response of glucose on a nanoporous gold film electrode fabricated by a rapid and

simple electrochemical method. *Biosensors and Bioelectronics* **2011**, *26*, 3555-3561, 10.1016/j.bios.2011.01.044.
(20) Downs, A. M.; Gerson, J.; Ploense, K. L.; Plaxco, K. W.; Dauphin-Ducharme, P. Subsecond-Resolved Molecular Measurements Using Electrochemical Phase Interrogation of Aptamer-Based Sensors. *Analytical Chemistry* **2020**, *92*, 14063-14068, 10.1021/acs.analchem.0c03109.
(21) Xiao, X.; Si, P.; Magner, E. An overview of dealloyed nanoporous gold in bioelectrochemistry. *Bioelectrochemistry* **2016**, *109*, 117-126, 10.1016/j.bioelechem.2015.12.008.
(22) S. Trasatti, O. A. P. Real Surface Area Measurements in Electrochemistry. *Journal of Electroanalytical Chemistry* **1992**, *327*, 353-376,
(23) Hossain, M. N.; Liu, Z.; Wen, J.; Chen, A. Enhanced catalytic activity of nanoporous Au for the efficient electrochemical reduction of carbon dioxide. *Applied Catalysis B: Environmental* **2018**, *236*, 483-489, 10.1016/j.apcatb.2018.05.053.
(24) Jia, F.; Yu, C.; Ai, Z.; Zhang, L. Fabrication of Nanoporous Gold Film Electrodes with Ultrahigh Surface Area and Electrochemical Activity. *Chemistry of Materials* **2007**, *19*, 3648-3653, 10.1021/cm070425l.
(25) van der Zalm, J.; Chen, S.; Huang, W.; Chen, A. Review—Recent Advances in the Development of Nanoporous Au for Sensing Applications. *Journal of The Electrochemical Society* **2020**, *167*, 037532, 10.1149/1945-7111/ab64c0.
(26) Deng, M.; Li, M.; Li, F.; Mao, X.; Li, Q.; Shen, J.; Fan, C.; Zuo, X. Programming Accessibility of DNA Monolayers for Degradation-Free Whole-Blood Biosensors. *ACS Materials Letters* **2019**, *1*, 671-676, 10.1021/acsmaterialslett.9b00404.
(27) Ramaley, L.; Krause, M. S. Theory of square wave voltammetry. *Analytical Chemistry* **1969**, *41*, 1362-1365, 10.1021/ac60280a005.
(28) Macias, G.; Ferré-Borrull, J.; Pallarès, J.; Marsal, L. F. Effect of pore diameter in nanoporous anodic alumina optical biosensors. *Analyst* **2015**, *140*, 4848-4854, 10.1039/C4AN01408A.
(29) Arshavsky Graham, S.; Boyko, E.; Salama, R.; Segal, E. Mass Transfer Limitations of Porous Silicon-Based Biosensors for Protein Detection. *ACS Sensors* **2020**, 10.1021/acssensors.0c00670.
(30) Collinson, M. M. Nanoporous Gold Electrodes and Their Applications in Analytical Chemistry. *ISRN Analytical Chemistry* **2013**, *2013*, 692484, 10.1155/2013/692484.
(31) Arroyo-Currás, N.; Dauphin-Ducharme, P.; Ortega, G.; Ploense, K. L.; Kippin, T. E.; Plaxco, K. W. Subsecond-Resolved Molecular Measurements in the Living Body Using Chronoamperometrically Interrogated Aptamer-Based Sensors. *ACS Sensors* **2018**, *3*, 360-366, 10.1021/acssensors.7b00787.
(32) Ferguson, B. S.; Hoggarth, D. A.; Maliniak, D.; Ploense, K.; White, R. J.; Woodward, N.; Hsieh, K.; Bonham, A. J.; Eisenstein, M.; Kippin, T. E.; Plaxco, K. W.; Soh, H. T. Real-time, aptamer-based tracking of circulating therapeutic agents in living animals. *Science translational medicine* **2013**, *5*, 213ra165, 10.1126/scitranslmed.3007095.
(33) In *Guide for the Care and Use of Laboratory Animals*; National Academies Press (US) Copyright © 2011, National Academy of Sciences.: Washington (DC), 2011.

(34) Curtis, S. D.; Ploense, K. L.; Kurnik, M.; Ortega, G.; Parolo, C.; Kippin, T. E.; Plaxco, K. W.; Arroyo-Currás, N. Open Source Software for the Real-Time Control, Processing, and Visualization of High-Volume Electrochemical Data. *Analytical Chemistry* **2019**, *91*, 12321-12328, 10.1021/acs.analchem.9b02553.

CHAPTER 4: IMPROVED CALIBRATION OF ELECTROCHEMICAL APTAMER-BASED SENSORS

4.1 ABSTRACT

Electrochemical aptamer-based (EAB) sensors support the real-time, high frequency measurement of pharmaceuticals, metabolites, and proteins in-situ in the living body, rendering them a potentially powerful technology for both research and clinical applications. Here we explore quantification using EAB sensors, examining the impact of media selection and temperature on measurement performance. Using freshly-collected, undiluted whole blood at body temperature as our calibration and measurement conditions, we demonstrate accuracy of better than ±11% over the clinically relevant range of our test bed drug, vancomycin. Comparing titrations collected at room and body temperature, we find that matching temperature of calibration curve collection to temperature used during measurements improves quantification by reducing differences in sensor gain and binding curve midpoint. We likewise find that, because blood age impacts the sensor response, calibrating in freshly collected blood can improve quantification. Finally, we demonstrate the use of non-blood calibration proxies to achieve calibration without the need to collect fresh whole blood.

4.2 INTRODUCTION

Electrochemical aptamer-based (EAB) sensors support high-frequency[1,2], real-time molecular measurements[3,4] directly in complex biological media, including unprocessed, undiluted bodily fluids[5,6]. To achieve this, EAB sensors utilize a redox-reporter-modified aptamer attached to a gold electrode via a self-assembled monolayer (**Figure 1A**)[5,7]. Upon target binding, the aptamer undergoes a conformational change, producing an easily-measurable shift in electrochemical signal[8]. As these sensors include both a recognition element (the aptamer) and a signaling moiety (the redox reporter), they do not require washing steps or reagent addition. And because they maintain their signaling properties in even complex sample matrices, such as undiluted whole blood, they perform well even when placed in situ in the living body[1,9-13]. Indeed, their ability to perform real-time molecular measurements in vivo even supports closed-loop feedback-controlled drug delivery[14,15]. Their utility for in-vivo measurements makes this class of sensors promising for clinical health monitoring and wearable devices.

While a number of electrochemical techniques[1,2,16,17] have been used to interrogate EAB sensors, converting the resulting signals into estimated target concentrations always relies on the use of a calibration curve. When applying square wave voltammetry, the most commonly employed interrogation technique, we produce the necessary calibration curve by collecting voltammogram peak currents over a range of target concentrations (**Figure 1C**). Of note, because of a square wave frequency-dependence on EAB signaling, square wave voltammetry can be tuned to yield an increase (“signal-on”) or a decrease (“signal-off”) in peak current upon target addition (**Figure 1B**)[8,18,19]. For in-vivo measurements, we use voltammograms collected at two such frequencies to perform "kinetic differential measurements," (KDM) in which we subtract the normalized peak currents seen at signal-on and signal-off frequencies to correct drift and enhance gain (**Figure 1C**)[20]. To generate a calibration curve, we fit averaged KDM values collected in vitro over a range of target concentrations to Hill-Langmuir isotherm [**Equation 1**][21]:

$$KDM = KDM_{min} + \frac{(KDM_{max} - KDM_{min}) * [Target]^{n_H}}{[Target]^{n_H} + K_{1/2}^{n_H}}$$

[1]

where n_H is the Hill coefficient (a measure of binding cooperativity), $K_{1/2}$ is the midpoint of the binding curve, KDM is the KDM value observed at the applied target concentration, KDM_{min} the KDM value seen in the absence of target, and KDM_{max} the KDM value expected at saturating target. After obtaining these parameters from a calibration curve, we can then translate EAB sensor output into estimates of target concentration [**Equation 2**].

$$[Target] = \sqrt[n_H]{\frac{K_{1/2}^{n_H} * (KDM - KDM_{min})}{KDM_{max} - KDM}} \qquad [2]$$

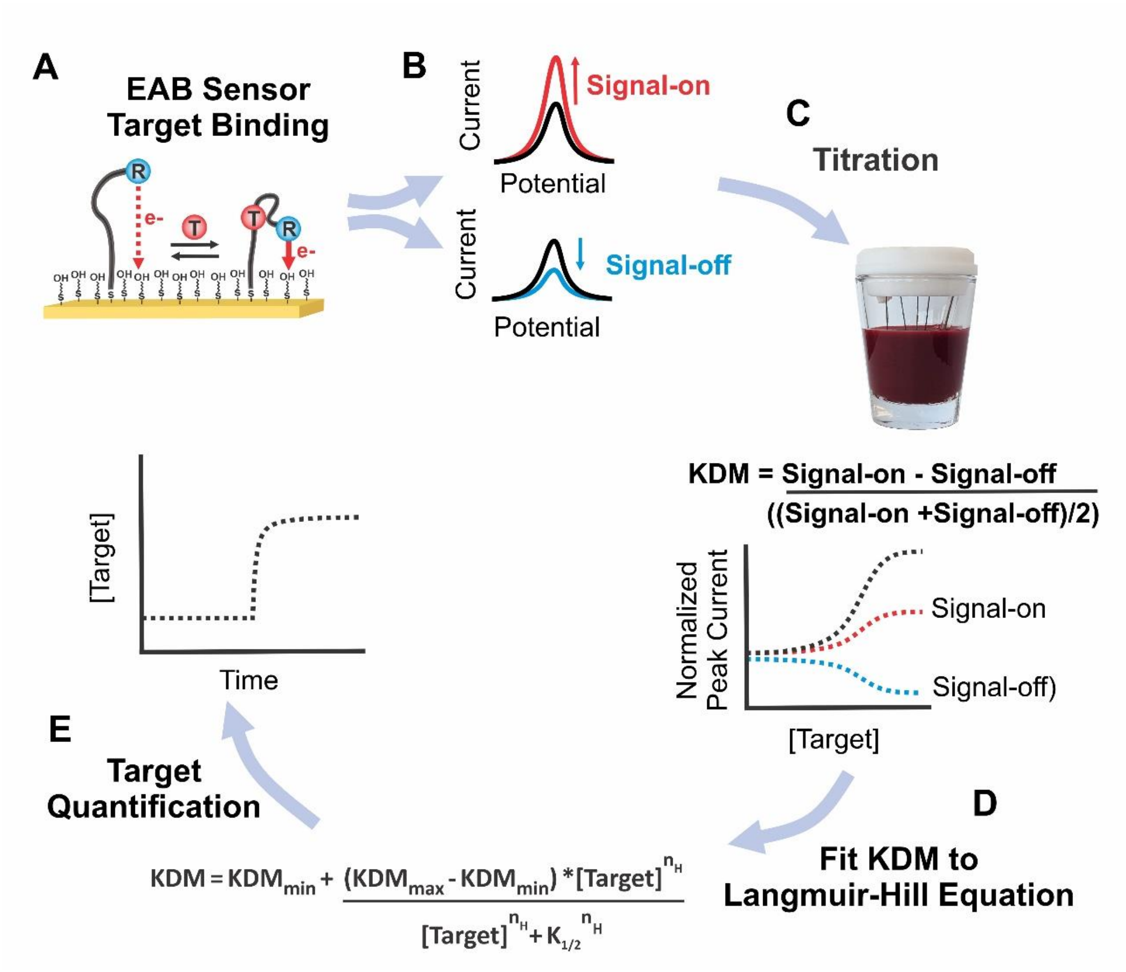

Figure 1: (A) EAB sensors consist of a redox-reporter-modified (R) aptamer attached to a gold electrode coated with a passivating self-assembled monolayer (here 6-mercapto-1-hexanol). Upon binding of target (T), a change in electron transfer kinetics between the redox reporter and the surface occurs, which is easily monitored using square wave voltammetry. **(B)** Depending upon the square-wave frequency employed, the peak currents seen in square wave voltammetry will increase ("signal on" behavior) or decrease ("signal off") in response to target binding. **(C)** To determine responses at different frequencies, we titrate the sensors with known amounts of target. To increase gain and correct for the appearance of drift, we obtain Kinetic Differential Measurement (KDM) values by taking the difference in normalized peak currents collected at a signal-on and a signal-off frequency, then dividing that value by the average of the signal-on and signal-off peak currents. **(D)** We then fit the KDM

values to a Hill-Langmuir equation, extracting parameters for KDM_{max} (the maximum KDM response, or gain), KDM_{min}, and $K_{1/2}$. **(E)** Using these parameters, we convert observed KDM measurements into concentration estimates.

EAB calibration curves thus depend on both the affinity of the aptamer, $K_{1/2}$, the cooperativity (or anti-cooperativity) of binding, n_H, and the sensor's signal gain, KDM_{max}. Given that both of these parameters are influenced by environmental factors, such as temperature[22,23], pH[24], ionic strength[24,25], careful selection of calibration conditions is required in order to achieve optimal measurement accuracy and precision. Here, we examine calibration in detail, investigating the impact of media temperature, age, and composition on the observed calibration curves obtained using square wave voltammetry. As our test bed, we examine the response for a sensor detecting the antibiotic target, vancomycin, using square wave frequencies of 25 and 300 Hz to generate a KDM signal.

4.3 RESULTS AND DISCUSSION

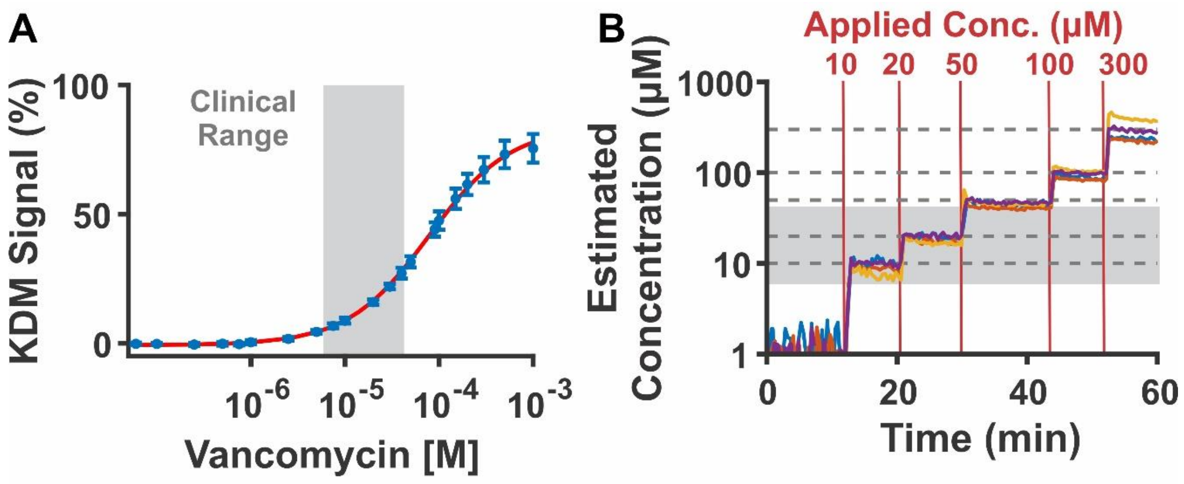

C

Actual concentration (µM)	10	20	50	100	300
Mean estimated concentration (µM)	9.2	18.7	44.6	94.9	286.4
Mean accuracy (µM)	0.8	1.3	5.4	5.1	13.6
Mean relative accuracy	- 8.2%	- 6.7%	- 10.8%	-5.1%	-4.6%
Standard deviation (µM)	1.3	1.7	3.0	9.1	68.4
Relative precision	± 28%	± 18%	± 14%	± 19%	± 48%

Figure 2: Vancomycin-detecting EAB sensors calibrated using a calibration curve collected in matched media and temperature easily achieve clinically useful measurement accuracy. **(A)** Here we created a calibration curve by fitting the average response of four sensors to a Hill-Langmuir isotherm using data collected at 37°C in freshly-collected rat blood. We derive KDM values by subtracting the normalized peak heights collected at 300 Hz from those collected at 25 Hz, and dividing by their average[20]. We indicate the clinical range of vancomycin in grey. **(B)** We then apply

this calibration curve to quantify measurements performed using the same four sensors in 37°C fresh rat blood to which (dotted lines) 10, 20, 50, 100, or 300 µM vancomycin has been added. We indicate the clinical range of vancomycin in grey. **(C)** We observe better than ±11% accuracy (defined as the mean percentage error from the actual drug concentration) for all challenges. Likewise, we achieve precision of better than 28% (defined as 2X standard deviation/mean value) over the clinical range of vancomycin.

EAB sensors calibrated in fresh whole rat blood under the conditions employed during the measurement achieve clinically useful performance. Specifically, when we apply parameters obtained from a calibration curve collected in fresh, body temperature (37˚C) rat blood to fresh rat blood held under the same conditions and containing various known concentrations of vancomycin (**Figure 2B**), we achieve accuracy of better than ±11% (**Table S1**). Here, we define accuracy as the mean percent deviation between the estimated and known concentrations. The clinical window of vancomycin is from 6-42 µm, which reflects the minimum target concentrations to achieve clinical effect, to the mean maximum peak concentrations concentrations[26,27]. To achieve the typical area under curve level of 400-600 mg*h/L, the targeted range for vancomycin varies from 6 to 14 µM[28]. Given the breadth of these ranges, 11% or better relative accuracy is sufficient to safely monitor delivery of this toxic antibiotic.

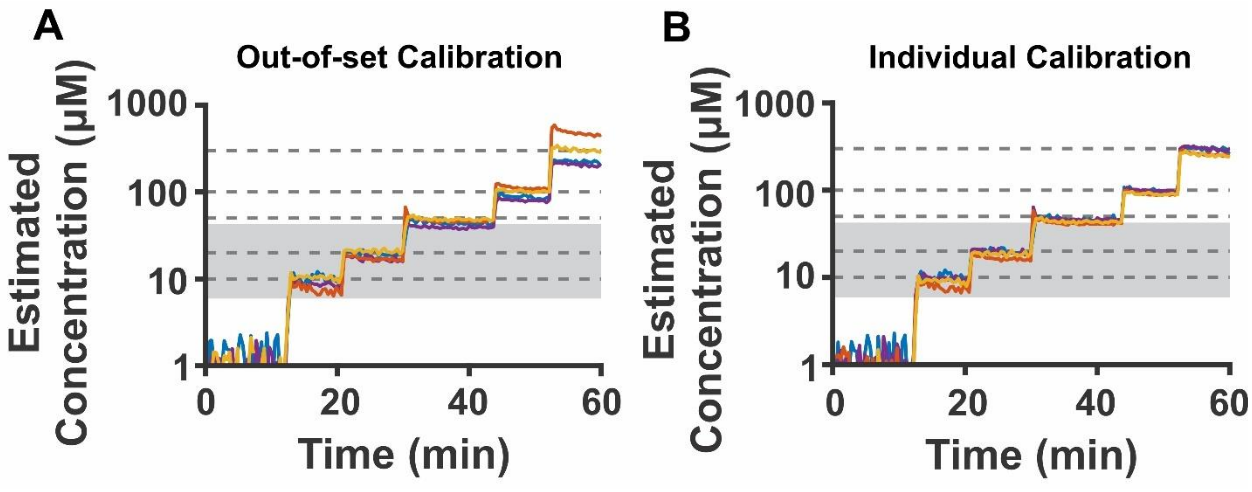

Figure 3: Calibrating sensors using out-of-set data, or calibrating individual sensors to their respective calibration curve does not greatly change sensor accuracy in vancomycin's clinical range (highlighted in grey). **(A)** To "individually" calibrate the sensors, we use the calibration curve collected for a specific sensor to quantify its resulting dose-response curve. **(B)** To calibrate sensors "out-of-set," for each sensor, we calibrate using a calibration curve formed from the other three sensors.

In the studies described above, we calibrated each individual sensor using a single, common calibration curve obtained by averaging the sensor's calibration curve with those of other vancomycin-detecting sensors. That is, each sensor was calibrated using a calibration curve to which it, itself, had also contributed. If, however, we instead use an "out-of-set" calibration curve, a calibration curve to which the sensor under investigation did not contribute (**Figure 3A**), we see no significant change in accuracy and only a slight reduction in precision over the clinically relevant range of vancomycin concentrations **(Table S1**). Likewise, if we use each sensor's own, individual calibration curve (**Figure 3B**) we see only small improvements in accuracy and precision over the clinical range (**Table S2**). These observations suggest that sensor-to-sensor variation is not contributing significantly to the level of accuracy and precision we achieve with this sensor at clinical target concentrations.

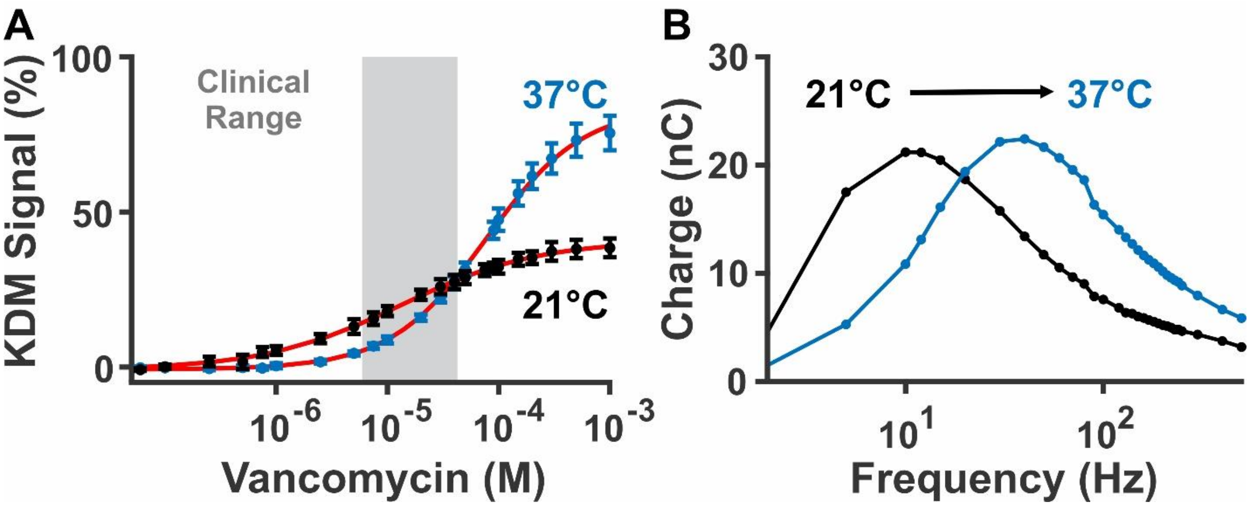

Figure 4: EAB signaling changes significantly between room and body temperature. **(A)** For example, calibration curves measured in freshly-collected rat blood at 21°C (black, n = 4 sensors, $K_{1/2}$ = 132 ± 2 µM) and 37°C (blue, n = 4 sensors, $K_{1/2}$ = 78 ± 7 µM) differ in their binding midpoint, their Hill coefficient, and their signal gain. **(B)** This occurs at least in part because the electron transfer rate from the redox reporter changes with temperature. Specifically, the, peak charge transfer rate shifts toward higher frequencies at higher temperatures. To illustrate this, we plot here charge transfer versus frequency for a representative sensor by determining square wave voltammogram peak current, and dividing it by its given interrogation frequency (additional sensor curves shown in **Figure S1**) [29].

Collecting calibration curves at the appropriate temperature is a key to sensor calibration. Specifically, between room and body temperature, calibration curves differ significantly (**Figure 4A**). Depending on interrogation frequency employed, this can lead to considerable under- or over-estimation of target concentrations. Interrogating at 25 and 300 Hz, for example, we observe up to a 10% higher KDM signal at room temperature than at body temperature over vancomycin's clinical concentration range. Consequently, applying a calibration curve collected at room temperature to those collected at body temperature causes concentration underestimates (**Figure S2**). Interrogating using other square wave frequency pairs, likewise, can yield significant differences in KDM signal in the clinical range (**Figure S3**). These differences in sensor response occur because temperature changes can shift system properties, such as binding equilibrium coefficients and the electron transfer rate itself. For example, the electron transfer rate (indicated by the location of peak charge transfer, when plotting interrogation frequency versus charge transfer) increases with temperature for the vancomycin aptamer (**Figure 4B**) as well as for EAB sensors against other targets (**Figures S4-6**). This shift is great enough that it can affect the selection of signal-on and signal-of frequencies. For example, from room temperature to body temperature, 25 Hz changes from a weak signal-on frequency to clear signal-off frequency (**Figure S7**).

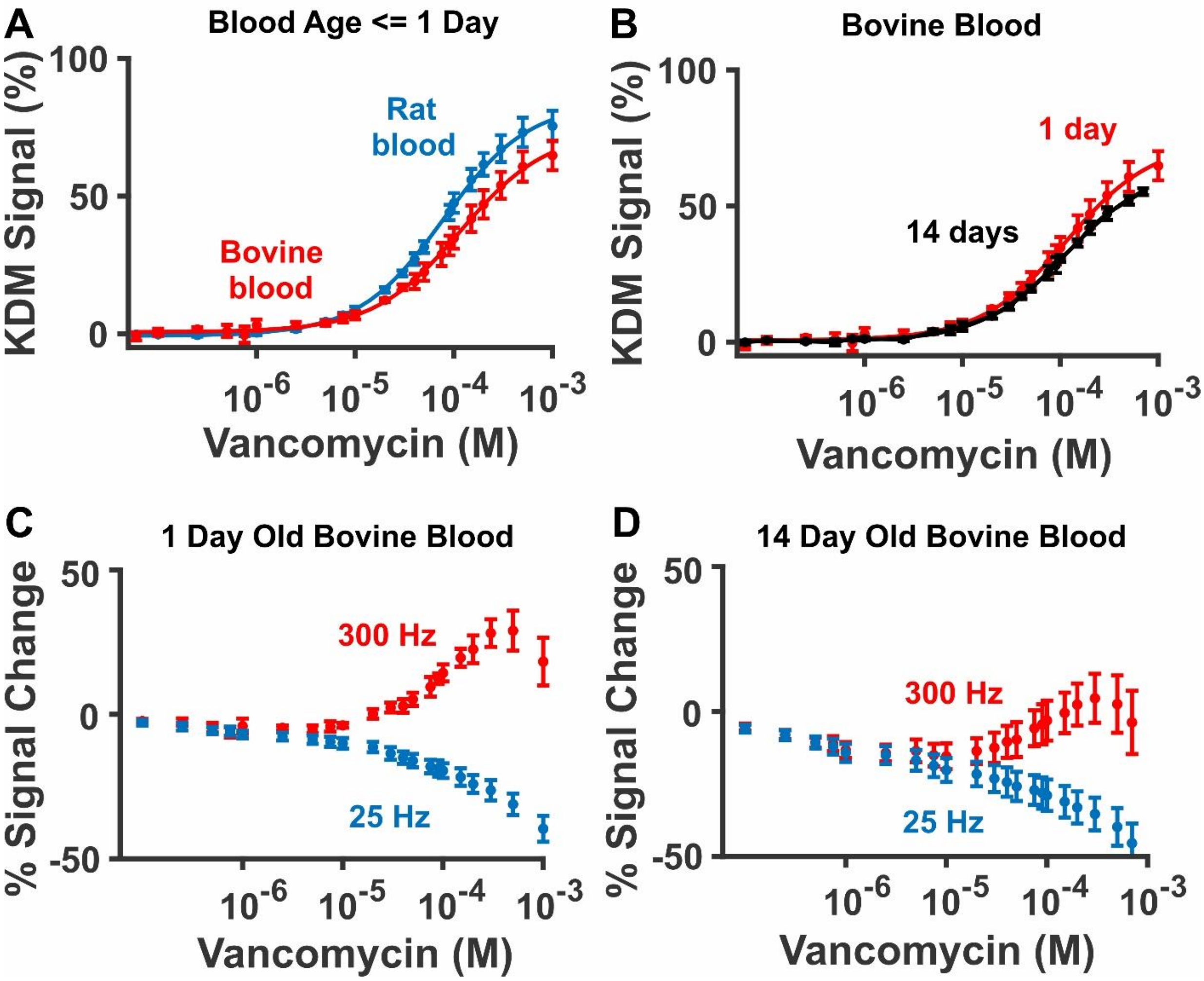

Figure 5: (A) Titrations performed in fresh rat blood and commercially sourced, one-day-old bovine blood produce distinct calibration curves. **(B)** To determine whether this is driven by species-specific differences in blood, or the greater age of the commercially sourced bovine blood, we compared calibration curves obtained in a bovine blood sample 1 day (red, K_D = 116 ± 15 µM) and 14 days (black, K_D = 114 ± 10 µM) after it was collected. Doing so, we find that the KDM response does not change significantly in the clinical range. **(C, D)** Examining the signal at the two square-wave frequencies used to perform KDM (here 25 Hz and 300 Hz) we see that, for the 14-day-old blood, there is a notable signal decrease at vancomycin

concentrations far below the K_D. Given that no target-induced response should occur at these low concentrations, we believe this is an artifact due to time-dependent sensor degradation in the older blood.

Obtaining bovine blood from commercial vendors is often more convenient than collecting fresh blood samples. Calibration curves obtained in the former matrix, however, deviate from those collected in the latter (**Figure 5A**). Specifically, in commercially sourced bovine blood, the vancomycin sensor's signal gain is reduced, such that using this calibration curve to quantify measurements performed in fresh blood would overestimate vancomycin concentration (**Figure 5A**). This could arise from differences in blood species source, the processing of the sample, or the age of the sample. Due to shipping, for example, commercially sourced blood is at least a day old by the time we use it. To determine whether blood age (time after initial blood collection) is an important calibration parameter, we titrated sensors in commercial bovine blood one day after collection and again using the blood from the same blood draw 13 days later. Doing so, we find that the older sample yielded similar signals in the clinical range, and slightly lower signal at concentrations above the clinical range (**Figure 5B**). While we observe a marked signal decrease at target concentrations below 1 µM, presumably due to sensor degradation occurring during the titration (**Figure 5C-D**), KDM effectively corrects for this signal loss in the clinical range.

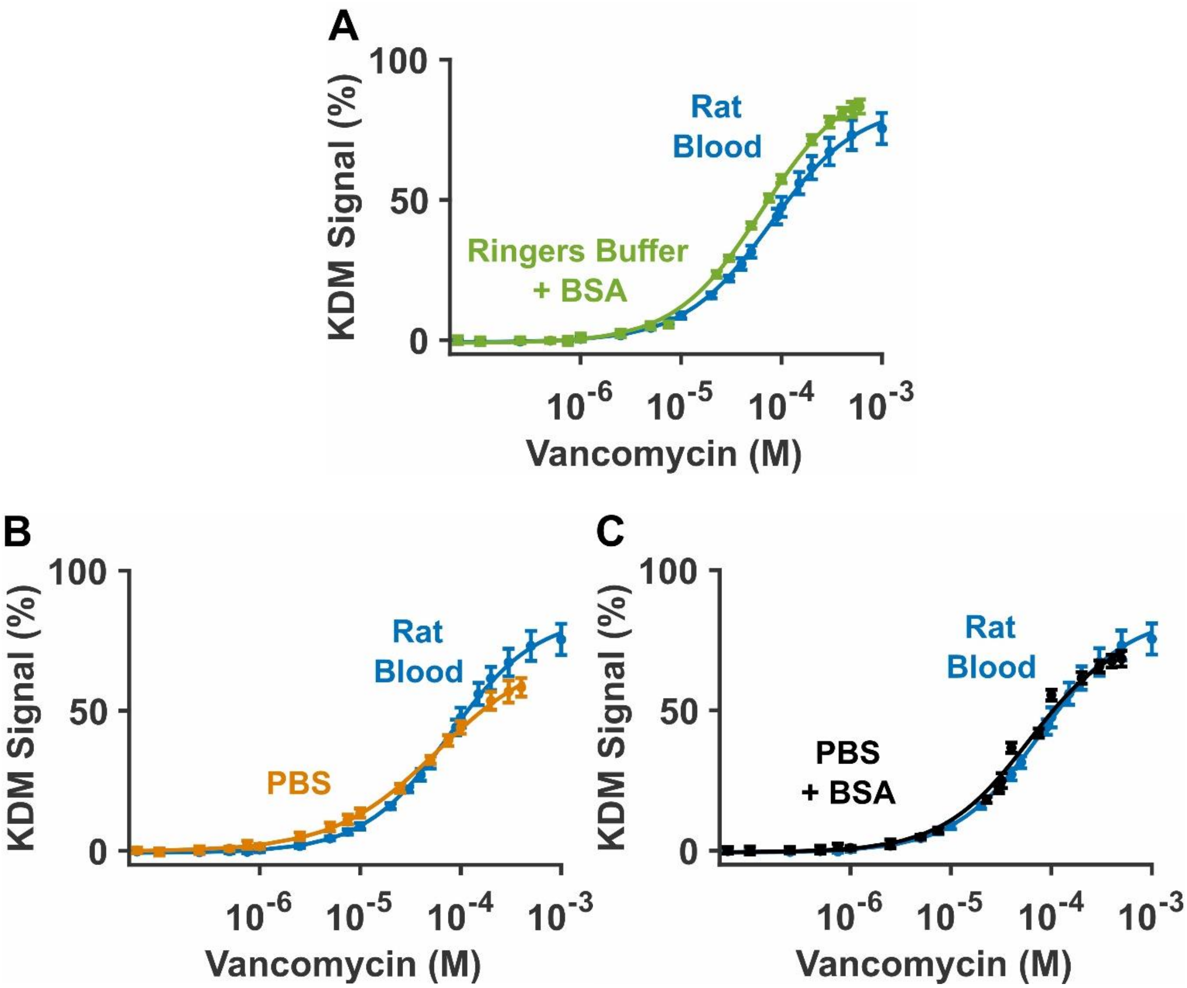

Figure 6: Here, we investigate whether simpler media can reproduce the response seen in freshly-collected rat blood. To do so, we compare titrations (KDM values derived from 25 Hz and 300 Hz) collected in 37°C freshly collected rat blood to **(A)** 37°C Ringer's buffer with 30 mg/mL bovine serum albumin (BSA), **(B)** 37°C phosphate buffered saline (PBS) with 2 mM $MgCl_2$, **(C)** and 37°C PBS with 2 mM $MgCl_2$ and 30 mg/mL bovine serum albumin.

Although it is the most accurate calibration matrix, the collection of fresh blood for sensor calibration can be inconvenient, leading us to ask if there are other, more easily obtained media that can reproduce sensor behavior in that matrix. To investigate this, we produced calibration curves in ringer's buffer containing 30 mg/mL bovine serum albumin, phosphate buffered saline (PBS) containing 2 mM $MgCl_2$, and PBS containing 2 mM $MgCl_2$ and 30 mg/mL bovine serum albumin. In ringer's buffer, the titration yields greater signal gain than that observed in rat blood (**Figure 6A**). Applying the resulting calibration curve, then, would lead to underestimation of vancomycin in rat blood. The PBS calibration curve, in contrast, exhibits a slightly different Hill coefficient (**Equation 1**), and thus would lead to under- or overestimates of vancomycin in rat blood (**Figure 6B**). A calibration curve collected in PBS with bovine serum albumin and magnesium, however, more accurately reproduces the calibration curve obtained in fresh rat blood (**Figure 6C**). Enough so that, when we quantify the successive vancomycin additions in body temperature rat blood with this calibration curve, we obtain accuracies greater than 26% - a level of accuracy that may be acceptable in some applications (**Figure S9, Table S3**). We note, however, that this buffer may not be an appropriate calibration matrix for all EAB sensors. We have previously found, for example, that ringer's buffer with bovine serum albumin is a good blood proxy for a phenylalanine-detecting EAB sensor[10]. Thus, the most appropriate proxy buffer likely varies by aptamer.

.

4.4 CONCLUSIONS

With the appropriate selection of media temperature, composition, and age, a vancomycin-detecting EAB sensor easily achieves clinically relevant accuracy.

Specifically, when calibrated at the appropriate temperature in freshly collected blood, sensors achieve accuracy of greater than 20% when challenged under those same conditions. This result holds for both sensors calibrated against themselves and for sensors calibrated against other sensors. In contrast, calibration curves collected at inappropriate temperatures or in aged blood samples deviated more significantly from those seen in fresh, body temperature blood, producing substantial over- or under-estimates of target concentration. Finally, in some cases, it is possible to use simpler media, such as phosphate buffered saline with bovine serum albumin, as a convenient and proxy for freshly collected blood for applications in which reduced accuracy is an acceptable trade-off relative to improved ease of calibration.

4.5 MATERIALS & METHODS

Electrode Fabrication

We fabricated sensors by soldering a 5 cm long, 75 µm diameter, PFA-coated gold wire (A-M Systems, Sequim, WA) to a gold-plated pin connector (CH Instruments, Inc., Austin, TX) with 60/40 lead-selenium solder (Digikey, Thief River Falls, MN). Before soldering, we used a digital caliper and razor blade to isolate 3 mm of gold on both ends of the gold wire. One end forms the working electrode, and the other end must be exposed for successful soldering. To prevent breakage of the delicate wires, we coated the wire-solder interface with a coat of urethane conformal coating (MG Chemicals, Surrey CA).

Aptamer Preparation

We first thawed a 2 μL, aliquot of 100 μM aptamer (sequence below) modified with a 6-carbon thiol linker on the 5’ end and methylene blue on the 3’ end (Biosearch Technologies, Novato, CA, dual HPLC purification, stored at -20°C).

5’-SH-$(CH_2)_6$- CGAGG GTACC GCAAT AGTAC TTATT GTTCG CCTAT TGTGG GTCGG-O-CH_2-$CHCH_2OH$-$(CH_2)_4$-NH-CO-$(CH_2)_2$-methylene blue-3’

Because the manufacturer provides the DNA constructs in oxidized form, which does not effectively immobilize onto the gold surface, we must reduce the disulfide bond before deposition. To do so, we combined 2 μL of 10 mM Tris (2-carboxyethyl) phosphine (TCEP, Sigma-Aldrich, St. Louis, MO) with the aptamer sample for a 1 h thiol reduction in the dark at room temperature. We then diluted the sample with 96 μL 1X phosphate buffered saline (PBS, ChemCruz 20X phosphate buffered saline, Santa Cruz Biotechnology, Dallas, TX) and quantified the concentration of the aptamer using the molar absorption coefficient at 260 nm provided by the supplier with UV-VIS spectroscopy (DU800, Beckman Coulter, Brea, CA). Using PBS, we then diluted the aptamer to 500 nM.

Electrode Preparation

For electrode cleaning and in-vitro characterization, our electrochemical cell contained a PFA-wrapped gold sensor working electrode, a platinum counter electrode (CH Instruments, Inc, Austin, TX), and an Ag|AgCl reference electrode (CH

Instruments, Inc., Austin TX). We secured our working, counter, and reference electrodes in a cell vessel “shot glass” with a custom-fabricated Teflon lid fixture (See **Figure 1C**). First, we electrochemically cleaned the electrodes in 0.5 M NaOH (Sigma-Aldrich, St. Louis, MO) by performing repeated cyclic voltammetry scans between -1 and -1.6 V (all potentials versus Ag|AgCl) at 1 V s^{-1} scan rate for 300 cycles using a CH Multipotentiostat (CHI1040C, CH Instruments, Inc.). We rinsed the electrodes in deionized water, then increased the surface area of the gold wire electrode by electrochemically roughening in 0.5 M H_2SO_4 (Sigma-Aldrich, St. Louis, MO) using a previously-described procedure that involves repeatedly stepping the potential between 0 and 2.2 V[30]. This results in a 2 to 5-fold increase in microscopic surface area, attributed to islands of nano-scale dendrites forming on the planar gold surface[30].

Sensor Fabrication

Immediately after roughening, we rinse the electrodes thoroughly in deionized water and place them in the prepared aptamer solution for 1 h at room temperature in dark conditions. We then rinsed the electrodes with deionized water and immersed them for 12 to 18 h at room temperature in a 10 mM 6-mercapto-1-hexanol (Sigma-Aldrich, St. Louis, MO) in 1X PBS to passivate the surface. Following a final rinse with deionized water, the sensor was ready for use.

Measurements

We filled the electrochemical cell with PBS, rinsed the electrodes in deionized water, and secured them in the electrochemical cell's Teflon cap. Before each experiment, we collected a baseline cyclic voltammogram in PBS (-0.1 to -0.5 V, 0.1 V/s).

To perform a titration, we moved the electrode cap to the selected media. We collected square wave voltammetry scans (-0.2 to -0.4 V, 25 mV amplitude) at 10, 25, and 300 Hz. Upon addition of a given target concentration, we back pipetted 15 times, allowed the solution to rest for two minutes, then proceeded with the measurement. To perform a spiking experiment, we used a CH software macro to repeatedly collect and store square wave voltammograms. We collected a 10 min baseline with no target, then sequentially added 10, 20, 50, 100, 300 µM vancomycin. For each addition, we pipetted rapidly, while taking care not to create bubbles in the blood, then measured the resulting signal for 5 to 10 min.

It is common to observe a downward drift in square wave voltammogram peak current, especially in complex media, such as whole blood. To correct for any peak signal loss, we applied a previously-described drift correction technique termed "Kinetic Differential Measurements" (KDM)[12,14,15]. Here, KDM denotes when normalized signal off-peak currents are subtracted from the normalized signal-on peak currents.

Data Analysis

To analyze square wave voltammetry peak currents in real time, we used a previously-reported, open source python script[4]. When provided with voltammogram bounds (typically, -0.2 to -0.4 V) and desired Savitzky–Golay filtering (5 mV), this script calculates peak height and KDM values. Raw data from this program was exported to Matlab for data analysis and presentation.

4.6 ACKNOWLEDGEMENTS

This work was funded by NIH grant R01AI145206. This material is based upon work supported by the National Science Foundation Graduate Research Fellowship under Grant No. 1650114. The content of the information does not necessarily reflect the position or the policy of the Government, and no official endorsement should be inferred.

4.7 SUPPLEMENTAL INFORMATION

Table S1: Employing “out of dataset” calibration curves does not significantly reduce accuracy over the clinically relevant target concentration range. Here, we challenged four sensors, in each case using the average calibration curve of the other three sensors.

Actual concentration (µM)	10	20	50	100	300
Mean estimated concentration (µM)	9.2	18.7	44.7	95.7	304.0
Mean accuracy (µM)	0.8	1.3	5.3	4.3	4.0
Mean relative accuracy	- 8.2%	- 6.6%	- 10.6%	- 4.3%	1.3%
Standard deviation (µM)	1.4	1.9	4.0	13.1	111.4
Relative precision	± 30%	± 20%	± 18%	± 27%	± 73%

Table S2: Calibrating each individual sensor does not significantly improve accuracy over the clinically relevant target concentration range. To show this, we used the Hill-Langmuir isotherm calibration curve of each individual electrode to produce concentration estimates using that same electrode when challenged with a series of vancomycin additions in 37°C fresh rat blood.

Actual concentration (µM)	10	20	50	100	300
Mean estimated concentration (µM)	9.2	18.7	44.7	94.9	278.3
Mean accuracy (µM)	0.8	1.3	5.3	5.1	21.7
Mean relative accuracy	- 7.9%	- 6.4%	- 10.6%	- 5.2%	- 7.2%
Standard deviation (µM)	1.2	1.7	2.7	5.2	24.3
Relative precision	± 25%	± 18%	± 11%	± 11%	± 18%

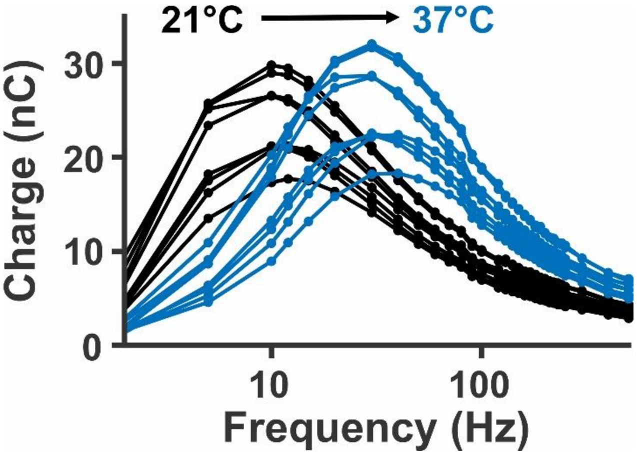

Figure S1: Between room temperature (black) and body temperature (blue), peak charge transfer shifts toward higher frequencies, indicating an increase in electron transfer rate. Shown are plots of charge transfer versus square-wave frequency for eight sensors. Note that variation in ethe total charge transferred occurs due to differences in electrode gold surface area, which changes the number of methylene blue redox reporters for a given sensor.

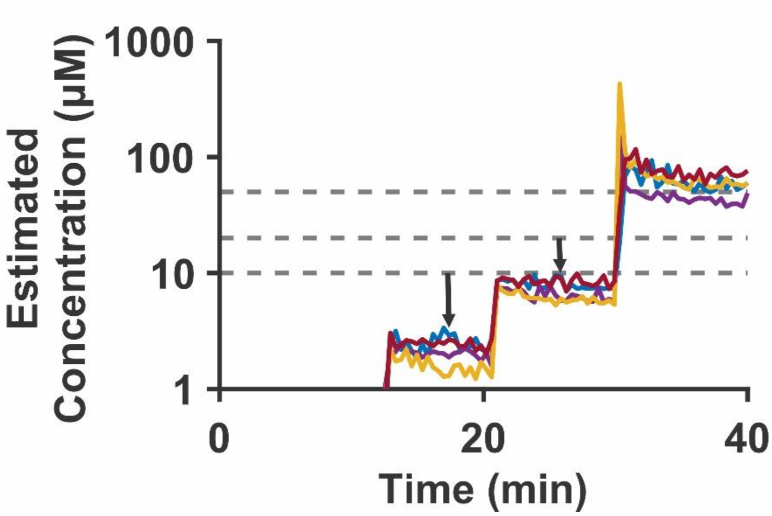

Figure S2: Calibrating EAB sensor data collected at body temperature with a calibration curve collected at room temperature fails to quantify additions of 100 and 300 µM, and produces substantial under-estimates of vancomycin concentration at 10 and 20 µM doses.

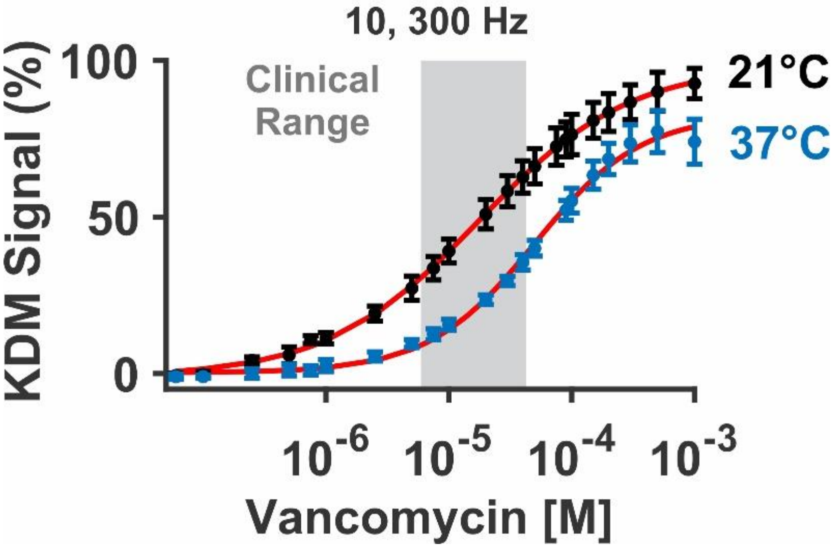

Figure S3: EAB sensor response is sufficiently temperature dependent that the change in signaling between room and body temperature is substantial. Here, we compare titrations in freshly collected rat blood at 21°C and 37°C. Calibration curves collected at 10 and 300 Hz at 21°C (black, n = 4 sensors, K_D = 175 ± 1 µM) and 37°C (blue, n = 4 sensors, K_D = 499 ± 8 µM) yield a 20 - 25 % difference in clinical range response magnitudes.

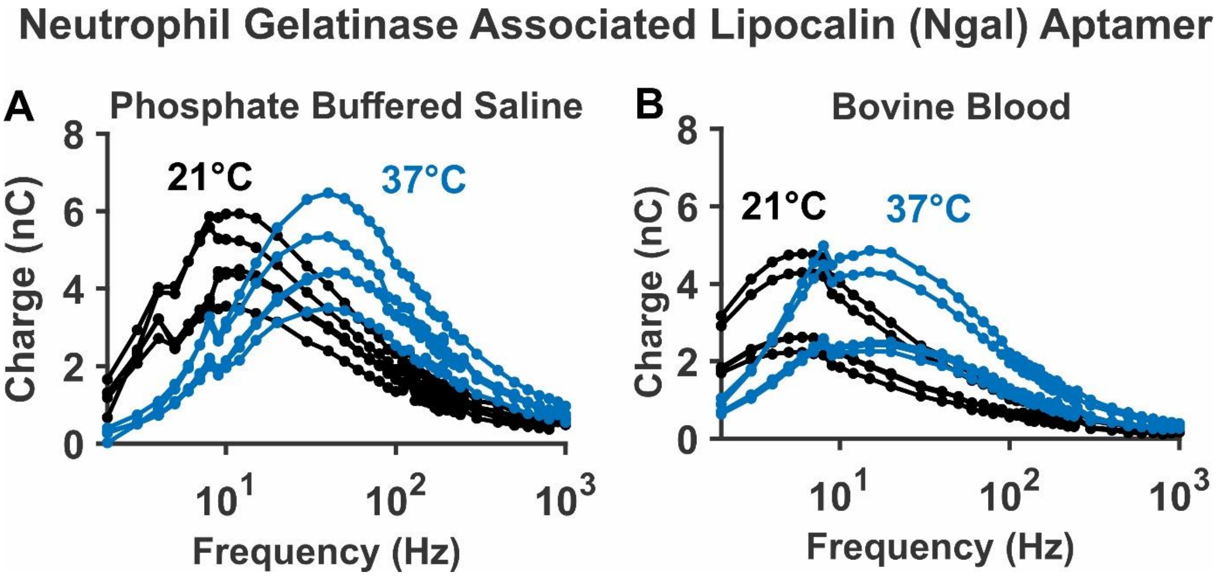

Figure S4: For an aptamer responding to the protein target, Ngal, electron transfer changes substantially between room (20˚C) and body (37˚C) temperature. **(A)** In phosphate buffered saline, the peak charge transfer shifts by 30 Hz (from a frequency of approximately 10 Hz to 40 Hz). **(B)** In whole bovine blood, the peak location shifts by 10 Hz (from approximately 5 Hz to 15 Hz).

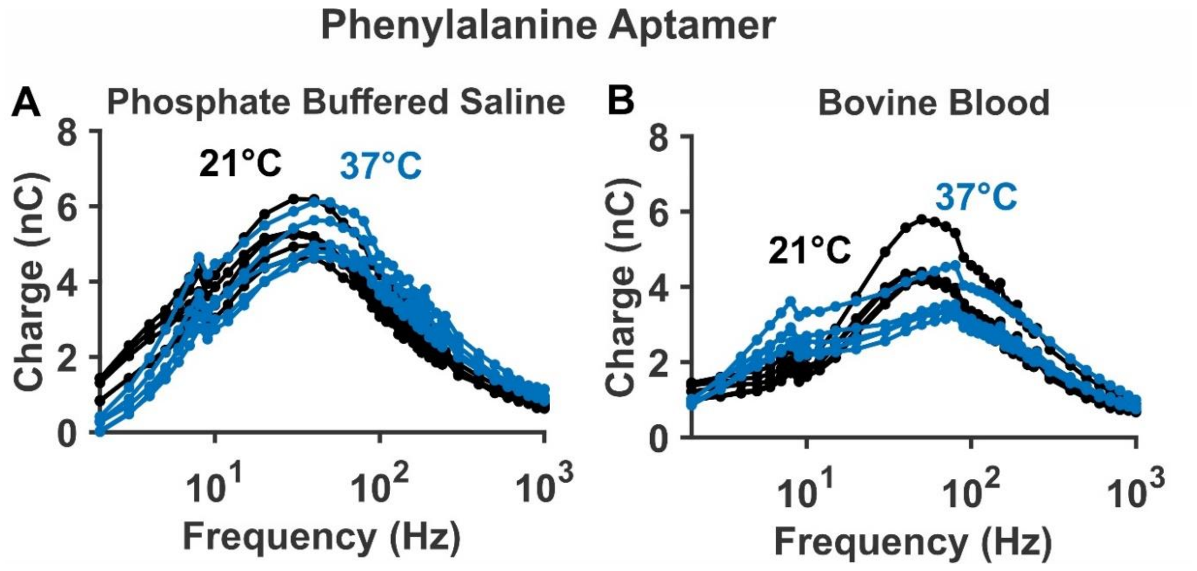

Figure S5: For an aptamer responding to the amino acid target, phenylalanine, electron transfer changes slightly between room (20˚C) and body (37˚C) temperature. **(A)** In phosphate buffered saline, the peak charge transfer shifts by approximately 10 Hz (from 30-40 Hz to 40-50 Hz). **(B)** In whole bovine blood, the peak broadens, and a slight secondary peak appears at frequencies near 10 Hz.

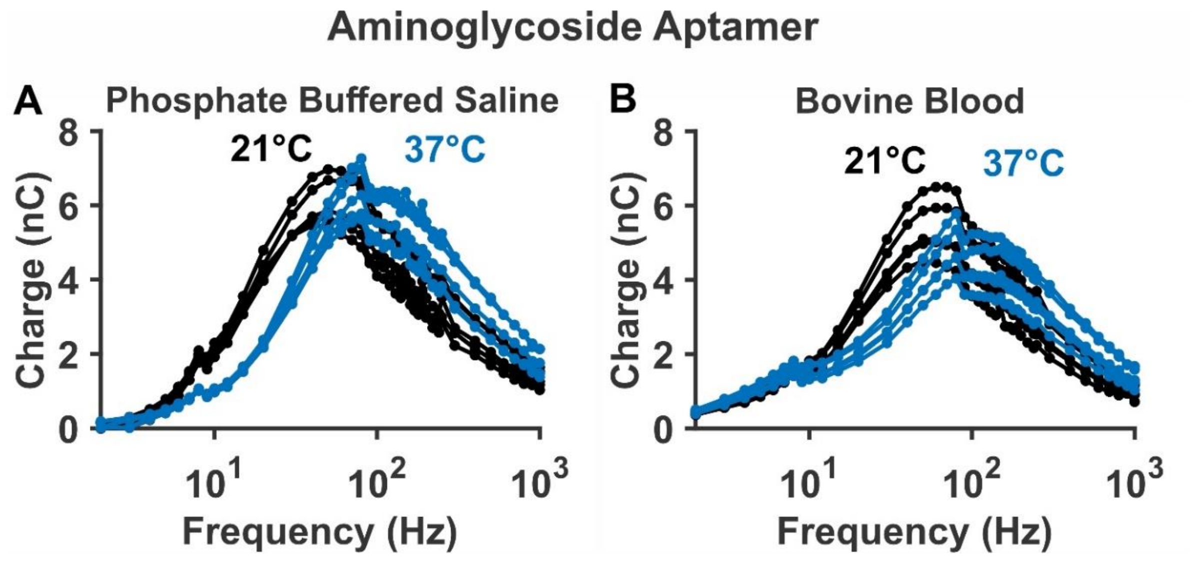

Figure S6: For an aptamer responding to aminoglycoside antibiotics, electron transfer changes substantially between room (20˚C) and body (37˚C) temperature. This occurs in both **(A)** phosphate buffered saline and **(B)** undiluted bovine blood.

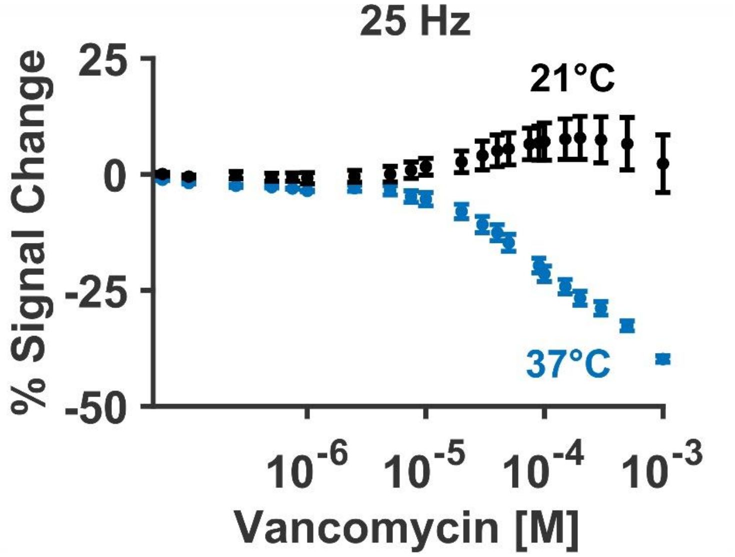

Figure S7: Between room temperature (black) and body temperature (blue) the normalized peak signal observed at 25 Hz changes from a weak signal-on response to a clear signal-off response.

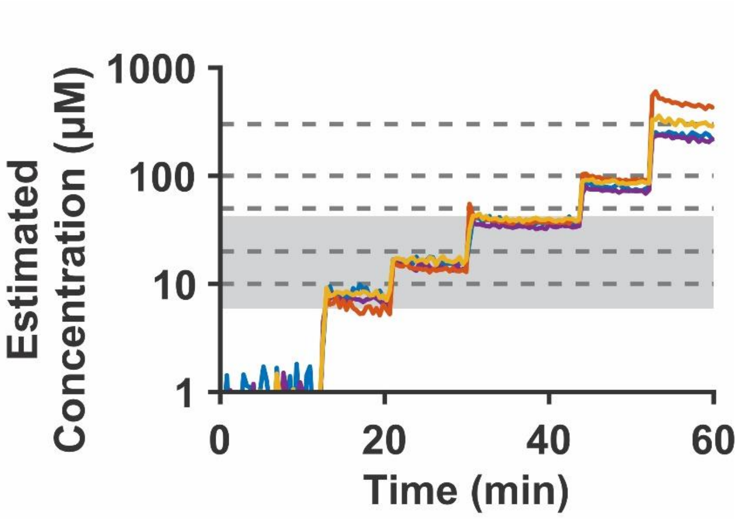

Figure S8: We calibrate the response of our sensors in body temperature rat blood using a titration curve collected in body temperature PBS with 2 mM $MgCl_2$ and 30 mg/mL BSA (dotted lines indicating 10, 20, 50, 100, and 300 µM vancomycin, grey area indicated clinical range).

Table S3: Calibrating each data collected in body temperature rat blood with a calibration curve collected in body temperature PBS with 2 mM $MgCl_2$ and 30 mg/mL BSA produces measurement accuracy of greater than 25%.

Actual concentration (μM)	10	20	50	100	300
Mean estimated concentration (μM)	9.2	18.7	44.7	94.9	278.3
Mean accuracy (μM)	0.8	1.3	5.3	5.1	21.7
Mean relative accuracy	- 7.9%	- 6.4%	- 10.6%	- 5.2%	- 7.2%
Standard deviation (μM)	1.2	1.7	2.7	5.2	24.3
Relative precision	± 25%	± 18%	± 11%	± 11%	± 18%

4.8 REFERENCES

(1) Arroyo-Currás, N.; Dauphin-Ducharme, P.; Ortega, G.; Ploense, K. L.; Kippin, T. E.; Plaxco, K. W. Subsecond-Resolved Molecular Measurements in the Living Body Using Chronoamperometrically Interrogated Aptamer-Based Sensors. *ACS Sensors* **2018**, *3*, 360-366, 10.1021/acssensors.7b00787.

(2) Downs, A. M.; Gerson, J.; Ploense, K. L.; Plaxco, K. W.; Dauphin-Ducharme, P. Subsecond-Resolved Molecular Measurements Using Electrochemical Phase Interrogation of Aptamer-Based Sensors. *Analytical Chemistry* **2020**, *92*, 14063-14068, 10.1021/acs.analchem.0c03109.

(3) Ferguson, B. S.; Hoggarth, D. A.; Maliniak, D.; Ploense, K.; White, R. J.; Woodward, N.; Hsieh, K.; Bonham, A. J.; Eisenstein, M.; Kippin, T. E.; Plaxco, K. W.; Soh, H. T. Real-Time, Aptamer-Based Tracking of Circulating Therapeutic Agents in Living Animals. *Science translational medicine* **2013**, *5*, 213ra165, 10.1126/scitranslmed.3007095.

(4) Curtis, S. D.; Ploense, K. L.; Kurnik, M.; Ortega, G.; Parolo, C.; Kippin, T. E.; Plaxco, K. W.; Arroyo-Currás, N. Open Source Software for the Real-Time Control, Processing, and Visualization of High-Volume Electrochemical Data. *Analytical Chemistry* **2019**, *91*, 12321-12328, 10.1021/acs.analchem.9b02553.

(5) Baker, B. R.; Lai, R. Y.; Wood, M. S.; Doctor, E. H.; Heeger, A. J.; Plaxco, K. W. An Electronic, Aptamer-Based Small-Molecule Sensor for the Rapid, Label-Free Detection of Cocaine in Adulterated Samples and Biological Fluids. *Journal of the American Chemical Society* **2006**, *128*, 3138-3139, 10.1021/ja056957p.
(6) Xiao, Y.; Lubin, A. A.; Heeger, A. J.; Plaxco, K. W. Label-Free Electronic Detection of Thrombin in Blood Serum by Using an Aptamer-Based Sensor. *Angewandte Chemie International Edition* **2005**, *44*, 5456-5459, 10.1002/anie.200500989.
(7) White, R. J.; Plaxco, K. W. Exploiting Binding-Induced Changes in Probe Flexibility for the Optimization of Electrochemical Biosensors. *Analytical Chemistry* **2010**, *82*, 73-76, 10.1021/ac902595f.
(8) White, R. J.; Phares, N.; Lubin, A. A.; Xiao, Y.; Plaxco, K. W. Optimization of Electrochemical Aptamer-Based Sensors via Optimization of Probe Packing Density and Surface Chemistry. *Langmuir* **2008**, *24*, 10513-10518, 10.1021/la800801v.
(9) Idili, A.; Arroyo-Currás, N.; Ploense, K. L.; Csordas, A. T.; Kuwahara, M.; Kippin, T. E.; Plaxco, K. W. Seconds-resolved pharmacokinetic measurements of the chemotherapeutic irinotecan in situ in the living body. *Chemical Science* **2019**, *10*, 8164-8170, 10.1039/C9SC01495K.
(10) Idili, A.; Gerson, J.; Kippin, T.; Plaxco, K. W. Seconds-Resolved, In Situ Measurements of Plasma Phenylalanine Disposition Kinetics in Living Rats. *Analytical Chemistry* **2021**, *93*, 4023-4032, 10.1021/acs.analchem.0c05024.
(11) Li, H.; Dauphin-Ducharme, P.; Arroyo-Currás, N.; Tran, C. H.; Vieira, P. A.; Li, S.; Shin, C.; Somerson, J.; Kippin, T. E.; Plaxco, K. W. A Biomimetic Phosphatidylcholine-Terminated Monolayer Greatly Improves the In Vivo Performance of Electrochemical Aptamer-Based Sensors. **2017**, *56*, 7492-7495, 10.1002/anie.201700748.
(12) Arroyo-Currás, N.; Somerson, J.; Vieira, P. A.; Ploense, K. L.; Kippin, T. E.; Plaxco, K. W. Real-time measurement of small molecules directly in awake, ambulatory animals. **2017**, *114*, 645-650, 10.1073/pnas.1613458114 %J Proceedings of the National Academy of Sciences.
(13) Parolo, C.; Idili, A.; Ortega, G.; Csordas, A.; Hsu, A.; Arroyo-Currás, N.; Yang, Q.; Ferguson, B. S.; Wang, J.; Plaxco, K. W. Real-Time Monitoring of a Protein Biomarker. *ACS sensors* **2020**, *5*, 1877-1881, 10.1021/acssensors.0c01085.
(14) Dauphin-Ducharme, P.; Yang, K.; Arroyo-Currás, N.; Ploense, K. L.; Zhang, Y.; Gerson, J.; Kurnik, M.; Kippin, T. E.; Stojanovic, M. N.; Plaxco, K. W. Electrochemical Aptamer-Based Sensors for Improved Therapeutic Drug Monitoring and High-Precision, Feedback-Controlled Drug Delivery. *ACS sensors* **2019**, *4*, 2832-2837, 10.1021/acssensors.9b01616.
(15) Arroyo-Currás, N.; Ortega, G.; Copp, D. A.; Ploense, K. L.; Plaxco, Z. A.; Kippin, T. E.; Hespanha, J. P.; Plaxco, K. W. High-Precision Control of Plasma Drug Levels Using Feedback-Controlled Dosing. *ACS Pharmacology & Translational Science* **2018**, *1*, 110-118, 10.1021/acsptsci.8b00033.
(16) Pellitero, M. A.; Curtis, S. D.; Arroyo-Currás, N. Interrogation of Electrochemical Aptamer-Based Sensors via Peak-to-Peak Separation in Cyclic Voltammetry Improves the Temporal Stability and Batch-to-Batch Variability in Biological Fluids. *ACS Sensors* **2021**, *6*, 1199-1207, 10.1021/acssensors.0c02455.

(17) Santos-Cancel, M.; Lazenby, R. A.; White, R. J. Rapid Two-Millisecond Interrogation of Electrochemical, Aptamer-Based Sensor Response Using Intermittent Pulse Amperometry. *ACS Sensors* **2018**, *3*, 1203-1209, 10.1021/acssensors.8b00278.
(18) Li, H.; Dauphin-Ducharme, P.; Ortega, G.; Plaxco, K. W. Calibration-Free Electrochemical Biosensors Supporting Accurate Molecular Measurements Directly in Undiluted Whole Blood. *Journal of the American Chemical Society* **2017**, *139*, 11207-11213, 10.1021/jacs.7b05412.
(19) Dauphin-Ducharme, P.; Plaxco, K. W. Maximizing the Signal Gain of Electrochemical-DNA Sensors. *Analytical Chemistry* **2016**, *88*, 11654-11662, 10.1021/acs.analchem.6b03227.
(20) Ferguson, B. S.; Hoggarth, D. A.; Maliniak, D.; Ploense, K.; White, R. J.; Woodward, N.; Hsieh, K.; Bonham, A. J.; Eisenstein, M.; Kippin, T. E.; Plaxco, K. W.; Soh, H. T. Real-time, aptamer-based tracking of circulating therapeutic agents in living animals. *Science translational medicine* **2013**, *5*, 213ra165, 10.1126/scitranslmed.3007095.
(21) Gesztelyi, R.; Zsuga, J.; Kemeny-Beke, A.; Varga, B.; Juhasz, B.; Tosaki, A. The Hill equation and the origin of quantitative pharmacology. *Archive for History of Exact Sciences* **2012**, *66*, 427-438, 10.1007/s00407-012-0098-5.
(22) Chen, Z.-m.; Wang, Y.; Du, X.-y.; Sun, J.-J.; Yang, S. Temperature-Alternated Electrochemical Aptamer-Based Biosensor for Calibration-Free and Sensitive Molecular Measurements in an Unprocessed Actual Sample. *Analytical Chemistry* **2021**, *93*, 7843-7850, 10.1021/acs.analchem.1c00289.
(23) Wang, C.; Liu, L.; Zhao, Q. Low Temperature Greatly Enhancing Responses of Aptamer Electrochemical Sensor for Aflatoxin B1 Using Aptamer with Short Stem. *ACS Sensors* **2020**, *5*, 3246-3253, 10.1021/acssensors.0c01572.
(24) Hianik, T.; Ostatná, V.; Sonlajtnerova, M.; Grman, I. Influence of ionic strength, pH and aptamer configuration for binding affinity to thrombin. *Bioelectrochemistry* **2007**, *70*, 127-133, 10.1016/j.bioelechem.2006.03.012.
(25) Xiao, Y.; Uzawa, T.; White, R. J.; DeMartini, D.; Plaxco, K. W. On the Signaling of Electrochemical Aptamer-Based Sensors: Collision- and Folding-Based Mechanisms. **2009**, *21*, 1267-1271, 10.1002/elan.200804564.
(26) Martin, J. H.; Norris, R.; Barras, M.; Roberts, J.; Morris, R.; Doogue, M.; Jones, G. R. Therapeutic monitoring of vancomycin in adult patients: a consensus review of the American Society of Health-System Pharmacists, the Infectious Diseases Society of America, and the Society Of Infectious Diseases Pharmacists. *The Clinical biochemist. Reviews* **2010**, *31*, 21-24,
(27) Suzuki, Y.; Kawasaki, K.; Sato, Y.; Tokimatsu, I.; Itoh, H.; Hiramatsu, K.; Takeyama, M.; Kadota, J. Is peak concentration needed in therapeutic drug monitoring of vancomycin? A pharmacokinetic-pharmacodynamic analysis in patients with methicillin-resistant staphylococcus aureus pneumonia. *Chemotherapy* **2012**, *58*, 308-312, 10.1159/000343162.
(28) Chavada, R.; Ghosh, N.; Sandaradura, I.; Maley, M.; Van Hal, S. J. Establishment of an AUC(0-24) Threshold for Nephrotoxicity Is a Step towards Individualized Vancomycin Dosing for Methicillin-Resistant Staphylococcus aureus

Bacteremia. *Antimicrobial agents and chemotherapy* **2017**, *61*, 10.1128/aac.02535-16.
(29) Lovrić, M.; Komorsky-Lovric, Š. Square-wave voltammetry of an adsorbed reactant. *Journal of Electroanalytical Chemistry and Interfacial Electrochemistry* **1988**, *248*, 239-253, 10.1016/0022-0728(88)85089-7.
(30) Arroyo-Currás, N.; Scida, K.; Ploense, K. L.; Kippin, T. E.; Plaxco, K. W. High Surface Area Electrodes Generated via Electrochemical Roughening Improve the Signaling of Electrochemical Aptamer-Based Biosensors. *Analytical Chemistry* **2017**, *89*, 12185-12191, 10.1021/acs.analchem.7b02830.